

REPORT DOCUMENTATION PAGE			Form Approved OMB NO. 0704-0188		
<p>The public reporting burden for this collection of information is estimated to average 1 hour per response, including the time for reviewing instructions, searching existing data sources, gathering and maintaining the data needed, and completing and reviewing the collection of information. Send comments regarding this burden estimate or any other aspect of this collection of information, including suggestions for reducing this burden, to Washington Headquarters Services, Directorate for Information Operations and Reports, 1215 Jefferson Davis Highway, Suite 1204, Arlington VA, 22202-4302. Respondents should be aware that notwithstanding any other provision of law, no person shall be subject to any penalty for failing to comply with a collection of information if it does not display a currently valid OMB control number.</p> <p>PLEASE DO NOT RETURN YOUR FORM TO THE ABOVE ADDRESS.</p>					
1. REPORT DATE (DD-MM-YYYY) 20-01-2011		2. REPORT TYPE Final Report		3. DATES COVERED (From - To) 1-Aug-2005 - 27-Jul-2008	
4. TITLE AND SUBTITLE Femtosecond-laser patterning of polymers: nonlinear and negative index devices			5a. CONTRACT NUMBER W911NF-05-1-0471		
			5b. GRANT NUMBER		
			5c. PROGRAM ELEMENT NUMBER 611102		
6. AUTHORS Eric Mazur, Kevin Vora, Michael Moebius			5d. PROJECT NUMBER		
			5e. TASK NUMBER		
			5f. WORK UNIT NUMBER		
7. PERFORMING ORGANIZATION NAMES AND ADDRESSES Harvard University Office of Sponsored Research 1350 Massachusetts Ave. Holyoke 727 Cambridge, MA 02138 -			8. PERFORMING ORGANIZATION REPORT NUMBER		
9. SPONSORING/MONITORING AGENCY NAME(S) AND ADDRESS(ES) U.S. Army Research Office P.O. Box 12211 Research Triangle Park, NC 27709-2211			10. SPONSOR/MONITOR'S ACRONYM(S) ARO		
			11. SPONSOR/MONITOR'S REPORT NUMBER(S) 49014-PH.1		
12. DISTRIBUTION AVAILABILITY STATEMENT Approved for Public Release; Distribution Unlimited					
13. SUPPLEMENTARY NOTES The views, opinions and/or findings contained in this report are those of the author(s) and should not be construed as an official Department of the Army position, policy or decision, unless so designated by other documentation.					
14. ABSTRACT The research described in this report focused on expanding our knowledge of laser micromachining and the scope of femtosecond laser fabrication. The research addressed Army Research Office initiatives for the development of novel photonics devices and techniques that utilize nonlinear optical phenomena. The interaction of femtosecond laser pulses with polymers were studied and the conditions for device fabrication					
15. SUBJECT TERMS MICROFABRICATION; LITHOGRAPHY; PHOTOPOLYMERIZATION; MICROSTRUCTURES; NANOPARTICLES; CHITIN; POLYMERS; BIOMATERIALS; RAMAN SPECTROSCOPY AND SCATTERING; ENHANCED					
16. SECURITY CLASSIFICATION OF:			17. LIMITATION OF ABSTRACT UU	15. NUMBER OF PAGES	19a. NAME OF RESPONSIBLE PERSON Eric Mazur
a. REPORT UU	b. ABSTRACT UU	c. THIS PAGE UU			19b. TELEPHONE NUMBER 617-495-8729

Report Title

Femtosecond-laser patterning of polymers: nonlinear and negative index devices

ABSTRACT

The research described in this report focused on expanding our knowledge of laser micromachining and the scope of femtosecond laser fabrication. The research addressed Army Research Office initiatives for the development of novel photonics devices and techniques that utilize nonlinear optical phenomena.

The interaction of femtosecond laser pulses with polymers were studied and the conditions for device fabrication were optimized. Various ways for inducing nonlinear response in polymers devices were investigated. The work allowed the group to expand its investigation of femtosecond laser interactions with materials to polymers and create polymer-based photonic devices. The applications of research may extend into other fields, including medicine and engineering.

Femtosecond laser pulses were also used to study ultrafast dynamics in solids, such as zinc oxide, through pump probe experiments. The transient material properties obtained through such experiments can be used to optimize ZnO-based devices. Other dielectric materials, including fused silica and diamond were micromachined and studied under irradiation from femtosecond laser pulses.

List of papers submitted or published that acknowledge ARO support during this reporting period. List the papers, including journal references, in the following categories:

(a) Papers published in peer-reviewed journals (N/A for none)

Three-dimensional fabrication of optically active microstructures containing an electroluminescent polymer
Mendonca CR, Correa DS, Marlow F, Voss T, Tayalia P, Mazur E
Applied Physics Letters, 95, 11 (2009).

Two-Photon Polymerization for Fabricating Structures Containing the Biopolymer Chitosan
Correa DS, Tayalia P, Cosendey G, dos Santos DS, Aroca RF, Mazur E, Mendonca CR
Journal of Nanoscience and Nanotechnology, 9, 10, 5845-5849 (2009).

Dielectric function dynamics during femtosecond laser excitation of bulk ZnO
Shih T, Winkler MT, Voss T, et al.
Applied Physics A, 96, 2, 363-367 (2009).

Ultrafast dynamics of bis (n-butylimido) perylene thin films excited by two-photon absorption
Mendonca CR, Kandyla M, Shih T, Aroca RF, Constantino CJL, Mazur E
Applied PHysics A, 96, 2, 369-372 (2009).

Femtosecond laser-induced formation of nanometer-width grooves on synthetic single-crystal diamond surfaces
Shinoda M, Gattass RR, Mazur E
Journal of Applied Physics, 105, 5 (2009).

Femtosecond laser waveguide micromachining of PMMA films with azoaromatic chromophores
Cleber R. Mendonca, Tina Shih and Eric Mazur
Opt. Express, 16, 200-206 (2008).

3D cell migration studies using two-photon engineered polymer scaffolds
Prakriti Tayalia, Cleber Mendonca and Eric Mazur
Advanced Materials, 20, 4494-4498 (2008).

Femtosecond laser micromachining in transparent materials
Rafael Gattass and Eric Mazur
Nat. Phot., 2, 219-225 (2008).

Two-photon absorption spectrum of the photoinitiator Lucirin TPO-L
C. R. Mendonca, D. S. Correa, T. Baldacchini, P. Tayalia and E. Mazur
Appl. Phys. A, 90, 633-636 (2008).

Femtosecond laser micromaching in the conjugated polymer MEH- PPV
C. R. Mendonca, S. Orlando, G. Cosendey, M. T. Winkler and E. Mazur
Applied Surface Science, 254, 1135-1139 (2007).

Faraday rotation in femtosecond laser micromachined waveguides
Tina Shih, Rafael R. Gattass, Cleber R. Mendonca and Eric Mazur
Opt Express, 15, 5809-5814 (2007).

Reversible birefringence in microstructures fabricated by two-photon absorption polymerization
Cleber Mendonca, Tommaso Baldacchini, Prakriti Tayalia andEric Mazur
J. Appl. Phys., 103, 013109-1-013109-4 (2007).

Optical loss measurements in femtosecond laser written waveguides in glass
Limin Tong, Rafael R. Gattass, Iva Zaharieva Maxwell,Jonathan B. Ashcom and Eric Mazur
Opt. Commun., 259, 626-630 (2006).

Numerical aperture dependence of damage and supercontinuum generation from femtosecond laser pulses in bulk fused silica
Jonathan B. Ashcom, Rafael R. Gattass, Chris B. Schaffer and Eric Mazur
J. Opt. Soc. Am. B, 23, 2317-2322 (2006).

Number of Papers published in peer-reviewed journals:
14.00

(b) Papers published in non-peer-reviewed journals or in conference proceedings (N/A for none)

Number of Papers published in non peer-reviewed journals: 0.00

(c) Presentations

Two-photon microfabrication of structures containing, presented by at the 2007 MRS Fall Meeting in Boston, MA, USA on 29 November 2007

Femtosecond laser micromaching in the conjugated polymer MEH-PPV, poster presented by at the E-MRS Spring Meeting in Strasbourg, France on 31 May 2007

Two-photon engineered polymer scaffolds for 3D migration studies, presented by at the MRS Fall Conference 2006 in Cambridge, MA on 29 November 2006

Three-dimensional microfabrication with conjugated polymers, poster presented by at 2006 MRS Fall Meetng in Boston, MA, USA on 30 November 2006

Femtosecond laser micromachining in azopolymer films, poster presented by at the 2006 MRS Fall Meeting in Boston, MA, USA on 27 November 2006

Femtosecond micromachining of waveguides in a Faraday material, presented by at Photonics West 2006 in San Jose, CA on 24 January 2006

Femtosecond laser micromachining, Invited paper presented by at Photonics West 2006 in San Jose, CA on 24 January 2006

Number of Presentations: 7.00

Non Peer-Reviewed Conference Proceeding publications (other than abstracts):

Complex microstructures fabricated via two-photon absorption polymerization
Daniel Souza Correa, Prakriti Tayalia, Eric Mazur and Cleber R. Mendonca
Macro 2006 - 41st Symposium on Macromolecules Proceedings (Rio de Janeiro, 2006) 1-2.

Three-dimensional microfabrication for photonics and biomedical applications
C. R. Mendonca, P. Tayalia, T. Baldacchini and E. Mazur
Macro 2006 - 41st International Symposium on Macromolecules Proceedings (Rio de Janeiro, 2006) 1-2.

A novel photoinitiator for microfabrication via two-photon polymerization
Cleber R. Mendonca, Daniel S. Correa, Tommaso Baldacchini,Prakriti Tayalia and Eric Mazur
Technical Digest CLEO 2006 (Long Beach, CA, 2006) CThQ5 1-2.

Reversible birefringence in microstructures fabricated by two-photon polymerization
C. R. Mendonca, T. Baldacchini, P. Tayalia and E. Mazur
Technical Digest CLEO 2006 (Long Beach, CA, 2006) CMX2 1-2.

Number of Non Peer-Reviewed Conference Proceeding publications (other than abstracts): 4

Peer-Reviewed Conference Proceeding publications (other than abstracts):

Number of Peer-Reviewed Conference Proceeding publications (other than abstracts): 0

(d) Manuscripts

Number of Manuscripts: 0.00

Patents Submitted

Patents Awarded

Awards

Eric Mazur, PI:

Millikan Medal, AAPT, 2008
Corresponding Member, Royal Academy of Arts and Sciences of the Netherlands, 2008
Esther Hoffman Beller Medal, Optical Society of America, 2008
Fellow, Optical Society of America, 2008
Phi Beta Kappa Visiting Scholar, 2007
Baetjer Lectureship, Princeton University, 2007
Award of Distinction (Communicator Award) for Interactive Teaching DVD, 2006
Selected as one of 75 Outstanding Physicist, AAPT, 2006
Silver Remi Award, Houston International Film Festival, 2006

Graduate Students

<u>NAME</u>	<u>PERCENT SUPPORTED</u>
Prakriti Tayalia	0.50
Tina Shih	0.20
Rafael Gattass	0.50
FTE Equivalent:	1.20
Total Number:	3

Names of Post Doctorates

<u>NAME</u>	<u>PERCENT SUPPORTED</u>
Cleber Mendonca	0.10
Tomaso Baldacchini	0.50
Tobias Voss	0.50
FTE Equivalent:	1.10
Total Number:	3

Names of Faculty Supported

<u>NAME</u>	<u>PERCENT SUPPORTED</u>	National Academy Member
Eric Mazur	0.10	No
FTE Equivalent:	0.10	
Total Number:	1	

Names of Under Graduate students supported

<u>NAME</u>	<u>PERCENT SUPPORTED</u>
Gatien Cosendey	0.00
Rafael Tilghman	0.10
FTE Equivalent:	0.10
Total Number:	2

Student Metrics

This section only applies to graduating undergraduates supported by this agreement in this reporting period

The number of undergraduates funded by this agreement who graduated during this period:	1.00
The number of undergraduates funded by this agreement who graduated during this period with a degree in science, mathematics, engineering, or technology fields:.....	1.00
The number of undergraduates funded by your agreement who graduated during this period and will continue to pursue a graduate or Ph.D. degree in science, mathematics, engineering, or technology fields:.....	1.00
Number of graduating undergraduates who achieved a 3.5 GPA to 4.0 (4.0 max scale):.....	1.00
Number of graduating undergraduates funded by a DoD funded Center of Excellence grant for Education, Research and Engineering:.....	0.00
The number of undergraduates funded by your agreement who graduated during this period and intend to work for the Department of Defense	0.00
The number of undergraduates funded by your agreement who graduated during this period and will receive scholarships or fellowships for further studies in science, mathematics, engineering or technology fields:	0.00

Names of Personnel receiving masters degrees

NAME

MASTERS?

Total Number:

1

Names of personnel receiving PhDs

NAME

Rafael Gattass

Tina Shih

Total Number:

2

Names of other research staff

NAME

PERCENT SUPPORTED

FTE Equivalent:

Total Number:

Sub Contractors (DD882)

Inventions (DD882)

Table of contents

Statement of the problem studied	2
Summary of most important results	3
Bibliography	8
Appendix A: Peer-reviewed publications	10

Statement of the problem studied

The research described in this report focused on expanding our knowledge of laser micromachining and the scope of femtosecond laser fabrication. The research addressed Army Research Office initiatives for the development of novel photonics devices and techniques that utilize nonlinear optical phenomena.

The interaction of femtosecond laser pulses with polymers were studied and the conditions for device fabrication were optimized. Various ways for inducing nonlinear response in polymers devices were investigated. The work allowed the group to expand its investigation of femtosecond laser interactions with materials to polymers and create polymer-based photonic devices. The applications of research may extend into other fields, including medicine and engineering.

Femtosecond laser pulses were also used to study ultrafast dynamics in solids, such as zinc oxide, through pump probe experiments. The transient material properties obtained through such experiments can be used to optimize ZnO-based devices. Other dielectric materials, including fused silica and diamond were micromachined and studied under irradiation from femtosecond laser pulses.

Summary of most important results

Dielectric function dynamics during femtosecond laser excitation of bulk ZnO

We measured the dielectric function dynamics of bulk ZnO under femtosecond laser excitation by performing broadband dual-angle pump-probe reflectometry. We find that sub-band-gap below-damage-threshold excitation creates excited electron–hole pairs in ZnO by way of multiphoton absorption. The large population of excited carriers generated from ultrafast laser excitation cause screening of the Coulomb interaction which subsequently damps the exciton resonance and renormalizes the band gap. These changes contribute to broadband changes in the dielectric function of ZnO from 2.5 to 3.5 eV. The observed dynamics in the dielectric function sheds light on how the index of refraction of ZnO changes under ultrafast excitation. From the dielectric function, many transient material properties can be determined to optimize ZnO-based devices.

Ultrafast dynamics of bis (n-butylimido) perylene thin films excited by two-photon absorption

We obtain pump-probe reflectivity spectra of bis (n-butylimido) perylene thin films deposited on Au nanoislands. The observed changes in reflectivity are due to Au-mediated surface plasmon enhancement of two-photon absorption. The reflectivity spectrum reveals depletion of the molecule's ground state and excited state absorption. Our experimental results indicate that the Au nanoislands effectively enhance the two-photon absorption and that they can be used to functionalize organic molecules for device applications.

Three-dimensional fabrication of optically active microstructures containing an electroluminescent polymer

We demonstrate an approach for fabricating three-dimensional microstructures containing the luminescent polymer poly(2-methoxy-5-(2'-ethylhexyloxy)-1,4-phenylenevinylene) (MEH-PPV) using two-photon absorption polymerization. The microstructures present good definition and structural integrity, which is required for photonics devices. Fluorescence microscopy images show that MEH-PPV is retained in the microstructure after the fabrication and that its optical properties are preserved. Fluorescence confocal microscopy images show that the MEH-PPV is distributed not only at the surface, but throughout the bulk of the microstructure, which enhances the luminescence properties of the microstructures. In addition, we demonstrate waveguiding of the MEH-PPV emission in 100 μm long microstructures fabricated on top of porous silica substrates, revealing the feasibility of fabricating photonics devices such as microLEDs and microwaveguides.

Two-photon polymerization for fabricating structures containing the biopolymer chitosan

We demonstrate an approach for fabricating three-dimensional structures containing the biocompatible polymer chitosan with nanometric features, using two-photon polymerization of an acrylic resin doped with the biocompatible polymer chitosan using a guest-host scheme. The structures present good definition and structural integrity (resolution of approximately 700 nm). Raman measurements show that chitosan is incorporated in the structure and is distributed throughout its bulk. The spectra also show that chitosan does not react chemically with the acrylic resin, which is a required condition for biomedical applications, where the acrylic resin must work as a substrate for chitosan without changing its chemical properties. Finally, hardness measurements show that chitosan does not impair the mechanical properties of the resins. Therefore, two-photon polymerization can be used to fabricate three-dimensional structures containing biopolymers, with nanometric features or even on the nanometric scale, which may then be applied in tissue engineering, bone reconstruction, drug delivery, and other biomedical applications.

Numerical aperture dependence of damage and supercontinuum generation from femtosecond laser pulses in bulk fused silica

We studied the role of the numerical aperture (NA) of the external focusing in the interaction of femtosecond laser pulses with transparent materials. We measured the threshold energy for supercontinuum generation and bulk damage in fused silica using numerical apertures (NAs) ranging from 0.01 to 0.65. At a high NA (above 0.25 NA), single-shot, catastrophic damage occurs, and no supercontinuum generation is observed. Below 0.15 NA we observe supercontinuum generation and damage at a threshold significantly above the threshold for supercontinuum generation. The extent of the blue broadening of the supercontinuum spectrum decreases significantly as the NA is increased from 0.01 to 0.08, showing that weak focusing is important for generating the broadest supercontinuum spectrum. Bulk micromachining is only practical for NAs of 0.25 NA and above, where self-focusing effects are minimal and spot size and focal position can be accurately predicted and controlled. Further, as the NA is increased, the energy necessary to cause material modification decreases, minimizing collateral damage. While supercontinuum can be produced at any NA below 0.15 NA, the spectrum is broadest at the lowest NA. Also, at the lowest NA, the supercontinuum is produced well below the damage threshold. Below 0.05 NA we observe multiple refocusing of the femtosecond laser beam. The results presented in this paper show that the NA, a linear optical parameter which is independent of the laser parameters, controls the interaction of ultrashort laser pulses with transparent materials, a highly nonlinear process.

Reversible birefringence in microstructures fabricated by two-photon absorption polymerization

We demonstrate the fabrication of birefringent microstructures using two-photon absorption polymerization. The birefringence is caused by a light-driven molecular orientation of azoaromatic molecules (Disperse Red 13) upon excitation with an Ar⁺ laser at 514.5 nm. For the optimum compositions for two-photon absorption polymerization and optically induced birefringence of 70% (by weight) of monomer A, 26% monomer B, 3% photoinitiator, and 1% Disperse Red 13, we obtain a birefringence of 5×10^{-5} . This birefringence can be completely erased by overwriting the test spot with circularly polarized laser light or by heating the sample close to the polymer glass transition temperature. Our results open the door to the development of alternative applications in optical data storage, waveguiding, and optical circuitry.

Faraday rotation in femtosecond laser micromachined waveguides

We demonstrate magneto-optic switching in femtosecond-laser micromachined waveguides written inside bulk terbium-doped Faraday glass. By measuring the polarization phase shift of the light as a function of the applied magnetic field, we find that there is a slight reduction in the effective Verdet constant of the waveguide compared to that of bulk Faraday glass. The change is not significant and the micromachined waveguides can be used as magneto-optic switches. Electron Paramagnetic Resonance (EPR) measurements confirm that the micromachining does not convert a significant fraction of the active Tb³⁺ ions into Tb⁴⁺ ions, leaving the concentration of the terbium ions that are responsible for the Faraday effect virtually unchanged. These findings pave the way for light-by-light magneto-optic switching and integrated optical isolators.

Two-photon absorption spectrum of the photoinitiator Lucirin TPO-L

Recently, Lucirin TPO-L was shown to be a photoinitiator with several advantageous properties for two-photon induced polymerization. We measured the two-photon absorption cross-section spectrum of Lucirin T-POL in the wavelength range from 600 to 810 nm using the Z-scan technique. The maximum value of two-photon absorption cross-section is 1.2GM at 610 nm, which is low compared to some organic molecules, but comparable to other photoinitiators reported in the literature. Using quantum-chemical calculations we established that the low nonlinear optical properties of this molecule arise from its nonplanarity and low conjugation length.

Despite the small two-photon absorption cross-section exhibited by Lucirin TPO-L, its high polymerization quantum yield permits the fabrication of microstructures with excellent structural integrity and definition, demonstrating the potential of Lucirin TPO-L for microfabrication by two-photon polymerization. These results indicate that optimization of the two-photon absorption cross-section is not the only material parameter to be considered when searching for new photoinitiators for microfabrication via two-photon absorption.

Femtosecond laser micromachining in the conjugated polymer MEH-PPV

Femtosecond-laser micromachining of poly[2-methoxy-5-(20-ethylhexyloxy)-p-phenylene vinylene] films was investigated using 130 fs pulses at 800 nm from a laser oscillator operating at 76 MHz repetition rate. We investigated the effect of pulse energy and translation speed on the depth and morphology of the micromachined regions.

For pulse energies higher than 1.2 nJ, film removal from the glass substrate occurs. Below 1.2 nJ only superficial material removal occurs, with a maximum groove depth of 30 nm. Furthermore, we demonstrated that although photobleaching occurs during the micromachining process, for the energy regime up to 1.2 nJ, the optical properties of the polymer remain unchanged. The results presented in this paper provide the optimum parameters for fs-laser micromachining of MEH-PPV for applications in polymeric-based photonic devices.

3D cell-migration studies using two-photon engineered polymer scaffolds

We conducted cell-migration studies in engineered polymer scaffolds fabricated by two-photon polymerization. We developed a model three-dimensional (3D) extracellular matrix that provides precise and independent control of architectural parameters and that can be used for controlled cell adhesion and migration studies. We find that the 3D environment produces higher cell speeds than a 2D substrate. As the pore size of the 3D matrix is decreased, we observe a decrease in mean speed due to obstruction from the matrix. The fabrication and analysis techniques we use open the door to systematic studies of the effects of mechanical properties, adhesion peptide concentration, and biodegradability on cell migration in three-dimensional environments.

Femtosecond laser waveguide micromachining of PMMA films with azoaromatic chromophores

We show that fs-laser waveguide micromachining is possible in azochromophore doped poly(methyl methacrylate) (PMMA) films. The micromachining results from two-photon absorption by the azochromophores at 800 nm. We determined the laser and sample parameters for micromachining PMMA samples doped with the azochromophores Disperse Red 1, Disperse Red 13, and Disperse Orange 3. Although we observe photobleaching of the azochromophores during micromachining, our results show that a significant amount of azochromophores remains unbleached. Finally, we fabricated optical waveguides in bulk PMMA doped with Disperse Red 1, demonstrating single-mode waveguiding in doped polymers.

Femtosecond laser-induced formation of nanometer-width grooves on synthetic single-crystal diamond surfaces

We demonstrated the fabrication of long nanometer-width grooves on synthetic single-crystal CVD diamond surfaces by femtosecond laser irradiation at 800 nm. The grooves are 40 nm wide, 500 nm deep, up to 0.3 mm long, and have an average spacing of 146 nm. The grooves are perpendicular to the direction of the laser polarization and are formed below the threshold for ablation throughout the focal volume. Their aspect ratio is larger than twelve and their shape is quite uniform at the nanometer scale. We used this technique to fabricate grooves of approximately 300 μm long and parallelepiped-shaped pillar structures with submicrometer dimensions. Raman spectroscopy confirms that the structures maintain the original diamond composition. The submicrometer periodicity is caused by interference between a laser-induced plasma and the incident laser beam, which locally enhances the field at the surface so the ablation threshold is exceeded. This process provides a high-speed and low-cost method for fabricating submicrometer devices such as optical gratings or nanoimprint molds in diamond.

Optical loss measurements in femtosecond laser written waveguides in glass

The optical loss is an important parameter for waveguides used in integrated optics. We measured the optical loss in waveguides written in silicate glass slides with high repetition-rate (MHz) femtosecond laser pulses. The average transmission loss of straight waveguides is about 0.3 dB/mm at a wavelength of 633 nm and 0.05 dB/mm at a wavelength of 1.55 μm . The loss is not polarization dependent and the waveguides allow a minimum bending radius of 36 mm without additional loss. The average numerical aperture of the waveguides is 0.065 at a wavelength of 633 nm and 0.045 at a wavelength of 1.55 μm . In straight waveguides more than 90% of the transmission loss is due to scattering.

Bibliography

Dielectric function dynamics during femtosecond laser excitation of bulk ZnO

Shih T, Winkler MT, Voss T, et al.

Applied Physics A, 96, 2, 363-367 (2009).

Ultrafast dynamics of bis (n-butylimido) perylene thin films excited by two-photon absorption

Mendonca CR, Kandyla M, Shih T, Aroca RF, Constantino CJL, Mazur E

Applied Physics A, 96, 2, 369-372 (2009).

Three-dimensional fabrication of optically active microstructures containing an electroluminescent polymer

Mendonca CR, Correa DS, Marlow F, Voss T, Tayalia P, Mazur E

Applied Physics Letters, 95, 11 (2009).

Two-Photon Polymerization for Fabricating Structures Containing the Biopolymer Chitosan

Correa DS, Tayalia P, Cosendey G, dos Santos DS, Aroca RF, Mazur E, Mendonca CR

Journal of Nanoscience and Nanotechnology, 9, 10, 5845-5849 (2009).

Numerical aperture dependence of damage and supercontinuum generation from femtosecond laser pulses in bulk fused silica

Jonathan B. Ashcom, Rafael R. Gattass, Chris B. Schaffer and Eric Mazur

J. Opt. Soc. Am. B, 23, 2317-2322 (2006).

Reversible birefringence in microstructures fabricated by two-photon absorption polymerization

Cleber Mendonca, Tommaso Baldacchini, Prakriti Tayalia and Eric Mazur

J. Appl. Phys., 103, 013109-1-013109-4 (2007).

Faraday rotation in femtosecond laser micromachined waveguides

Tina Shih, Rafael R. Gattass, Cleber R. Mendonca and Eric Mazur

Opt Express, 15, 5809-5814 (2007).

Two-photon absorption spectrum of the photoinitiator Lucirin TPO-L

C. R. Mendonca, D. S. Correa, T. Baldacchini, P. Tayalia and E. Mazur

Appl. Phys. A, 90, 633-636 (2008).

Femtosecond laser micromachining in the conjugated polymer MEH-PPV

C. R. Mendonca, S. Orlando, G. Cosendey, M. T. Winkler and E. Mazur

Applied Surface Science, 254, 1135-1139 (2007).

3D cell migration studies using two-photon engineered polymer scaffolds

Prakriti Tayalia, Cleber Mendonca and Eric Mazur

Advanced Materials, 20, 4494-4498 (2008).

Femtosecond laser waveguide micromachining of PMMA films with azoaromatic chromophores

Cleber R. Mendonca, Tina Shih and Eric Mazur

Opt. Express, 16, 200-206 (2008).

Femtosecond laser-induced formation of nanometer-width grooves on synthetic single-crystal diamond surfaces

Shinoda M, Gattass RR, Mazur E

Journal of Applied Physics, 105, 5 (2009).

Optical loss measurements in femtosecond laser written waveguides in glass

Limin Tong, Rafael R. Gattass, Iva Zaharieva Maxwell, Jonathan B. Ashcom and Eric Mazur

Opt. Commun., 259, 626-630 (2006).

Femtosecond laser micromachining in transparent materials

Rafael Gattass and Eric Mazur

Nat. Phot., 2, 219-225 (2008).

Appendix A: Peer-reviewed publications

Dielectric function dynamics during femtosecond laser excitation of bulk ZnO

T. Shih · M.T. Winkler · T. Voss · E. Mazur

Received: 8 December 2008 / Accepted: 3 March 2009 / Published online: 25 March 2009
© Springer-Verlag 2009

Abstract Using a broad band dual-angle pump-probe reflectometry technique, we obtained the ultrafast dielectric function dynamics of bulk ZnO under femtosecond laser excitation. We determined that multiphoton absorption of the 800-nm femtosecond laser excitation creates a large population of excited carriers with excess energy. Screening of the Coulomb interaction by the excited free carriers causes damping of the exciton resonance and renormalization of the band gap causing broadband (2.3–3.5 eV) changes in the dielectric function of ZnO. From the dielectric function, many transient material properties, such as the index of refraction of ZnO under excitation, can be determined to optimize ZnO-based devices.

PACS 81.05.Dz · 78.47.J

1 Introduction

Zinc oxide (ZnO) is a wide-band-gap semiconductor that has recently gained renewed interest as an ideal material system for the development of optoelectronic devices and lasing media in the blue-to-near-UV spectral region [1, 2]. Known for its large band gap and large exciton binding energy [2, 3], ZnO can easily be handled to yield uniform and

high-quality ZnO nanostructures and its fabrication does not require toxic precursors [4–6]. In order to better understand ZnO and its relevant properties for optoelectronic applications, it is necessary to know the carrier dynamics in ZnO after excitation with intense ultrafast laser pulses.

Under intense ultrafast excitation, semiconductors undergo dramatic changes because the induced high carrier density can cause heating, melting, ablation, and resolidification, which permanently modify the morphology of the material [7–10]. Figure 1 shows an example of the permanent surface modification in ZnO after exposure to high-intensity ultrashort laser pulses. While typical ZnO-based applications do not require permanent changes in the material, most applications involve a large population of excited carriers. The performance of lasers and waveguides, for example, depend strongly on the carrier density and other material properties. It is therefore necessary to understand how ZnO behaves under high carrier densities over time in order to optimize ZnO-based devices. While the nonlinear optical properties of ZnO under ultrashort laser irradiation have been investigated [11–13], there are no studies on the related timescales and broadband dynamics of the large population of excited carriers in ZnO after ultrafast laser excitation. Characterization of ZnO under high-excitation conditions not only provides additional information on the excitation, thermalization, scattering, and recombination of the carriers, but also reveals how high carrier densities affect the dielectric function of ZnO.

In this paper, we perform systematic time and energy resolved pump-probe studies that yield the time-resolved ZnO dielectric function after excitation with femtosecond laser pulses [14]. The data suggests that excitation with femtosecond laser pulses of sub-band-gap photon energy creates a large number of free carriers. The generated free carriers

T. Shih (✉) · M.T. Winkler · T. Voss · E. Mazur
Department of Physics and School of Engineering and Applied Sciences, Harvard University, 9 Oxford Street, Cambridge, MA 02138, USA
e-mail: tinashih@fas.harvard.edu

T. Voss
Institute of Solid-State Physics, University of Bremen, Bremen, Germany

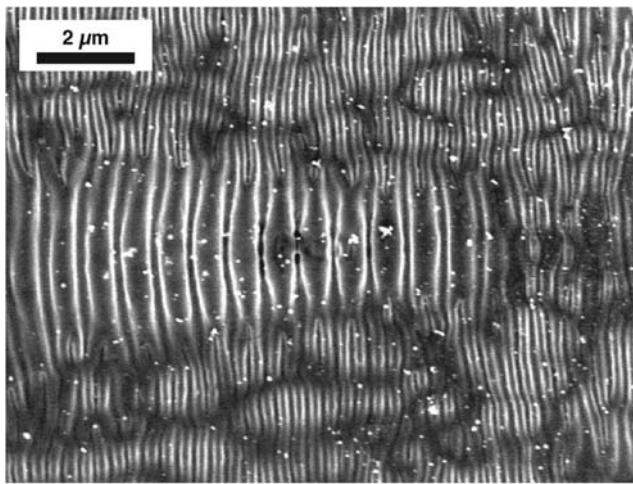
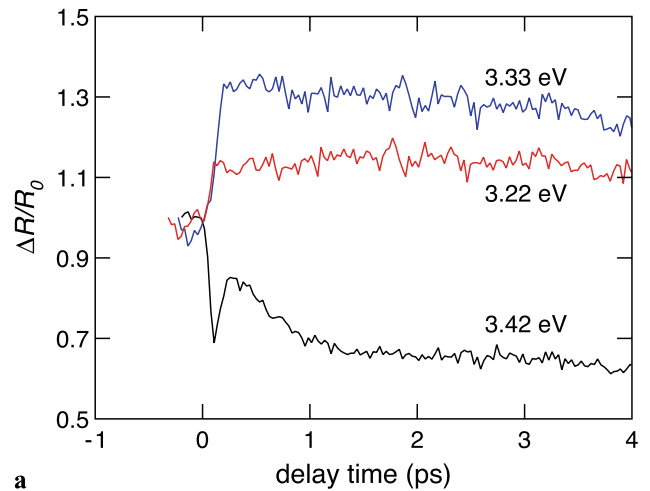


Fig. 1 SEM image of femtosecond laser-structured bulk ZnO

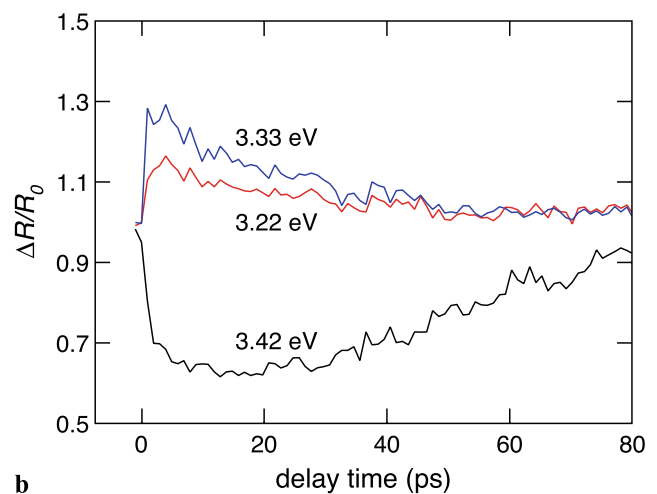
cause screening of the Coulomb interaction which subsequently damps the exciton resonance and renormalizes the band gap causing broad band (2.3–3.5 eV) changes in the dielectric function of ZnO. Information about the dielectric function yields a number of pertinent material properties of ZnO, including the change in the index of refraction as a function of time after fs laser excitation. The measurement of the dielectric function and the index of refraction during and after intense excitation enables a better understanding of the carrier dynamics in highly excited ZnO, which in turn will permit optimizing the design of ZnO-based devices [15–19].

2 Experimental details

We performed dual-angle-of-incidence pump-probe spectroscopy to measure the changes in the reflectivity and invert the data into the transient dielectric function [14] of ZnO under ultrafast laser excitation. Using a multipass amplified Ti:sapphire laser (0.5-mJ pulse energy, 40-fs pulse width, 1-kHz repetition rate), we excite the *c*-plane of a crystalline ZnO sample under normal atmosphere and room temperature conditions. The pump pulse, centered at 800 nm, had a fluence of 2.5 kJ/m², just below the ZnO damage threshold of 3.0 kJ/m². The excitation fluence used to obtain reflectivity and dielectric function dynamics is different from the above-damage-threshold excitation fluence of 4.0 kJ/m² used to laser structure the surface of bulk ZnO (Fig. 1). Focusing the laser pulse through a CaF₂ crystal, we generate a broadband (1.5–3.5 eV) probe pulse to detect reflectivity changes of the excited ZnO at different pump-probe delay times. Using the reflectivity data measurements taken at multiple angles of incidence, we reconstruct the time-resolved dielectric function of the highly excited ZnO [14].



a



b

Fig. 2 Ultrafast reflectivity of bulk ZnO for an excitation fluence of 2.5 kJ/m² at three different photon energy ranges: above band gap energy 3.42 eV (*black*); at the exciton resonance energy 3.33 eV (*blue*); and below the band gap energy—3.25 eV. Reflectivity is plotted as a function of pump-probe delay time (**a**) from −1 to 4 ps in steps of 33 fs and (**b**) from −2 to 80 ps in steps of 1 ps

3 Results

We measured the ultrafast reflectivity response at photon energies from 1.5 to 3.5 eV for an excitation fluence of 2.5 kJ/m². Figure 2a shows the reflectivity data as a function of delay time (0–4 ps) at three characteristic photon energy ranges: below the band gap at 3.25 eV (red line), at the exciton resonance of 3.32 eV (blue line), and above the band gap at 3.42 eV (black line). For all three energies, the reflectivity data show a fast response over several hundred femtoseconds followed by a slower decay back towards equilibrium over several tens of picoseconds. Below the band-gap energy, the reflectivity takes 200 fs to increase by 15% and then decays after 3 ps. At the exciton resonance, the reflectivity sharply increases by 40% over 200 fs and decays

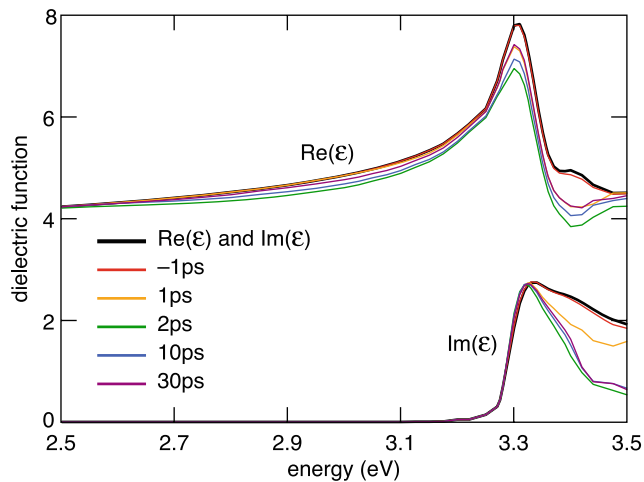


Fig. 3 Dielectric function of ZnO as a function of energy (2.5–3.5 eV) for various pump-probe delay times after excitation from

immediately thereafter. Above the band-gap energy, the reflectivity sharply decreases by 30% within 150 fs, recovers halfway after 250 fs, and then continues to decrease on a longer timescale. Figure 2b depicts the reflectivity dynamics over a longer time window (–2 to 80 ps) and shows that the reflectivity for energies above the band gap starts to increase back towards unexcited ZnO reflectivities after 20 ps. In addition, complete recovery occurs within 150 ps for all photon energies thus indicating that the measurements are below the damage threshold and can be repeated.

From the dual-angle broadband reflectivity measurements we can extract the time-resolved dielectric function of the highly excited ZnO [14]. Figure 3 shows the resulting real and imaginary components of the dielectric function of ZnO at different pump-probe delay times. For reference, the black line represents the linear dielectric function of the sample, as measured using ellipsometry. The ultrafast dynamics of the dielectric function is plotted for different delay times ranging from –1 to 30 ps after excitation. For energies above the band gap, the real and imaginary parts of the dielectric function decrease by 25% within the first few hundred femtoseconds. Excitation effects can be seen for delay times well beyond a few picoseconds and for photon energies far below 3 eV. In particular, a decrease in the real part of the dielectric function stretches from 3.5 eV down to at least 2.5 eV. Near the exciton resonance (3.31 eV) the real part shows a 25% decrease of the resonance from 7.8 to 6.9 as well as a large decrease from 4.9 to 3.8 at 3.4 eV. The imaginary part shows an initial decrease from 2.2 to 0.7 at energies above resonance, followed by a recovery after 2 ps. The data also show a redshift of the maximum of the imaginary part of about 15–20 meV.

4 Discussion

Because the pump photon energy (1.55 eV) is well below 3.35 eV, the room-temperature band gap of ZnO, multiphoton processes are required to induce interband transitions. We measured the ZnO photoluminescence and found the multiphoton process to have a higher contribution from two-photon absorption than three-photon absorption, even though the energy of two photons is not quite enough to bridge the band gap. This finding is in agreement with reports in literature, because the cross section of two-photon absorption is much larger than that of three-photon absorption [11], most likely due to electric-field-assisted two-photon absorption caused by the high electric fields in the amplified femtosecond laser pulses [20]. Evidence of multiphoton absorption can also be seen in the periodic structures on the surface of ZnO, generated by 800-nm above-damage-threshold laser excitation (Fig. 1). These features, which are often observed on material surfaces upon exposure to short pulse irradiation, have a spacing of λ or λ/n , where λ is the incident laser wavelength and n is an integer [21, 22]. During femtosecond laser structuring of ZnO, we observe emission at $\lambda = 800$ and 400 nm indicating that second-harmonic generation, a common phenomenon upon ultrafast excitation of a highly polar semiconductor like ZnO [23], occurs at the surface. The presence of ZnO surface feature sizes that correspond to these wavelengths indicates that the absorption causing the structuring must be nonlinear.

The reflectivity measurements in Fig. 2 reveal three timescales in the dynamics of photoexcited ZnO. The first timescale is the fast initial 200-fs reflectivity change resulting from multiphoton absorption of the incident 800-nm pulses. Multiphoton absorption creates a large number of highly excited electron–hole pairs that occupy states well above the conduction band edge. Above the band gap, at 3.42 eV, the reflectivity shows temporary decrease on this timescale, which we attribute to pump-induced nonlinear absorption [12, 24]. Around zero time delay in pump-probe spectroscopy studies, a pump photon may have the opportunity to interact with one or more probe photons inducing a nonlinear absorption and creating a large reflectivity decrease that disappears after about two pulse widths in time [12, 24].

The second timescale is on the order of 1 ps and is associated with the time required for the hot carriers to reach a quasithermal equilibrium [25]. This 1-ps timescale is most visible for the above band gap energy reflectivities (Fig. 2a, black line) because this energy range probes the hot carriers that relaxing down to states near the exciton resonance.

About 20 ps after excitation a third timescale emerges in the reflectivity data (Fig. 2b). Starting at about 20 ps the reflectivity gradually reverts to the value for unexcited ZnO.

Indeed, this timescale correlates well with recombination timescales obtained from photoluminescence measurements in ZnO [26]. The reflectivity completely returns to the reflectivity of unexcited ZnO in about 150 ps. The 150-ps timescale agrees with previous work, which reports a carrier recombination time in ZnO of about 100–300 ps [27, 28].

The dielectric function of ZnO shown in Fig. 3 provides additional detail on the interaction of ultrafast laser excitation with ZnO revealing how multiphoton absorption of the pump affects the carriers, how excited carriers affect the exciton resonance, and how excitation affects the material response. The femtosecond laser excitation creates a large concentration of free electron–hole pairs via multiphoton absorption of 800-nm photons. The initial decrease in both the real and imaginary components of the dielectric function above 3.35 eV is indicative of an increase of carrier concentration at energies above the conduction band minimum. The high density of free electron–hole pairs significantly screen the Coulomb interaction and damp the exciton resonance, as evidenced by the 20% decrease of the real part of the dielectric function at 3.33 eV in Fig. 3. Immediately after excitation, the imaginary part near 3.33 eV shows a small 20-meV redshift which we can attribute to a reduction of the band gap due to Coulomb screening [19, 20]. At time delays of 1–2 ps the carriers have thermalized, and over tens of picoseconds the carrier relax through LO phonons [12] restoring the dielectric function to that of unexcited ZnO.

The dielectric function data can be used to obtain the transient behavior of other material properties, such as the index of refraction. Knowing how the index of refraction is affected by high carrier concentrations is important for modeling and designing ZnO devices. Previous studies on ultrafast laser excitation of ZnO waveguides [18, 29] and ZnO-based lasers [16, 19] revealed an unexpected blueshift of the waveguide or cavity modes relative to calculated models. These unexpected mode changes may be due to a change in the index of refraction of ZnO induced by the laser excitation. From the dielectric function data, we see that the changes in the real part are largest (about 20%) near the band gap (3.33 eV) which implies that there is also a large change in the index of refraction near the band gap.

5 Conclusion

In summary, we measured the dielectric function dynamics of bulk ZnO under femtosecond laser excitation by performing broadband dual-angle pump-probe reflectometry. We find that sub-band-gap below-damage-threshold excitation creates excited electron–hole pairs in ZnO by way of multiphoton absorption. The large population of excited carriers generated from ultrafast laser excitation cause screening of the Coulomb interaction which subsequently damps

the exciton resonance and renormalizes the band gap. These changes contribute to broadband changes in the dielectric function of ZnO from 2.5 to 3.5 eV. The observed dynamics in the dielectric function sheds light on how the index of refraction of ZnO changes under ultrafast excitation.

Acknowledgements Several people contributed to the work described in this paper. T.V. conceived of the basic idea for this work. M.W., T.S., T.V. designed and carried out the experiments and analyzed the results. E.M. supervised the research and the development of the manuscript. This work was carried out with the financial support of the National Science Foundation under contract DMI-0334984 and the Army Research Office under contract W911NF-05-1-0471. T.S. and M.W. would like to acknowledge support from NSF Graduate Research Fellowship, and T.V. acknowledges support from the German Research Foundation (DFG) under contract VO1265/3.

References

1. C. Klingshirn, R. Hauschild, H. Priller, M. Decker, J. Zeller, H. Kalt, *Superlattices Microstruct.* **38**, 209 (2005)
2. D.C. Look, *Mater. Sci. Eng. B-Solid State Mater. Adv. Technol.* **80**, 383 (2001)
3. H. Yoshikawa, S. Adachi, *Jpn. J. Appl. Phys. Part 1-Regul. Pap. Short Notes Rev. Pap.* **36**, 6237 (1997)
4. C. Borchers, S. Muller, D. Stichtenoth, D. Schwen, C. Ronning, *J. Phys. Chem. B* **110**, 1656 (2006)
5. Y. Huang, X.F. Duan, C.M. Lieber, *Small* **1**, 142 (2005)
6. P.J. Pauzauskie, P. Yang, *Mater. Today* **9**, 36 (2006)
7. A. Cavalleri, C. Toth, C.W. Siders, J.A. Squier, F. Raksi, P. Forget, J.C. Kieffer, *Phys. Rev. Lett.* **87**, 401 (2001)
8. C. Guo, G. Rodriguez, A. Lobad, A.J. Taylor, *Phys. Rev. Lett.* **84**, 4493 (2000)
9. P.N. Saeta, J.K. Wang, Y. Siegal, N. Bloembergen, E. Mazur, *Phys. Rev. Lett.* **67**, 1023 (1991)
10. K. Sokolowski-Tinten, J. Solis, J. Bialkowski, J. Siegel, C.N. Alfonso, D.v.d. Linde, *Phys. Rev. Lett.* **81**, 3679 (1998)
11. D.C. Dai, S.J. Xu, S.L. Shi, M.H. Xie, C.M. Che, *Opt. Lett.* **30**, 3377 (2005)
12. C.K. Sun, S.Z. Sun, K.H. Lin, K.Y.J. Zhang, H.L. Liu, S.C. Liu, J.J. Wu, *Appl. Phys. Lett.* **87** (2005)
13. X.J. Zhang, W. Ji, S.H. Tang, *J. Opt. Soc. Am. B-Opt. Phys.* **14**, 1951 (1997)
14. C.A.D. Roeser, A.M.T. Kim, J.P. Callan, L. Huang, E.N. Glezer, Y. Siegal, E. Mazur, *Rev. Sci. Instrum.* **74**, 3413 (2003)
15. J.M. Bao, M.A. Zimmler, F. Capasso, X.W. Wang, Z.F. Ren, *Nano Lett.* **6**, 1719 (2006)
16. A.B. Djuricic, W.M. Kwok, Y.H. Leung, W.K. Chan, D.L. Phillips, M.S. Lin, S. Gwo, *Nanotechnology* **17**, 244 (2006)
17. R. Hauschild, H. Lange, H. Priller, C. Klingshirn, R. Kling, A. Waag, H.J. Fan, M. Zacharias, H. Kalt, *Phys. Status Solidi B-Basic Solid State Phys.* **243**, 853 (2006)
18. J.C. Johnson, H.Q. Yan, P.D. Yang, R.J. Saykally, *J. Phys. Chem. B* **107**, 8816 (2003)
19. J.K. Song, J.M. Szarko, S.R. Leone, S.H. Li, Y.P. Zhao, *J. Phys. Chem. B* **109**, 15749 (2005)
20. Z.W. Dong, C.F. Zhang, G.J. You, X.Q. Qiu, K.J. Liu, Y.L. Yan, S.X. Qian, *J. Phys.-Condens. Matter* **19** (2007)
21. J.E. Sipe, J.F. Young, J.S. Preston, H.M.v. Driel, *Phys. Rev. B* **27**, 1141 (1983)
22. J.E. Young, J.S. Preston, H.M.v. Driel, J.E. Sipe, *Phys. Rev. B* **27**, 1155 (1983)

23. U. Neumann, R. Grunwald, U. Griebner, G. Steinmeyer, W. Seiber, *Appl. Phys. Lett.* **84**, 170 (2004)
24. K.H. Lin, G.W. Chern, Y.C. Huang, S. Keller, S.P. DenBaars, C.K. Sun, *Appl. Phys. Lett.* **83**, 3087 (2003)
25. A. Yamamoto, T. Kido, Y.F. Goto, Y. Chen, T. Yao, A. Kasuya, *Appl. Phys. Lett.* **75**, 469 (1999)
26. T. Voss, L. Wischmeier, J. Nanosci. Nanotechnol. **8**, 228 (2008)
27. J.C. Johnson, K.P. Knutsen, H.Q. Yan, M. Law, Y.F. Zhang, P.D. Yang, R.J. Saykally, *Nano Lett.* **4**, 197 (2004)
28. D.C. Reynolds, D.C. Look, B. Jogai, J.E. Hoelscher, R.E. Sherriff, M.T. Harris, M.J. Callahan, *J. Appl. Phys.* **88**, 2152 (2000)
29. R. Hauschild, H. Kalt, *Appl. Phys. Lett.* **89** (2006)

Ultrafast dynamics of bis (*n*-butylimido) perylene thin films excited by two-photon absorption

C.R. Mendonca · M. Kandyla · T. Shih · R.F. Aroca ·
C.J.L. Constantino · E. Mazur

Received: 21 October 2008 / Accepted: 3 March 2009 / Published online: 21 March 2009
© Springer-Verlag 2009

Abstract We report a pump-probe study of the two-photon induced reflectivity changes in bis (*n*-butylimido) perylene thin films. To enhance the two-photon excitation we deposited bis (*n*-butylimido) perylene films on top of gold nanoislands. The observed transient response in the reflectivity spectrum of bis (*n*-butylimido) perylene is due to a depletion of the molecule's ground state and excited state absorption.

PACS 78.40.Me · 78.47.J · 42.65.Re

1 Introduction

Perylene tetracarboxylic derivatives (PTCD) are a class of organic molecules that can function as organic semiconductors suitable for device applications [1–4]. The strong absorption and emission of PTCD in the visible region [5], and their thermal and chemical stability [6, 7], make them

prime candidates for optoelectronic devices, such as photoconductors, solar cells [8], and laser materials [9]. It has recently been reported that PTCD possess extremely large two-photon absorption cross sections [10–12] making them ideal for photonic applications, such as upconversion lasing and high-efficiency optical limiting.

A major challenge in developing organic-molecule-based photonic devices is the high intensity threshold required for inducing optical nonlinearities. To increase optical nonlinearities in organic molecules one can use electromagnetic-field enhancement produced by surface plasmons in nanoparticles [13]. Such surface plasmon resonances have been applied to Raman scattering [14, 15] and more recently to two-photon absorption [13, 16, 17]. The enhancement factor depends strongly on the shape, size, and type of metal particles, the incident excitation wavelength, and the permittivity of the material surrounding the organic molecule.

In PTCD, enhancement of the local electromagnetic field induced by surface plasmon resonance has been observed by way of Raman scattering [14, 18, 19], electronic emission [7], and vibrational absorption [20]. Among several different forms of PTCD, the bis (*n*-butylimido) perylene tetracarboxylic derivative (BuPTCD) has attracted special attention not only because of its optoelectronic properties but also because it possesses an absorption band in a conveniently accessible range. The BuPTCD absorption band partially overlaps with the absorption band tail of common metals used for surface-enhancement, including Cu, Ag, and Au. This partial overlap of the band tails allows the enhancement of optical effects, such as two-photon absorption, while maintaining spectrally distinct maxima for both the metal absorption band and the organic absorption band.

Although the structural, electronic, and optical properties of PTCDs have been studied [4, 7, 21–23], the dynam-

C.R. Mendonca · M. Kandyla · T. Shih (✉) · E. Mazur
Department of Physics and School of Engineering and Applied
Sciences, Harvard University, 9 Oxford Street, Cambridge,
MA 02138, USA
e-mail: tinashih@fas.harvard.edu

C.R. Mendonca
Instituto de Física de São Carlos, Universidade de São Paulo,
Caixa Postal 369, 13560-970 São Carlos, SP, Brazil

R.F. Aroca
Materials and Surface Science Group, University of Windsor,
Windsor, ON, N9B 3P4, Canada

C.J.L. Constantino
DFQB, Faculdade de Ciências e Tecnologia, UNESP, 19060-900
Presidente Prudente, SP, Brazil

ics resulting from two-photon excitation of these molecules have yet to be determined. In this paper, we report on a femtosecond pump-probe study of BuPTCD films deposited by physical vapor deposition on top of nanometric Au islands on glass substrates. The transient reflectivity of BuPTCD, resulting from two-photon excitation enhanced by surface plasmon resonance, reveals dynamics on the picosecond timescale.

2 Experimental details

The bis (*n*-butylimido) perylene (BuPTCD) used in this work was synthesized by the condensation of appropriate amines with perylene tetracarboxylic dianhydride. The BuPTCD molecular structure is shown in the inset of Fig. 1a.

The data presented here were obtained on two 100-nm-thick BuPTCD films; one was evaporated on top of a glass substrate (BuPTCD thin film) and the other was evaporated on Au nanoislands on top of a glass substrate (Au-BuPTCD thin film). The Au nanoislands were obtained by coating glass slides with a 6-nm-thick Au film, deposited by evaporation at a rate of about 0.05 nm/s. Both the BuPTCD and the metal films were evaporated with the substrates at room temperature, at a pressure of 10^{-8} Pa using an evaporator ma-

chine equipped with quartz crystal oscillator for film thickness determination. We measured the samples' absorbance from 350 to 800 nm with a spectrophotometer.

We performed pump-probe reflectometry experiments on the films using a multipass amplified Ti:sapphire laser system which produces 0.5-mJ, 40-fs pulses at a repetition rate of 1 kHz. The sample is excited by a train of 800-nm *s*-polarized pulses focused into a 100- μ m-diameter spot at the sample, with the pulse energy below the threshold for permanent damage. To measure the time-resolved reflectivity we use a *p*-polarized white-light (350–730 nm) probe, obtained by focusing part of the femtosecond laser output onto a 3-mm-thick piece of CaF₂ [24]. We measured the chirp of the white-light probe separately and corrected the reflectivity data accordingly, as described in Ref. [24].

For the Au-BuPTCD sample we used an excitation energy of 0.44 μ J, about half of the damage threshold, which was determined to be 0.87 μ J. These energies are small compared to the 11.5- μ J damage threshold for the BuPTCD sample indicating that the presence of Au nanoislands significantly increases the absorption of 800-nm laser irradiation.

3 Results

The dashed line in Fig. 1a shows the absorption spectrum for BuPTCD in solution. The spectrum exhibits a π – π^* electronic absorption band around 500 nm (*S*₁ state), with absorption peaks separated by approximately 170 meV corresponding to the vibrational progression of the electronic absorption [7, 21, 25].

The absorption spectrum of the BuPTCD film evaporated on glass (solid line in Fig. 1a) looks different from the spectrum of BuPTCD in solution because the molecules have fewer degrees of freedom in the thin film than when they are suspended. Compared to the solution, the thin film shows a redshifted component with a broad maximum at 572 nm and a blueshifted component centered at 466 nm. The observed band shifts and the double absorption peaks are attributed to the “card pack” (H aggregate \rightarrow blueshift) and “head-to-tail” (J aggregate \rightarrow redshift) arrangement of the chromophores [26].

Figure 1b shows the absorption spectrum for the Au-BuPTCD film (solid line). The reference spectrum used to calibrate this Au-BuPTCD film absorption spectrum was obtained with a glass slide. Compared to the linear absorption spectrum of the BuPTCD film in Fig. 1a, the Au-BuPTCD spectrum in Fig. 1b is blueshifted by about 20 nm, and there is an overall increase in absorbance. The dashed line in Fig. 1b shows the surface-plasmon absorption peaks of the Au nanoislands alone broadened by the wide range of sizes and shapes of the deposited islands on the glass substrate.

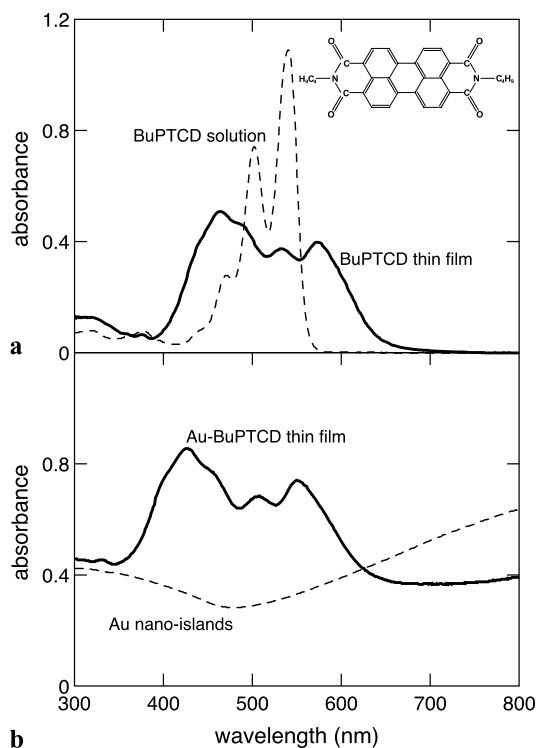


Fig. 1 Absorbance spectra of (a) BuPTCD in solution (dashed line) and a BuPTCD thin film evaporated onto a glass slide (solid line), (b) a BuPTCD thin film evaporated onto Au nanoislands deposited on a glass slide (solid line) and Au nanoislands on a glass slide (dashed line). The inset shows a diagram of the BuPTCD molecule

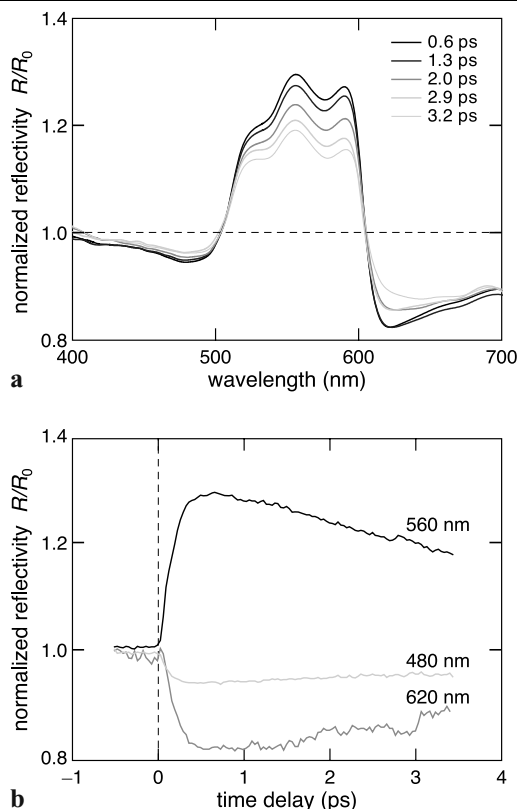


Fig. 2 Normalized reflectivity, R/R_0 , of Au-BuPTCD (**a**) as a function of probe wavelength at various delay times and (**b**) as a function of time delay at three different wavelengths

The BuPTCD spectra in Fig. 1 clearly show that the 800-nm laser excitation wavelength is nonresonant with the electronic absorption spectra, a necessary condition to observe a two-photon induced process. However, the 800-nm laser line is in resonance with the broad surface plasmon absorption of the Au nanoislands. This condition is necessary to activate the surface-plasmon enhancement mechanisms in the organic molecule [27].

Figure 2a shows the transient reflection spectrum of Au-BuPTCD as a function of the probe beam wavelength, at probe delays of 600 fs, 1.3, 2.0, 2.9, and 3.2 ps. Note that as the delay time changes the shape of the Au-BuPTCD reflectivity spectra does not undergo significant changes. Reflectivity data at time delays less than 500 fs are not shown, as they tend to exhibit contributions from coherent artifacts during pulse overlap and from the vibration relaxation of the perylene molecules [4, 21, 22, 28, 29].

Figure 2b shows normalized reflectivity, R/R_0 as a function of the time delay between the pump and probe pulses, for three selected probe wavelengths representing the three distinct regions observed in the transient spectrum of Fig. 2a. For these three regions the transient reflectivity of Au-BuPTCD shows: (1) around 550 nm: an increase in reflectivity which reaches a maximum about 500 fs after excitation

and subsequently decays on a 10 ps timescale; (2) around 620 nm: an initial decrease in reflectivity with a characteristic relaxation time of about 10 ps; (3) around 490 nm: a decrease in reflectivity with a slower recovery time of about 30 ps.

4 Discussion

The reflectivity spectra in Fig. 2a present the same profile for different delay times indicating that we are probing the response of a single state of the perylene molecules (the S_1 state) to the excitation. As the reflectivity signal around 550 nm (Fig. 2a) resembles the linear absorption spectrum of the Au-BuPTCD (Fig. 1b solid line), we attribute the increase in reflectivity to depletion of the S_0 ground state. From Fig. 2b, one can see that the ground state is depleted within 500 fs of the excitation and recovers in 300 ps. The other two spectral regions of interest are at wavelengths above 600 nm and below 490 nm, where the decrease in reflectivity can be attributed to excitation of the perylene molecules from S_1 to a higher energy state, in agreement with results presented on transmission pump-probe experiments [4, 21, 22].

Our results also indicate that the two-photon induced reflectivity changes of the Au-BuPTCD films depend strongly on the presence of Au nanoislands. We observed no transient signal in the BuPTCD film on plain glass substrates, even for pulse energies as high as 4.4 μ J, ten times higher than that used for the Au-BuPTCD film. Additionally, we verified that the transient response is due to Au-mediated excitation of BuPTCD organic molecules by performing the same pump-probe reflectivity measurements on a glass substrate covered only with Au nanoislands. Using the same excitation pulse energy of 0.44 μ J, the measured reflectivity change of the Au nanoislands is zero. This indicates that the transient reflectivity response measured in Au-BuPTCD is entirely due to the organic molecular film.

The enhancement factor of the BuPTCD two-photon absorption due to the surface plasmon can be determined by comparing the reflectivity signals obtained from the BuPTCD film and the Au-BuPTCD film at the same excitation energy. However, at an excitation of 4.4 μ J we are unable to distinguish the BuPTCD reflectivity signal from the experimental noise level. We still can obtain a conservative estimate of the enhancement factor by comparing the upper bound of the BuPTCD noise (3%) to the measurements of the Au-BuPTCD reflectivity signal. Compared to the reflectivity change of 30% obtained for the Au-BuPTCD sample at an excitation of 0.44 μ J, the enhancement factor is at least 100. This is comparable to other enhancement factors observed for two-photon absorption processes reported for organic compounds [13, 16, 17].

5 Conclusion

We present pump-probe reflectivity spectra of BuPTCD thin films deposited on Au nanoislands. The observed changes in reflectivity are due to Au-mediated surface plasmon enhancement of two-photon absorption. The reflectivity spectrum reveals depletion of the molecule's ground state and excited state absorption. Our experimental results indicate that the Au nanoislands effectively enhance the two-photon absorption and that they can be used to functionalize organic molecules for device applications.

Acknowledgements Several people contributed to the work described in this paper. C.R.M. conceived of the basic idea for this work. M.K., C.R.M., and T.S. designed and carried out the experiments and analyzed the results. E.M. supervised the research and the development of the manuscript. We would like to acknowledge Dr. J. Duff of the Xerox Research Centre of Canada, who provided the BuPTCD samples. This work was carried out with financial support of the National Science Foundation under contract DMI-0334984 and the Army Research Office under contract W911NF-05-1-0471. T. Shih would like to acknowledge support from NSF Graduate Research Fellowship, and C.R. Mendonca acknowledges support from the FAPESP and CAPES (Brazil).

References

1. C.W. Tang, Appl. Phys. Lett. **48**, 183–185 (1986)
2. C.W. Tang, S.A. Vanslyke, Appl. Phys. Lett. **51**, 913–915 (1987)
3. J.H. Burroughes, D.D.C. Bradley, A.R. Brown, R.N. Marks, K. Mackay, R.H. Friend, P.L. Burns, A.B. Holmes, Nature **347**, 539–541 (1990)
4. E. Engel, M. Koschorreck, K. Leo, M. Hoffmann, Phys. Rev. Lett. **95** (2005)
5. C.J.L. Constantino, P.A. Antunes, C.B. Oliveira, M. Trsic, I. Caracelli, R.F. Aroca, Can. J. Anal. Sci. Spectrosc. **49**, 64–72 (2004)
6. A. Kam, R. Aroca, J. Duff, C.P. Tripp, Chem. Mater. **10**, 172–176 (1998)
7. A. Volpati, A.E. Job, R.F. Aroca, C.J.L. Constantino, J. Phys. Chem. B **112**, 3894–3902 (2008)
8. J. Danziger, J.P. Dodelet, P. Lee, K.W. Nebesny, N.R. Armstrong, Chem. Mater. **3**, 821–829 (1991)
9. J. Ivri, Z. Burshtein, E. Miron, R. Reisfeld, M. Eyal, IEEE J. Quantum Electron. **26**, 1516–1520 (1990)
10. L. De Boni, C.J.L. Constantino, L. Misoguti, R.F. Aroca, S.C. Zilio, C.R. Mendonca, Chem. Phys. Lett. **371**, 744–749 (2003)
11. S.L. Oliveira, D.S. Correa, L. Misoguti, C.J.L. Constantino, R.F. Aroca, S.C. Zilio, C.R. Mendonca, Adv. Mater. **17**, 1890 (2005)
12. D.S. Correa, S.L. Oliveira, L. Misoguti, S.C. Zilio, R.F. Aroca, C.J.L. Constantino, C.R. Mendonca, J. Phys. Chem. A **110**, 6433–6438 (2006)
13. I. Cohanoschi, S. Yao, K.D. Belfield, F.E. Hernandez, J. Appl. Phys. **101**, (2007)
14. R.F. Aroca, C.J.L. Constantino, J. Duff, Appl. Spectrosc. **54**, 1120–1125 (2000)
15. B. Tolaieb, C.J.L. Constantino, R.F. Aroca, Analyst **129**, 337–341 (2004)
16. H. Kano, S. Kawata, Opt. Lett. **21**, 1848–1850 (1996)
17. I. Cohanoschi, F.E. Hernandez, J. Phys. Chem. B **109**, 14506–14512 (2005)
18. P. Goulet, N. Pieczonka, R. Aroca, Can. J. Anal. Sci. Spectrosc. **48**, 146–152 (2003)
19. M. Kerker, D.S. Wang, H. Chew, Appl. Opt. **19**, 4159–4174 (1980)
20. S. Rodriguez-Llorente, R. Aroca, J. Duff, Spectrochim. Acta Part A, Mol. Biomol. Spectrosc. **55**, 969–978 (1999)
21. E. Engel, K. Schmidt, D. Beljonne, J.L. Bredas, J. Assa, H. Frob, K. Leo, M. Hoffmann, Phys. Rev. B **73**, (2006)
22. E. Engel, K. Leo, M. Hoffmann, Chem. Phys. **325**, 170–177 (2006)
23. R. Mercadante, M. Trsic, J. Duff, R. Aroca, Theochem. J. Mol. Struct. **394**, 215–226 (1997)
24. C.A.D. Roeser, A.M.T. Kim, J.P. Callan, L. Huang, E.N. Glezer, Y. Siegal, E. Mazur, Rev. Sci. Instrum. **74**, 3413–3422 (2003)
25. M.H. Hennessy, Z.G. Soos, R.A. Pascal, A. Girlando, Chem. Phys. **245**, 199–212 (1999)
26. V. Ramamurthy, K.S. Schanze, *Understanding and Manipulating Excited-State Processes* (Marcel Dekker, New York, 2001)
27. J.C. Tsang, J.E. Demuth, P.N. Sanda, J.R. Kirtley, Chem. Phys. Lett. **76**, 54–57 (1980)
28. M. Kandyla, T. Shih, E. Mazur, Phys. Rev. B **75**, (2007)
29. E. van Dijk, J. Hernando, J.J. Garcia-Lopez, M. Crego-Calama, D.N. Reinhoudt, L. Kuipers, M.F. Garcia-Parajo, N.F. van Hulst, Phys. Rev. Lett. **94**, 4 (2005)

Copyright of *Applied Physics A: Materials Science & Processing* is the property of Springer Science & Business Media B.V. and its content may not be copied or emailed to multiple sites or posted to a listserv without the copyright holder's express written permission. However, users may print, download, or email articles for individual use.

Copyright of *Applied Physics A: Materials Science & Processing* is the property of Springer Science & Business Media B.V. and its content may not be copied or emailed to multiple sites or posted to a listserv without the copyright holder's express written permission. However, users may print, download, or email articles for individual use.

Three-dimensional fabrication of optically active microstructures containing an electroluminescent polymer

C. R. Mendonca,^{1,2,a)} D. S. Correa,^{1,2} F. Marlow,³ T. Voss,^{2,4} P. Tayalia,² and E. Mazur²

¹*Instituto de Física de São Carlos, Universidade de São Paulo, Caixa Postal 369, 13560-970 São Carlos, SP, Brazil*

²*Department of Physics and Harvard School of Engineering and Applied Sciences, Harvard University,*

9 Oxford Street, Cambridge, Massachusetts 02138, USA

³*Max-Planck-Institut für Kohlenforschung, Mülheim an der Ruhr, D-45470, Germany*

⁴*Institut für Festkörperphysik, Universität Bremen, P.O. Box 330440, 28334 Bremen, Germany*

(Received 18 April 2009; accepted 29 August 2009; published online 18 September 2009)

Microfabrication via two-photon absorption polymerization is a technique to design complex microstructures in a simple and fast way. The applications of such structures range from mechanics to photonics to biology, depending on the dopant material and its specific properties. In this paper, we use two-photon absorption polymerization to fabricate optically active microstructures containing the conductive and luminescent polymer poly(2-methoxy-5-(2'-ethylhexyloxy)-1,4-phenylenevinylene) (MEH-PPV). We verify that MEH-PPV retains its optical activity and is distributed throughout the microstructure after fabrication. The microstructures retain the emission characteristics of MEH-PPV and allow waveguiding of locally excited fluorescence when fabricated on top of low refractive index substrates. © 2009 American Institute of Physics.

[doi:10.1063/1.3232207]

Since its introduction in 1997,¹ two-photon polymerization has proven to be a suitable technique to fabricate three-dimensional microstructures, with applications in optical circuitry,² optical data storage,³ three-dimensional micromechanical actuators,^{4–6} birefringent microstructures,⁷ photonic crystals,^{3,8} and biomedical devices.^{9–12} Two-photon polymerization enables the fabrication of three-dimensional microstructures because the polymerization is restricted to the focal volume of the laser beam, where the photon flux density is high enough that two photons can be simultaneously absorbed in a single event.¹³ By scanning the focus of the laser beam in three dimensions, complex microstructures can be fabricated.^{13,14} While the majority of studies reported to date explore undoped microstructures, which are passive and therefore of limited use in technological applications, more recently, some reports deal with doped microstructures, which possess enhanced optical and biological properties.^{7,11,15–21}

In this paper, we report on two-photon polymerization of microstructures containing the polymer poly(2-methoxy - 5-(2' - ethylhexyloxy) - 1,4-phenylenevinylene) (MEH-PPV).^{22–24} We use a guest-host strategy in which the host consists of two triacrylate monomers. The guest material is MEH-PPV, a polymer known for its conductivity,²⁴ electroluminescence,^{22,23} and nonlinear optical properties.^{25–28} The microstructures are freestanding and preserve the luminescence properties of MEH-PPV. Our results show that MEH-PPV is distributed throughout the microstructure and not just at the surface. We also demonstrate waveguiding of MEH-PPV fluorescence in 100 μm long microstructures fabricated on mesoporous silica substrates. The microstructures hold promise for photonics applications,

such as microlight emitting diodes (microLEDs) and micro-waveguides.

We fabricate microstructures by two-photon absorption polymerization of an acrylate-based resin containing MEH-PPV. The resin consists of a mixture of two triacrylate monomers: tris(2-hydroxyethyl) isocyanurate triacrylate (30% by weight), which increases the hardness of the microstructure, and ethoxylated(6) trimethylolpropane triacrylate (70% by weight), which reduces shrinkage upon polymerization. We initially prepare an ethanol solution containing these two triacrylate monomers, to which we add MEH-PPV (up to 1% by weight). We stir this solution for 1 h to fully mix the components. Ethanol is then eliminated by evaporation at room temperature for 24 h, yielding a viscous liquid. Finally, we add to this liquid the polymerization photoinitiator ethyl-2,4,6-trimethylbenzoylphenylphosphine, commercially known as Lucirin T-POL^{29,30} (3% by weight), mixing it for 1 h prior to use.

To increase adhesion of the microstructure to the glass substrate, we treat the surface of a microscope slide with (3-acryloxypropyl)trimethoxysilane. Then we place a drop of the resin inside a spacer located on the surface-treated microscope slide and place a cover slip on top of the spacer. The resin is polymerized using 130 fs pulses at 800 nm from a Ti:sapphire laser oscillator operating at 80 MHz. For fabricating the microstructures, we use an average power of 40 mW, measured before the 0.65 numerical aperture objective, which focuses the laser beam into the sample, yielding a laser fluence of nearly 30 mJ/cm². A motorized stage moves the sample in the axial z direction and a pair of galvanometer mirrors scans the laser across the resin in the x - y direction. After fabricating the desired microstructure, we place the sample in ethanol to wash away any unpolymerized resin. In addition, we fabricate waveguides using the same approach described before. However, in this case, we use mesoporous silica films as substrates, which have a low refractive index

^{a)}Author to whom correspondence should be addressed. Electronic mail: crmendon@ifsc.usp.br.

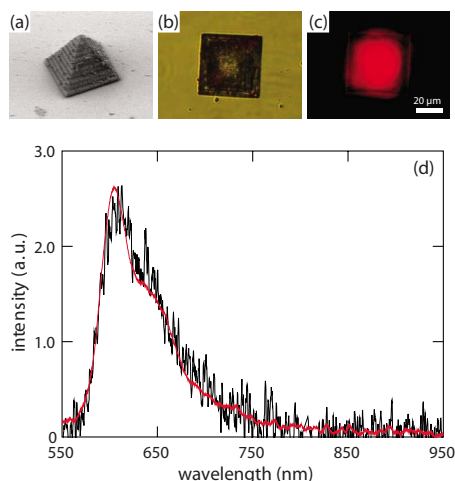


FIG. 1. (Color online) (a) Scanning electron microscopy of a pyramidal microstructure containing MEH-PPV. Fluorescence microscopy image of the pyramid (top view) with laser excitation at 532 nm (b) off and (c) on. (d) Emission spectrum of the microstructure (black line) and of a film with the same composition (red line).

($n=1.185$) throughout the visible spectrum.³¹

We obtain the fluorescence spectrum and fluorescence microscopy images of the microstructures by exciting them with a neodymium doped yttrium aluminum garnet cw laser operating at 532 nm and an average power of 1 mW. To obtain the fluorescence microscopy images, we use a color filter in front of the camera to block the excitation light at 532 nm. We collect the fluorescence spectrum of microstructures through an exit port of the microscope using a portable spectrometer.

The confocal microscopy images of the microstructure containing MEH-PPV are obtained using 540 nm excitation light ($40\times$ objective). We collect the emission at 570 nm from x - y planes of the microstructure separated in the z direction by 16 μm .

Figure 1(a) shows scanning electron microscope image of a 40 μm square-base pyramid containing 1% MEH-PPV fabricated by two-photon polymerization. Figure 1(b) shows a top view bright-field image of the microstructure. Figure 1(c) shows the fluorescence image of the same microstructure. The fluorescence spectra of the microstructure and of an approximately 100 μm thick film with the same composition as the microstructure are displayed in Fig. 1(d). The spectra have the same shape, confirming that the fluorescence observed in Fig. 1(c) arises from the MEH-PPV contained in the microstructure. The noise observed in the microstructure spectrum is due to the low intensity of the fluorescence signal because the microstructure has dimensions of only a few micrometers. We also fabricated microstructures down to 4 μm long side, which presents the same features of the fluorescence spectrum showed in Fig. 1(d). We observed that the fluorescence intensity decreases linearly with the MEH-PPV content as the microstructure size diminishes. For microstructures of a given size, we measured a maximum variation of approximately 20% in the fluorescence intensity.

To verify that the MEH-PPV is distributed throughout the microstructure, we obtained fluorescence confocal microscopy images of a pyramidal microstructure with a squared base of $120\times 120\ \mu\text{m}^2$ at different z levels (Fig. 2).

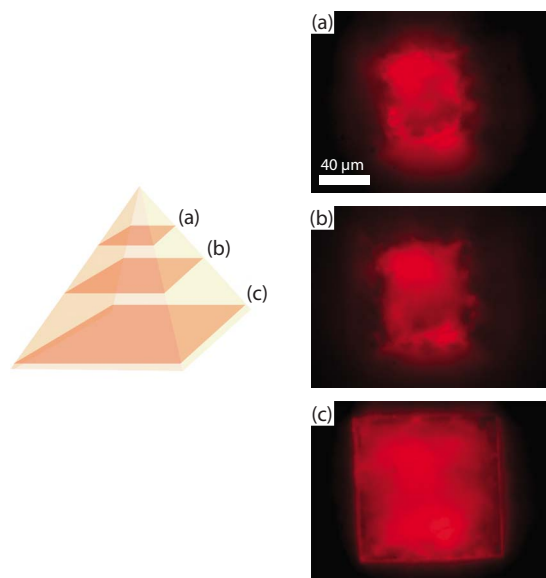


FIG. 2. (Color online) Fluorescent confocal microscopy images of planes separated by 16 μm in a pyramidal microstructure (squared base of $120\times 120\ \mu\text{m}^2$).

The sequence of fluorescence images represent layers of the pyramidal microstructure separated by 16 μm each.

Figure 3(a) shows a 100 μm long waveguide, containing MEH-PPV, illuminated in its central region by a focused laser at 532 nm (top view). The MEH-PPV fluorescence is guided through the microstructure and scatters at both microstructure ends. Because of surface roughness, some light scattering occurs along the waveguide. Figure 3(b) shows no waveguiding of a microstructure fabricated on top of a conventional glass slide (top view). In the left hand side of Fig. 3, we display a schematic (side view) of the microstructure excitation and the corresponding waveguiding.

The fabrication method used in this work involves absorption of two photons, localizing polymerization to the focal region and allowing the fabrication of three-dimensional microstructures. The MEH-PPV containing microstructure in Fig. 1(a) exhibits excellent integrity and good definition, indicating that the presence of MEH-PPV does not affect the fabrication process, provided we use laser power below 40 mW. Furthermore, MEH-PPV is retained in the microstructure, as demonstrated by the characteristic fluorescent emis-

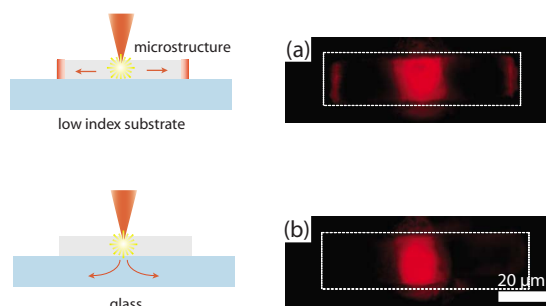


FIG. 3. (Color online) Fluorescence optical microscopy image (top view) of a MEH-PPV-containing microstructure fabricated on a mesoporous silica substrate (a) and on a conventional glass substrate (b). In (a), the light is guided through the microstructure ends when it is excited at its center. For the microstructure on glass substrate no fluorescence waveguiding is observed (b). In the left hand side of the figure we display a schematic (side view) of the microstructure excitation and the corresponding waveguiding.

sion observed in Fig. 1(c) and its corresponding spectrum [Fig. 1(d)]. Such a result implies that the MEH-PPV retained in the microstructure is not degraded during the microfabrication, which is desirable for application in optical devices. For laser powers above 40 mW, we observe generation of bubbles during microfabrication, which ruins the quality of the final structure.

The fluorescence confocal microscopy images in Fig. 2 show that MEH-PPV is distributed throughout the microstructure and not only at its surface. The microstructures preserve their luminescent properties, although the images at each z level reveal nonuniform distributions at different planes of the microstructure. This nonuniformity could be caused by the moderate solubility of MEH-PPV in the acrylic based-resin. To improve the solubility and distribution of MEH-PPV in the acrylic resin, one could reduce the amount of dopant, although this would decrease the fluorescence intensity of the microstructure.

When the microstructures are fabricated on top of low-refractive index substrates, we observe waveguiding of MEH-PPV fluorescence [Fig. 3(a)]. The low refractive index,³¹ the homogeneity, and the flatness of the mesoporous silica minimize the waveguiding losses in the acrylic-based waveguides by preventing parasitic scattering and coupling into the substrate. On the other hand, we do not see waveguiding in Fig. 3(b) because this microstructure lies on a conventional glass substrate, leading to light coupling into the substrate. The light scattering observed along the waveguides arises from surface roughness and inhomogeneity of the microstructure, which can be decreased by improving the stages and objectives in the microfabrication setup. Ultimately, microstructures fabricated on top of mesoporous silica substrate could be used for photonics applications, such as microLEDs and microwaveguides.

In conclusion, we present an approach for fabricating three-dimensional microstructures containing the luminescent polymer MEH-PPV using two-photon absorption polymerization. The microstructures present good definition and structural integrity, which is required for photonics devices. Fluorescence microscopy images show that MEH-PPV is retained in the microstructure after the fabrication and that its optical properties are preserved. Fluorescence confocal microscopy images show that the MEH-PPV is distributed not only at the surface, but throughout the bulk of the microstructure, which enhances the luminescence properties of the microstructures. In addition, we demonstrate waveguiding of the MEH-PPV emission in 100 μm long microstructures fabricated on top of porous silica substrates, revealing the feasibility of fabricating photonics devices such as microLEDs and microwaveguides.

The research described in this paper was supported by National Science Foundation under Grant No. DMI 0334984, the Army Research Office under Grant No. ARO W911NF-05-1-0471. C.R.M. acknowledges support from FAPESP and CAPES from Brazil during his stay at Harvard University. D. S.C. also acknowledges FAPESP. T.V. acknowledges funding by the DFG from Germany through the Grant No. N.V. 1265/3. The authors also would like to acknowledge the use of facilities of the Center for Nanoscale Systems, which is supported by the National Science Foundation's National

Nanotechnology Infrastructure Network. The authors would like to acknowledge Jason Dowd and Jessica Watkins for providing feedback on the manuscript.

- ¹S. Maruo, O. Nakamura, and S. Kawata, *Opt. Lett.* **22**, 132 (1997).
- ²M. P. Joshi, H. E. Pudavar, J. Swiatkiewicz, P. N. Prasad, and B. A. Reianhardt, *Appl. Phys. Lett.* **74**, 170 (1999).
- ³B. H. Cumpston, S. P. Ananthavel, S. Barlow, D. L. Dyer, J. E. Ehrlich, L. L. Erskine, A. A. Heikal, S. M. Kuebler, I. Y. S. Lee, D. McCord-Maughon, J. Q. Qin, H. Rockel, M. Rumi, X. L. Wu, S. R. Marder, and J. W. Perry, *Nature (London)* **398**, 51 (1999).
- ⁴P. Galajda and P. Ormos, *Appl. Phys. Lett.* **78**, 249 (2001).
- ⁵T. Watanabe, M. Akiyama, K. Totani, S. M. Kuebler, F. Stellacci, W. Wenseleers, K. Braun, S. R. Marder, and J. W. Perry, *Adv. Funct. Mater.* **12**, 611 (2002).
- ⁶Z. Bayindir, Y. Sun, M. J. Naughton, C. N. LaFratta, T. Baldacchini, J. T. Fourkas, J. Stewart, B. E. A. Saleh, and M. C. Teich, *Appl. Phys. Lett.* **86**, 064105 (2005).
- ⁷C. R. Mendonca, T. Baldacchini, P. Tayalia, and E. Mazur, *J. Appl. Phys.* **102**, 013109 (2007).
- ⁸J. Serbin, A. Ovsianikov, and B. Chichkov, *Opt. Express* **12**, 5221 (2004).
- ⁹A. Ovsianikov, B. Chichkov, O. Adunka, H. Pillsbury, A. Doraiswamy, and R. J. Narayan, *Appl. Surf. Sci.* **253**, 6603 (2007).
- ¹⁰R. Liska, M. Schuster, R. Infuhr, C. Turecek, C. Fritscher, B. Seidl, V. Schmidt, L. Kuna, A. Haase, F. Varga, H. Lichtenegger, and J. Stampfl, *J. Coat. Technol.* **4**, 505 (2007).
- ¹¹D. S. Correa, P. Tayalia, G. Cosendey, D. S. Dos Santos, Jr., R. F. Aroca, E. Mazur, and C. R. Mendonca, *J. Nanosci. Nanotechnol.* **9**, 5845 (2009).
- ¹²P. Tayalia, C. R. Mendonca, T. Baldacchini, D. J. Mooney, and E. Mazur, *Adv. Mater.* **20**, 4494 (2008).
- ¹³H. B. Sun and S. Kawata, in *NMR—3D Analysis—Photopolymerization* (Springer, Berlin, 2004), Vol. 170, pp. 169–273.
- ¹⁴S. Kawata, H. B. Sun, T. Tanaka, and K. Takada, *Nature (London)* **412**, 697 (2001).
- ¹⁵T. S. Drakakis, G. Papadakis, K. Sambani, G. Filippidis, S. Georgiou, E. Gizeli, C. Fotakis, and M. Farsari, *Appl. Phys. Lett.* **89**, 144108 (2006).
- ¹⁶H. B. Sun, T. Tanaka, K. Takada, and S. Kawata, *Appl. Phys. Lett.* **79**, 1411 (2001).
- ¹⁷C. N. LaFratta, J. T. Fourkas, T. Baldacchini, and R. A. Farrer, *Angew. Chem., Int. Ed.* **46**, 6238 (2007).
- ¹⁸A. Ovsianikov, J. Viertl, B. Chichkov, M. Oubaha, B. MacCraith, L. Sakellari, A. Giakoumaki, D. Gray, M. Vamvakaki, M. Farsari, and C. Fotakis, *ACS Nano* **2**, 2257 (2008).
- ¹⁹M. Farsari, A. Ovsianikov, M. Vamvakaki, I. Sakellari, D. Gray, B. N. Chichkov, and C. Fotakis, *Appl. Phys. A: Mater. Sci. Process.* **93**, 11 (2008).
- ²⁰N. Takeyasu, T. Tanaka, and S. Kawata, *Appl. Phys. A: Mater. Sci. Process.* **90**, 205 (2008).
- ²¹Z. B. Sun, X. Z. Dong, S. Nakanishi, W. Q. Chen, X. M. Duan, and S. Kawata, *Appl. Phys. A: Mater. Sci. Process.* **86**, 427 (2007).
- ²²I. D. Parker, *J. Appl. Phys.* **75**, 1656 (1994).
- ²³T. Q. Nguyen, I. B. Martini, J. Liu, and B. J. Schwartz, *J. Phys. Chem. B* **104**, 237 (2000).
- ²⁴G. Yu, J. Gao, J. C. Hummelen, F. Wudl, and A. J. Heeger, *Science* **270**, 1789 (1995).
- ²⁵S. L. Oliveira, D. S. Correa, L. De Boni, L. Misoguti, S. C. Zilio, and C. R. Mendonca, *Appl. Phys. Lett.* **88**, 021911 (2006).
- ²⁶L. De Boni, A. A. Andrade, D. S. Correa, D. T. Balogh, S. C. Zilio, L. Misoguti, and C. R. Mendonca, *J. Phys. Chem. B* **108**, 5221 (2004).
- ²⁷S.-J. Chung, G. S. Maciel, H. E. Pudavar, T.-C. Lin, G. S. He, J. Swiatkiewicz, P. N. Prasad, D. W. Lee, J.-I. Lin, and M. Menard, *J. Phys. Chem. A* **106**, 7512 (2002).
- ²⁸D. S. Correa, L. De Boni, D. T. Balogh, and C. R. Mendonca, *Adv. Mater.* **19**, 2653 (2007).
- ²⁹C. R. Mendonca, D. S. Correa, T. Baldacchini, P. Tayalia, and E. Mazur, *Appl. Phys. A: Mater. Sci. Process.* **90**, 633 (2008).
- ³⁰T. Baldacchini, C. N. LaFratta, R. A. Farrer, M. C. Teich, B. E. A. Saleh, M. J. Naughton, and J. T. Fourkas, *J. Appl. Phys.* **95**, 6072 (2004).
- ³¹D. Konjhdzic, H. Bretinger, U. Wilczok, A. Dreier, A. Ladenburger, M. Schmidt, M. Eich, and F. Marlow, *Appl. Phys. A: Mater. Sci. Process.* **81**, 425 (2005).

Two-Photon Polymerization for Fabricating Structures Containing the Biopolymer Chitosan

D. S. Correa^{1,2}, P. Tayalia², G. Cosendey², D. S. dos Santos, Jr.³,
R. F. Aroca³, E. Mazur², and C. R. Mendonca^{1,2,*}

¹*Instituto de Física de São Carlos, Universidade de São Paulo, Caixa Postal 369, 13560-970 São Carlos, SP, Brazil*

²*Department of Physics and School of Engineering and Applied Sciences, Harvard University,
Cambridge, Massachusetts 02138, USA*

³*Department of Chemistry and Biochemistry, University of Windsor, Windsor, ON, N9B3 P4 Canada*

Two-photon polymerization is a powerful tool for fabricating three-dimensional micro/nano structures for applications ranging from nanophotonics to biology. To tailor such structure for specific purposes it is often important to dope them. In this paper we report on the fabrication of structures, with nanometric surface features (resolution of approximately 700 nm), using two-photon polymerization of an acrylic resin doped with the biocompatible polymer chitosan using a guest-host scheme. The fluorescence background in the Raman spectrum indicates the presence of chitosan throughout the structure. Mechanical characterization reveals that chitosan does not affect the mechanical properties of the host acrylic resin and, consequently, the structures exhibit excellent integrity. The approach presented in this work can be used in the fabrication of micro- and nanostructures containing biopolymers for biomedical applications.

Keywords: Polymers, Biomaterials, Raman Spectroscopy and Scattering, Microstructure.

1. INTRODUCTION

Two-photon polymerization is a powerful tool for fabricating three-dimensional structures with dimensions ranging from micro- to nanometers for diverse applications, such as optical circuitry,¹ optical data storage,² three-dimensional mechanical actuators,^{3–5} birefringent structures,⁶ photonic crystals^{2,7} and bone replacement.^{8–9} The nonlinear nature of multiphoton absorption confines polymerization to the focal volume of the laser, allowing fabrication of structures by scanning a focused laser beam through the resin.^{10–12} Due to the optical nonlinearity and the threshold energy required for the photo-polymerization, multiphoton polymerization techniques allow the achievement of resolution better than the laser beam diffraction limit. For instance, two-photon polymerization with features smaller than 100 nm have been reported recently.^{13–16} To tailor the property of resins for specific applications it is important to identify new dopants that can be used in two-photon polymerization. To date limited work has been reported on the fabrication of structures using two-photon polymerization of doped resins.^{6, 17–19}

In this paper, we report on two-photon fabrication of structures containing the biopolymer chitosan, with resolution of approximately 700 nm. We use a guest-host strategy in which the host consists of two triacrylate monomers, and the guest material is chitosan. Chitosan [(1→4)-2 amino-2-deoxy-β-D-glucan] is a linear cationic polysaccharide obtained by deacetylation of chitin [(1→4)-2 acetamide-2-deoxy-β-D-glucan], a structural polysaccharide normally encountered in crustaceans.²⁰ It is a biodegradable and biocompatible polymer,^{21,22} which has been used for applications in blood coagulation,^{23–25} taste sensors,^{26,27} soft tissue and bone regeneration,²⁸ antibacterial action²¹ and conductive membranes.²⁹ Chitosan has also been used in producing nanostructured films^{30,31} and nanoparticles for applications in drug delivery.^{32–35} The structures we fabricated contain chitosan distributed throughout the bulk. In addition, we show that chitosan does not impair the mechanical properties of the polymer. Therefore, the fabrication process presented here is promising for fabricating tailor-made structures containing chitosan with nanometric features for biomedical applications.

2. EXPERIMENTAL DETAILS

The resin we used consists of a mixture of tris(2-hydroxyethyl)isocyanurate triacrylate, which gives

*Author to whom correspondence should be addressed.

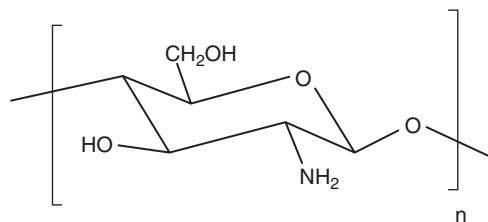


Fig. 1. Chemical structure of chitosan.

hardness to the structure, and ethoxylated(6) trimethylolpropane triacrylate, which reduces shrinkage upon polymerization³⁶ and the photoinitiator Lucirin TPO-L. We demonstrated earlier that Lucirin TPO-L is suitable for two-photon absorption polymerization, despite its low two-photon absorption cross-section.³⁷

Chitosan, whose chemical structure is shown in Figure 1, is extracted from gray shrimps using a standard approach described in the literature.³⁸ The extracted chitosan is purified by dissolution in acetic acid, precipitation in 0.1-M NaOH, and filtration using a 450-nm membrane. The purified chitosan sample has a molecular weight of 450 kg/mol and a degree of deacetylation of 72, determined by H-NMR according to Lavertu Method.³⁹ The sample is dissolved in a solution of acetic acid in ethanol (7% by volume), and mixed for 30 min. with the triacrylate resins. Ethanol is eliminated by evaporation at room temperature for 24 h, yielding a viscous liquid containing the chitosan. To this liquid, we add the photoinitiator (1% by weight) and stir for 1 h prior to use. We prepared solutions containing from 1% up to 10% of chitosan by weight. We were able to fabricate microstructures within this range of chitosan content, however we present the results only of the solution containing 10% of chitosan by weight.

To fabricate the structures, we place a drop of the viscous liquid between spacers located on top of a microscope slide, which is then covered by a cover slip. The surface of the microscope slide is treated with (3-acryloxypropyl)trimethoxysilane to increase adhesion of the polymerized structure to the glass substrate. The resin is polymerized using 130-fs pulses at 800 nm from a Ti:sapphire laser oscillator operating at 80 MHz. The average power of the laser is 60 mW, measured before the 0.65-NA objective that focuses the laser beam into the sample. The sample is positioned in the axial z direction using a motorized stage, and the laser is scanned in the x - y direction by a pair of galvo mirrors. After the laser exposure, the sample is immersed in ethanol to wash away any unsolidified resin.

We analyzed the structures using a Raman microscope. Typically, we used 200 μ W of the 514.5-nm argon ion laser line at the sample for Raman scattering, mapping and global imaging. For the 785- and 632.8-nm laser lines, the power at the sample was 25 μ W. All measurements were

made in a backscattering geometry, using a 50 \times microscope objective with a numerical aperture value of 0.75, providing scattering areas of about 1 μ m². Single point spectra were recorded with 4 cm⁻¹ resolution, while 2D mapping results were collected through the rastering of a computer-controlled 3-axis encoded motorized stage, with a step of 1 μ m. To test the structural properties of the material, we used UV-lamp to polymerize discs of 20-mm diameter and 1-mm height from the same resin. To evaluate the hardness of the material, we used the Shore-D hardness test, which is based on the penetration of an indenter into the surface of the material (ASTM D2240-00 – “Standard Test Method for Rubber Property – Durometer Hardness”).

3. RESULTS

Figure 2 shows optical microscopy images of the top view of three-dimensional structures of tri-acrylate resins containing up to 10% of chitosan by weight fabricated by two-photon absorption polymerization. The cubic structures range in dimension from 40 μ m (Fig. 2(a)) to 6 μ m (Fig. 2(c)), with a resolution of approximately 700 nm.

The structures in Figure 2 were fabricated with an average power of 20 mW, measured after the 0.65-NA objective. At an average power below 10 mW two-photon absorption polymerization does not occur. At average powers above 40 mW we observe generation of bubbles during the polymerization, which ruins the quality of the final structure.

Figure 3 shows scanning electron micrographs of three-dimensional acrylate resin structures containing chitosan and fabricated using an average power of 20 mW. The stripes and pattern on the surface of the structures were produced during the fabrication, displaying that features on the scale of nanometers can be made. The structures have excellent definition and physical integrity, demonstrating that the method presented here is suitable for fabricating biopolymer-containing micro/nano structures. Although the structures presented here are simple, structures of any shape or pattern can be produced with this technique.

To verify if the acrylic resins present Raman signals distinct from those of chitosan, we measured the Raman spectrum of 100- μ m thick acrylate films of the same compositions as the microstructures (with and without chitosan), and of a pure chitosan film. Figure 4 shows that the Raman spectra of the resin sample without chitosan (blue line) and with chitosan (dark gray) are very similar. The spectrum of chitosan-containing resin differs from that of the pure resin by a monotonic rise of the background towards higher wavenumbers. This monotonically rising background can be attributed to fluorescence from chitosan and is also visible in the spectrum of neat chitosan (Fig. 2, gray line). The absence of any lines in the neat chitosan spectrum can be explained by the fact that chitosan is a poor scatterer with a very low Raman cross section.

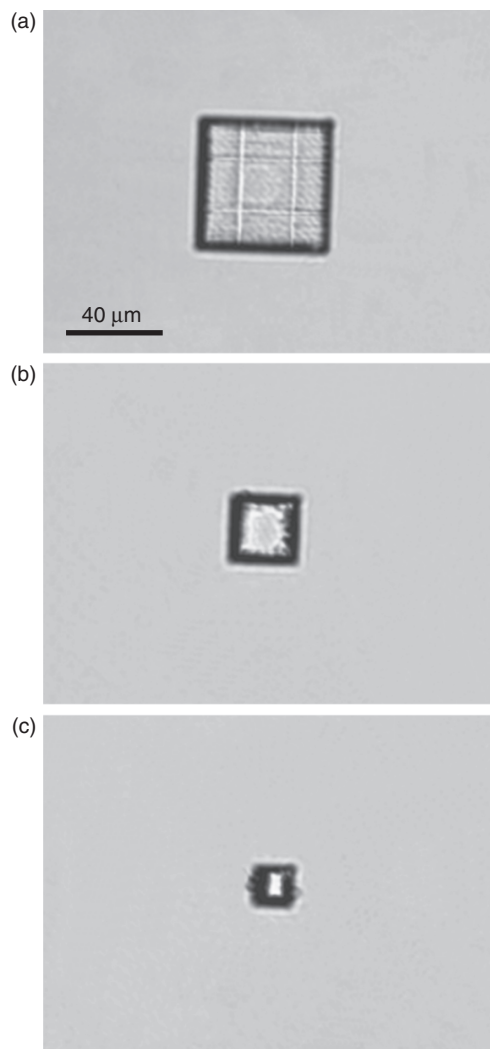


Fig. 2. Optical microscopy images of cubic microstructures of different sizes fabricated via two-photon absorption polymerization. (a), (b), and (c) hold the same scale bar.

The fluorescence background indicates that chitosan is distributed throughout the structure. The Raman scattering spectrum obtained from a cubic structure without chitosan shown in Figure 5(a) exhibits vibrational lines at 1637 cm^{-1} and at 1736 cm^{-1} . The left two images in the inset are Raman maps of the structure obtained from the intensity of the vibrational modes at 1637 cm^{-1} and 1736 cm^{-1} . The square shape of the structures in the Raman map agrees with the shape observed in the scanning electron micrographs in Figure 3(a). The right-most image was created from the intensity recorded at 1858 cm^{-1} where there is no characteristic Raman peak of the resin. Indeed no structure is seen at this wavenumber.

Figure 5(b) shows the Raman spectrum of a fabricated structure containing chitosan, using the same excitation wavelength. As we concluded before, Raman measurements do not reveal any distinctive chitosan peaks. However, the spectrum in Figure 5(b) does reveal the

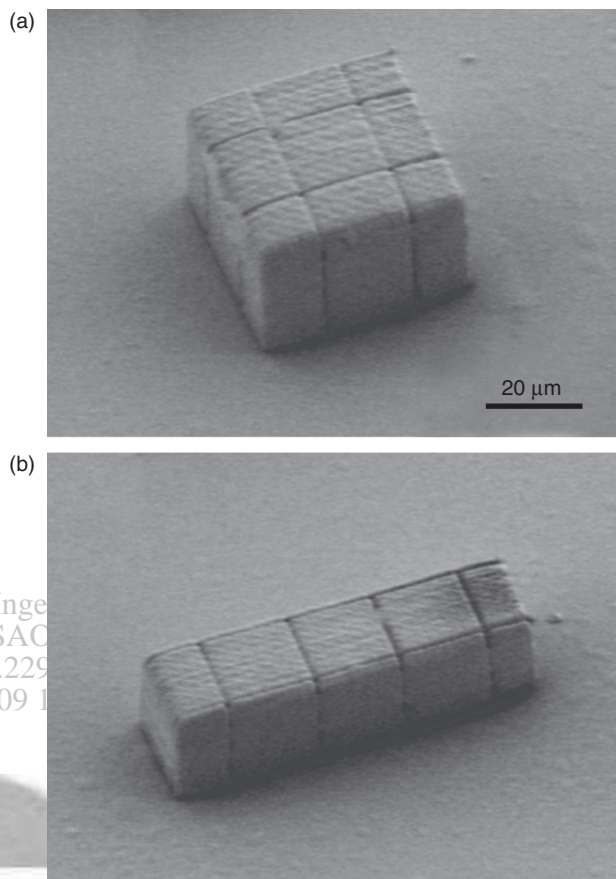


Fig. 3. Scanning electron micrographs of microstructures containing chitosan fabricated by two-photon absorption polymerization. (a) and (b) hold the same scale bar.

monotonic rise in background characteristic of chitosan fluorescence, indicating that the structures produced contain chitosan.

To determine the influence of chitosan on the mechanical properties of the acrylic resin, we measured the

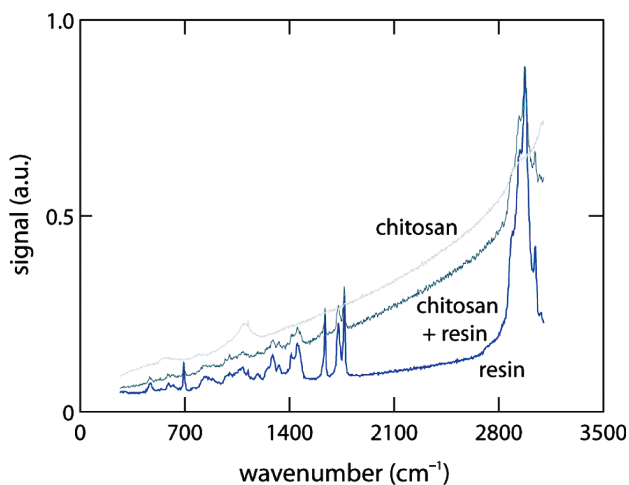


Fig. 4. Raman scattering spectrum of resin films with (dark gray) and without chitosan (blue), and for pure chitosan (light gray).

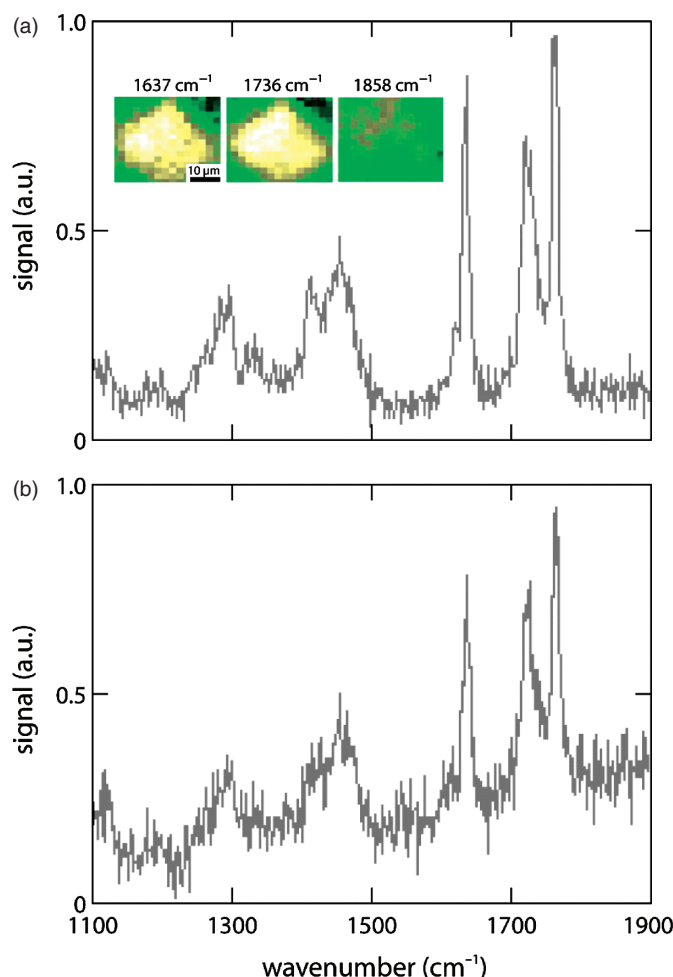


Fig. 5. Raman spectra of a microstructure (a) without and (b) with chitosan. The inset shows images built from the Raman scattering signal at 1637 cm^{-1} , 1736 cm^{-1} and 1858 cm^{-1} , using excitation at 514 nm .

hardness of specimens fabricated with acrylic resin and chitosan. The results of the hardness test are displayed in Table I. We observe that both the mixture of acrylic resins with (10% in weight) and without chitosan have an average hardness of 80 ± 1 on the Shore D scale. This value is higher than low-density and high-density polyethylene and comparable to polypropylene.⁴⁰

4. DISCUSSION

Because the fabrication method used here involves simultaneous absorption of two photons, the polymerization is

Table I. Shore D scale hardness comparison of the acrylic resin with and without chitosan, and some other polymers.

Material	Hardness (shore D scale)
Resin	80 ± 1
Resin + chitosan	80 ± 1
Low-density polyethylene	45 ± 5
High-density polyethylene	65 ± 5
Polypropylene	80 ± 5

highly localized and occurs only in the focal region of the laser beam, allowing the fabrication of three-dimensional microstructures. The absorption creates free radicals of the photoinitiator Lucirin TPO-L which react with unsaturated monomers of the acrylic resin, creating an active site that triggers the crosslinking of acrylic monomers. Multiphoton polymerization techniques offer real three-dimensional fabrication, at resolutions lower than 100 nm . Such resolution on the nanometric scale can only be achieved owing to the nonlinear nature of the process, which narrows the interaction region below the diffraction limit of the excitation wavelength, and to the careful control of the laser intensity close to the threshold energy of photopolymerization. Ideally the chitosan should be retained within the structure without forming any kind of crosslinking, which would alter its desirable chemical properties for biological application.

The chitosan-containing structures in Figure 3 exhibit excellent integrity and good definition, indicating that the presence of chitosan does not affect the fabrication process and confirming the feasibility of fabricating three-dimensional chitosan-containing structures by two-photon absorption polymerization. In addition, Figure 3 shows that nanometric patterns can be produced on the structure surface, allowing a new approach of manipulating chitosan compounds on a nanometric scale, aiming at biological applications.

The Raman spectrum of films or fabricated structures made of the chitosan-containing acrylate resin differs from that of films or structures made without chitosan only in a fluorescence background that can be attributed to chitosan (Figs. 4 and 5). Because the addition of chitosan does not affect the vibrational Raman spectrum of the resin, we infer that crosslinking or other chemical interaction between the acrylic resin and the chitosan is negligible. Such mixing without chemical interaction is desirable for biomedical applications, because it implies that the acrylic resins retain chitosan without altering any of its biological or chemical properties.

The hardness is inversely proportional to the indentation depth, and depends on the elastic modulus and viscoelasticity of the polymer. Although the data presented in Table I give an idea of the material's penetration resistance, they cannot be directly correlated with the fundamental properties of the material (e.g., elastic modulus). Our results indicate that chitosan does not reduce the hardness of the acrylic resins. Therefore, three-dimensional structures fabricated using two-photon polymerization containing chitosan can be used in biomedical applications.

5. CONCLUSION

We present an approach for fabricating three-dimensional structures containing the biocompatible polymer chitosan with nanometric features. The two-photon polymerized

structures present good definition and structural integrity. Raman measurements show that chitosan is incorporated in the structure and is distributed throughout its bulk. The spectra also show that chitosan does not react chemically with the acrylic resin, which is a required condition for biomedical applications, where the acrylic resin must work as a substrate for chitosan without changing its chemical properties. Finally, hardness measurements show that chitosan does not impair the mechanical properties of the resins. Therefore, two-photon polymerization can be used to fabricate three-dimensional structures containing chitosan, with nanometric features or even on the nanometric scale, which may then be applied in tissue engineering, bone reconstruction and drug delivery.

Acknowledgments: The research described in this paper was supported by National Science Foundation under contract DMI 0334984, the Army Research Office under contract ARO W911NF-05-1-0471. C. R. Mendonça and D. S. Correa acknowledge support from Fundação de Amparo à Pesquisa do Estado de São Paulo (FAPESP). Cleber Mendonça also acknowledges Coordenação de Aperfeiçoamento de Pessoal de Nível Superior (CAPES) from Brazil. The authors would also like to acknowledge the use of facilities of the Center for Nanoscale Systems, which is supported by the National Science Foundation's National Nanotechnology Infrastructure Network. We also would like to thank Dr. Rosa Ana Campos-Araiz (University of Valladolid) for valuable help with the micro-Raman measurements.

References and Notes

1. K. D. Belfield, Y. Liu, R. A. Negres, M. Fan, G. Pan, D. J. Hagan, and F. E. Hernandez, *Chemistry of Materials* 14, 3663 (2002).
2. J. Scrimgeour, D. N. Sharp, C. F. Blandford, O. M. Roche, R. G. Denning, and A. J. Turberfield, *Adv. Mater.* 18, 1557 (2006).
3. L. H. Nguyen, M. Straub, and M. Gu, *Advanced Functional Materials* 15, 209 (2005).
4. T. Watanabe, M. Akiyama, K. Totani, S. M. Kuebler, F. Stellacci, W. Wenseleers, K. Braun, S. R. Marder, and J. W. Perry, *Advanced Functional Materials* 12, 611 (2002).
5. Z. Bayindir, Y. Sun, M. J. Naughton, C. N. LaFratta, T. Baldacchini, J. T. Fourkas, J. Stewart, B. E. A. Saleh, and M. C. Teich, *Appl. Phys. Lett.* 86, 064105 (2005).
6. C. R. Mendonça, T. Baldacchini, P. Tayalia, and E. Mazur, *J. Appl. Phys.* 102, 013109 (2007).
7. J. Serbin, A. Ovsianikov, and B. Chichkov, *Optics Express* 12, 5221 (2004).
8. A. Ovsianikov, B. Chichkov, O. Adunka, H. Pillsbury, A. Doraiswamy, and R. J. Narayan, *Appl. Surf. Sci.* 253, 6603 (2007).
9. R. Liska, M. Schuster, R. Infuhr, C. Turecek, C. Fritscher, B. Seidl, V. Schmidt, L. Kuna, A. Haase, F. Varga, H. Lichtenegger, and J. Stampfl, *Journal of Coatings Technology and Research* 4, 505 (2007).
10. H. B. Sun and S. Kawata, NMR – 3D Analysis – Photopolymerization, *Advances in Polymer*, Springer-Verlag, Berlin (2004), Vol. 170, p. 169.
11. S. Kawata, H. B. Sun, T. Tanaka, and K. Takada, *Nature* 412, 697 (2001).
12. J. T. Fourkas and S. Maruo, *Laser & Photonics Reviews* 2, 100 (2008).
13. W. Haske, V. W. Chen, J. M. Hales, W. T. Dong, S. Barlow, S. R. Marder, and J. W. Perry, *Optics Express* 15, 3426 (2007).
14. D. F. Tan, Y. Li, F. J. Qi, H. Yang, Q. H. Gong, X. Z. Dong, and X. M. Duan, *Appl. Phys. Lett.* 90, 071106 (2007).
15. J. F. Xing, X. Z. Dong, W. Q. Chen, X. M. Duan, N. Takeyasu, T. Tanaka, and S. Kawata, *Appl. Phys. Lett.* 90, 131106 (2007).
16. S. Juodkazis, V. Mizeikis, K. K. Seet, M. Miwa, and H. Misawa, *Nanotechnology* 16, 846 (2005).
17. T. S. Drakakis, G. Papadakis, K. Sambani, G. Filippidis, S. Georgiou, E. Gizeli, C. Fotakis, and M. Farsari, *Appl. Phys. Lett.* 89, 144108 (2006).
18. H. B. Sun, T. Tanaka, K. Takada, and S. Kawata, *Appl. Phys. Lett.* 79, 1411 (2001).
19. C. N. LaFratta, J. T. Fourkas, T. Baldacchini, and R. A. Farrer, *Angewandte Chemie—International Edition* 46, 6238 (2007).
20. M. Kumar, *Reactive & Functional Polymers* 46, 1 (2000).
21. Q. L. Hu, B. Q. Li, M. Wang, and J. C. Shen, *Biomaterials* 25, 779 (2004).
22. T. Dvir, O. Tsur-Gang, and S. Cohen, *Israel Journal of Chemistry* 45, 487 (2005).
23. Y. Okamoto, R. Yano, K. Miyatake, I. Tomohiro, Y. Shigemasa, and S. Minami, *Carbohydrate Polymers* 53, 337 (2003).
24. K. Y. Lee, W. S. Ha, and W. H. Park, *Biomaterials* 16, 1211 (1995).
25. S. Sagnella and K. Mai-Ngam, *Colloids and Surfaces B—Biointerfaces* 42, 147 (2005).
26. D. S. dos Santos, A. Riul, R. R. Malmegrim, F. J. Fonseca, O. N. Oliveira, and L. H. C. Mattoso, *Macromolecular Bioscience* 3, 591 (2003).
27. A. Riul, H. C. de Sousa, R. R. Malmegrim, D. S. dos Santos, A. Carvalho, F. J. Fonseca, O. N. Oliveira, and L. H. C. Mattoso, *Sensors and Actuators B—Chemical* 98, 77 (2004).
28. H. W. Tong and M. Wang, *J. Nanosci. Nanotechnol.* 7, 3834 (2007).
29. Y. Wan, K. A. M. Creber, B. Peppley, and V. T. Bui, *Polymer* 44, 1057 (2003).
30. D. S. dos Santos, A. Bassi, J. J. Rodrigues, L. Misoguti, O. N. Oliveira, and C. R. Mendonça, *Biomacromolecules* 4, 1502 (2003).
31. C. S. Camilo, D. S. dos Santos, J. J. Rodrigues, M. L. Vega, S. P. Campana, O. N. Oliveira, and C. R. Mendonça, *Biomacromolecules* 4, 1583 (2003).
32. B. Sarmento, A. J. Ribeiro, F. Veiga, D. C. Ferreira, and R. J. Neufeld, *J. Nanosci. Nanotechnol.* 7, 2833 (2007).
33. L. Illum, *Pharmaceutical Research* 15, 1326 (1998).
34. P. Calvo, C. RemunanLopez, J. L. VilaJato, and M. J. Alonso, *J. Appl. Polym. Sci.* 63, 125 (1997).
35. A. Berthold, K. Cremer, and J. Kreuter, *Journal of Controlled Release* 39, 17 (1996).
36. T. Baldacchini, C. N. LaFratta, R. A. Farrer, M. C. Teich, B. E. A. Saleh, M. J. Naughton, and J. T. Fourkas, *J. Appl. Phys.* 95, 6072 (2004).
37. C. R. Mendonça, D. S. Correa, T. Baldacchini, P. Tayalia, and E. Mazur, *Applied Physics A—Materials Science & Processing* 90, 633 (2008).
38. W. A. Bough, W. L. Salter, A. C. M. Wu, and B. E. Perkins, *Biotechnology and Bioengineering* 20, 1931 (1978).
39. M. Lavertu, Z. Xia, A. N. Serreqi, M. Berrada, A. Rodrigues, D. Wang, M. D. Buschmann, and A. Gupta, *Journal of Pharmaceutical and Biomedical Analysis* 32, 1149 (2003).
40. Characterization and Failure Analysis of Plastics, ASM International, Materials Park, OH (2003).

Received: 7 October 2008. Accepted: 20 November 2008.

Numerical aperture dependence of damage and supercontinuum generation from femtosecond laser pulses in bulk fused silica

Jonathan B. Ashcom,* Rafael R. Gattass, Chris B. Schaffer,[†] and Eric Mazur

Department of Physics and Division of Engineering and Applied Sciences, Harvard University, 9 Oxford Street, Cambridge, Massachusetts 02138

Received January 13, 2006; revised July 18, 2006; accepted July 23, 2006; posted July 26, 2006 (Doc. ID 66335)

Competing nonlinear optical effects are involved in the interaction of femtosecond laser pulses with transparent dielectrics: supercontinuum generation and multiphoton-induced bulk damage. We measured the threshold energy for supercontinuum generation and bulk damage in fused silica using numerical apertures (NAs) ranging from 0.01 to 0.65. The threshold for supercontinuum generation exhibits a minimum near 0.05 NA and increases quickly above 0.1 NA. For NAs greater than 0.25, we observe no supercontinuum generation. The extent of the blue broadening of the supercontinuum spectrum decreases significantly as the NA is increased from 0.01 to 0.08, showing that weak focusing is important for generating the broadest supercontinuum spectrum. Using a light-scattering technique to detect the onset of bulk damage, we confirmed bulk damage at all NAs studied. At a high NA, the damage threshold is well below the critical power for self-focusing. © 2006 Optical Society of America

OCIS codes: 320.2250, 260.5950, 140.3440, 160.6030.

1. INTRODUCTION

When femtosecond pulses are strongly focused into a transparent material, permanent damage can be produced in the bulk of the material via nonlinear absorption.^{1–3} Although weakly focused femtosecond pulses can also produce bulk damage,^{4,5} significantly more energy is required than under strong-focusing conditions and such pulses tend to generate a considerable amount of supercontinuum light.⁶ The pulse's spectrum broadens considerably as it propagates, resulting in the formation of a broad flat pedestal on the blue side of the spectrum (blue broadening).^{6,7} The fact that otherwise identical laser pulses produce damage when strongly focused and generate a supercontinuum when weakly focused shows that the numerical aperture (NA) is a critical parameter that governs how femtosecond laser pulses interact with and propagate in transparent materials. In this paper we study how the focusing conditions affect bulk damage and supercontinuum generation by femtosecond laser pulses in fused silica.

Laser-induced breakdown and supercontinuum generation have been studied extensively.^{6–9} The role of focusing conditions in the breakdown and supercontinuum generation in CO₂ gas and in water has been investigated with picosecond^{10,11} and femtosecond pulses.¹² The effect of the NA on femtosecond pulse propagation and supercontinuum generation has also been investigated in solids using numerical simulations^{13,14} and experimentally in fused silica.⁹ The experimental work in fused silica, however, was limited to NAs ranging from 0.03 to 0.29 and identified the detection of radiation at 400 nm as the threshold for supercontinuum, as opposed to looking for the onset of blue broadening.

Here we report the results of a systematic study of the

energy threshold for bulk damage and supercontinuum generation using femtosecond pulses in fused silica as a function of the NA of the external focusing optics. While femtosecond pulse-induced damage is an intensity-dependent effect, self-focusing makes the unambiguous determination of the focused spot size within the bulk challenging, and hence we use the pulse energy as the fundamental quantity in this study, as it is the quantity over which the experimenter has direct control. Our results indicate that the interaction of femtosecond laser pulses with transparent materials falls into three regimes, depending on the NA. We find that bulk damage can be produced at all NAs investigated ($0.1 < \text{NA} < 0.65$), but that supercontinuum generation does not occur at 0.25 NA or higher (the “high-NA regime”). In the range from 0.05 to 0.15 NA (the “medium-NA regime”), we observe the supercontinuum generation, but multiple shots show the accumulation of bulk damage, causing the supercontinuum to disappear. Finally, below 0.05 NA (the “low-NA regime”), it is possible to damage the bulk, but only at energies significantly above the threshold for the supercontinuum generation. The morphology of the damage is found to be different for high and low NA. For damage induced at low NAs, we observe multiple refocusing of the femtosecond laser pulse. We also show that the extent of the blue broadening in the supercontinuum diminishes with an increasing NA.

2. EXPERIMENTAL SETUP

The experiments were carried out using a multipass-amplified Ti:sapphire laser operating at 1 kHz with a center wavelength of 800 nm, a 40 nm spectral width, a pulse duration of 60 fs, and pulse to pulse energy fluctuations

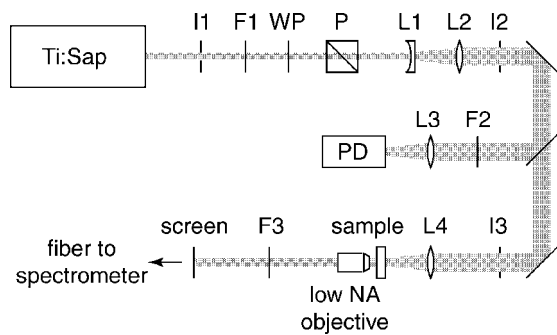


Fig. 1. Schematic of the setup used for damage and supercontinuum experiments. I1, I2, I3, iris; F1, F2, F3, neutral density filter wheels; WP, waveplate; P, polarizer; L1, L2, 3 \times telescope; L3, 0.2 m focal lens; L4, sample focusing lens-objective (varied throughout experiment); PD, photodiode. All collection optics are UV-grade fused silica transparent down to 300 nm.

below 2%. Amplification is required to reach the critical power for self-focusing (about 300 nJ for a 60 fs pulse^{7,15}). Additionally, the low repetition rate of the laser allows the sample to be translated during irradiation so that each successive pulse hits an unexposed area.

All experiments were carried out on UV-grade fused silica samples (ESCO commercial quality SI-UV; <5 waves/inch; 60–40 scratch-dig or better surface quality). For the experiments carried out at focusing conditions below 0.1 NA, we used 12 mm thick samples to ensure that all high-intensity propagation was confined to the bulk. At higher NAs we used thinner (1.0 and 3.0 mm) samples.

A schematic of the experimental setup is shown in Fig. 1. Because the key parameter in this study is the focusing angle of the incident pulse, beam quality is of critical importance. We therefore spatially filtered the 6 mm unfocused beam exiting the laser system using an iris (I1) so that a small section (approximately 0.5 mm in diameter) of the beam of relatively uniform intensity passes through, diffracting into an Airy pattern in the far field. This mode propagates 3 m and is then expanded by a factor of 3 using a telescope (L1, L2). A second iris (I2) spatially filters the central spot of the Airy pattern. This central spot, which is nearly Gaussian, is imaged with a CCD camera to measure mode shape and spot size. A fraction of the transmitted beam, which has a $1/e^2$ diameter of about 7–8 mm, is split off and focused onto a calibrated photodiode (PD) to monitor the energy of each pulse incident on the sample. The pulse energy can be varied continuously over a large range using a combination of a half-waveplate (WP) and a Glan-laser polarizer (P), as well as a filter wheel (F1) that spans 3 OD (optical density) in 0.1 OD steps.

To focus at low NAs we used commercial BK7 and fused silica singlet lenses with focal lengths ranging from 300 mm to 50 mm. Using these lenses and a beam diameter of 7–8 mm we obtained NAs between 0.01 and 0.08. Above 0.16 NA, the spherical aberration introduced by a singlet lens degrades diffraction-limited focusing, so we used microscope objectives to obtain diffraction-limited spots at NAs ranging from 0.10 to 0.65. We observe that the damage threshold plateaus or has a slight minimum with the focus at a depth of roughly two confocal param-

eters. Therefore, we choose two confocal parameters as the depth for consistent bulk damage threshold measurements.

The BK7 and fused silica singlet lenses do not introduce appreciable dispersion [approximately $-160 \text{ ps km}^{-1} \text{ nm}^{-1}$ (Ref. 16)], and therefore the pulse duration was minimized at the input of the focusing lens. The multiple elements and different glasses in high-NA microscope objectives, however, cause significant dispersion, and so the pulse must be prechirped to compensate for this dispersion. We therefore adjusted the grating pulse compressor to obtain the lowest energy damage threshold in the sample. The pulse width at the focus is then roughly equal to the shortest pulse duration measured in front of the objective.¹⁷

A. Experimental Procedure—Supercontinuum Generation

As the threshold for supercontinuum generation we use the energy required to broaden the pulse spectrum such that 720 nm radiation is just visible to the dark-adapted eye. The supercontinuum generated is passed through a Schott BG40 filter, which passes the visible and begins to cut on strongly around 600 nm, to block the intense 800 nm portion of the spectrum. We chose this criterion because 720 nm is near the long-wavelength edge of the asymmetric blue-broadening characteristic of supercontinuum generation. Once we determined the energy threshold for a given NA, we increased the pulse energy by 60% and 100% and recorded the resulting supercontinuum spectra. Because at some NAs damage occurs below the supercontinuum threshold, the sample is continuously translated at 20 mm/s while spectra are collected, so that each pulse is incident on a fresh section of the sample.

Figure 2 shows a typical supercontinuum spectrum. An important metric for evaluating the supercontinuum is the extent to which the spectrum has been blue broadened. The edge of the blue broadening is chosen as the

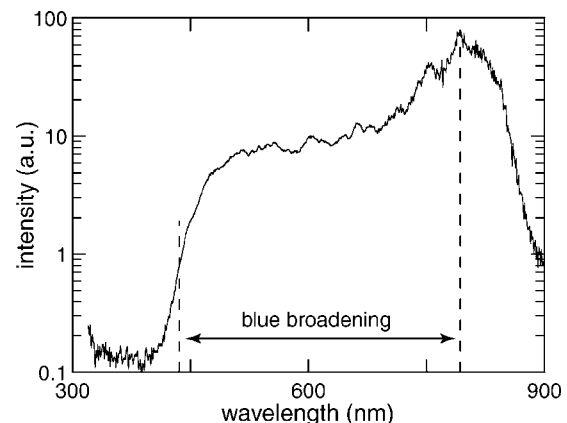


Fig. 2. Typical supercontinuum spectrum produced by a 60 fs, 480 nJ 800 nm laser pulse (1.6 times the supercontinuum threshold) focused at 0.025 NA. The value at the 800 nm peak is attenuated due to the spectrometer's limited dynamic range (typically, the pedestal is down by 100 to 500 times). The blue-broadening width is measured from the laser's center wavelength (800 nm) to the wavelength where the intensity of the supercontinuum spectrum is reduced to 10% of its plateau value.

wavelength where the intensity has dropped to 10% of the average intensity of the flat pedestal (dashed line in Fig. 2). The blue broadening is defined as the difference in photon energy between this edge and the 800 nm seed pulse, as indicated in Fig. 2.

B. Experimental Procedure—Bulk Damage

We measured the damage threshold using a previously reported scattering technique.¹⁸ A He–Ne probe laser beam propagates collinearly with the femtosecond laser pulse and reaches a focus at the same spot as the femtosecond laser. A beam block prevents the undisturbed He–Ne signal from reaching the detector. The damage threshold is determined by capturing the scattering of a He–Ne laser probe beam caused by material modification at the focal spot and recording it on a PD.

Contrary to the damage produced by longer pulses, femtosecond pulse-induced damage exhibits a sharp intensity threshold.^{3,19,20} We observe that the measured value of this threshold (using the pulse energy as a metric) depends on the incident number of shots because both the size of the damage structure and the magnitude of the index change increase with each successive laser shot, and the scattering technique has a lower limit of sensitivity. We investigated this dependence by measuring the He–Ne scattered signal versus pulse energy at a number of NAs, for 1 to 10,000 incident pulses. The energy damage threshold (E_{th}^D) decreases with an increasing number of pulses and plateaus as the number of pulses per spot increases to 5000 pulses (confirmed for NAs of 0.1, 0.25, 0.45, and 0.65). This measurement calibrates the scattering apparatus, and hence the damage threshold we report is for 5000-pulses. For these damage threshold measurements, the sample is stationary for the duration of a given 5000-pulse exposure, and then translated to a fresh region prior to continuing the experiment.

3. RESULTS

Figure 3 shows how the extent of the blue broadening decreases with increasing NA. The data obtained at both 1.6 and 2.0 times the supercontinuum threshold energy (E_{th}^S) show the same trend, emphasizing that weak focusing should be used to obtain the broadest supercontinuum spectrum. Around 0.05 NA the shape of the spectrum

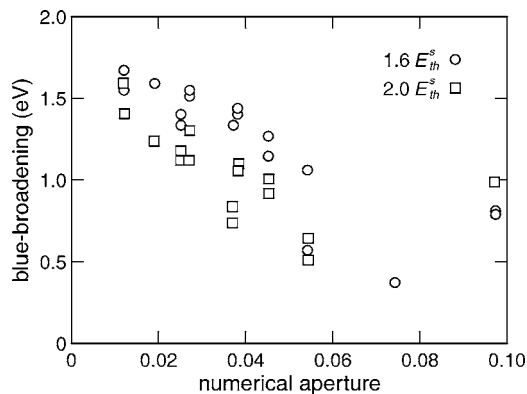


Fig. 3. NA dependence of the blue broadening at two different pulse energies.

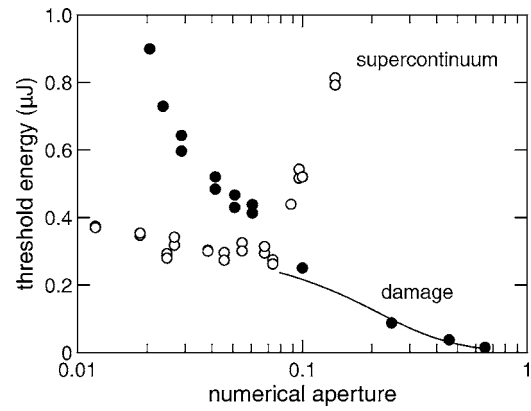


Fig. 4. Energy thresholds for damage (filled circles) and supercontinuum generation (open circles) versus NA. The black curve is a constant peak intensity fit of Eq. (1) to the damage data obtained for NAs above 0.1.

changes: at a lower NA the spectrum shows the characteristic blue-broadened pedestal seen in Fig. 2; at higher NAs the broadening is much more symmetric. Above 0.05 NA the supercontinuum generation also decreases when thousands of successive pulses are incident on the same spot, suggesting a slow buildup of damage. Above 0.1 NA, the damage threshold is lower than the supercontinuum generation threshold and plasma emission may contribute to the recorded spectrum²¹ resulting in unreliable data for the blue broadening.

Figure 4 shows how the energy thresholds for supercontinuum generation and bulk damage depend on the NA. Below 0.07 NA, the threshold for supercontinuum generation is roughly constant at 300 nJ. Above 0.07 NA, however, the threshold quickly increases, and by 0.25 NA, no supercontinuum is observed up to the highest pulse energy, 10 μJ, available.

The threshold power for the onset of supercontinuum generation is the same as the critical power for self-focusing in a wide range of transparent materials,^{10,22–24} supporting the hypothesis that supercontinuum generation is triggered by self-focusing. For the 60 fs pulse used in this experiment, the threshold energy value for supercontinuum generation of 300 nJ corresponds to a peak power of 4.9 MW, roughly consistent with the 4.3 MW critical power for self-focusing in fused silica.^{8,18}

For pulse energies below the energy corresponding to the critical power, the effects of self-focusing can be taken into account and the focused spot size can be reliably predicted,²⁵ yielding the following relation between pulse energy, intensity, and NA:

$$E = \frac{I\tau\lambda^2}{0.9} \left[2\pi \frac{NA^2}{1 - NA^2} + \frac{I\lambda^2}{P_{crit}} \right]^{-1}. \quad (1)$$

Using the critical power $P_{crit} = 4.9$ MW obtained above, we can fit this expression to the three damage threshold data points with $NA > 0.10$ using the intensity as a fitting parameter. The result is shown in Fig. 4, and yields a threshold of $1.0 \times 10^{18} \text{ W/m}^2$ (67 kJ/m² peak fluence), consistent with the breakdown intensities reported for other transparent materials of similar bandgap.^{2,18,19,26–28} The fit becomes inaccurate as the threshold energy approaches the energy associated with the critical power

and the assumption of weak self-focusing is no longer valid.

Figure 5 shows the scattering of He–Ne laser light due to bulk damage as a function of incident pulse energy for three different NAs. As can be seen for 0.45 NA, there is a sharp energy damage threshold, indicated by the abrupt linear increase in the scattered signal. We do not observe such a sharp threshold at NAs below 0.1; instead the scattering intensity gradually increases as the pulse energy is increased (see, e.g., the data for 0.035 NA in Fig. 5). The sharp threshold exhibited in the high NA regime (0.25 NA or greater) is generally associated with the onset of multiphoton ionization.^{3,18–20,27,29} Our data therefore suggest that the damage observed at NAs above 0.1 are due to multiphoton ionization of the material at the focus. The gradual increase in scattering observed below 0.1 NA suggests that a different mechanism is at play at these lower NAs.

Previous work has shown that at a high NA (0.65 to 1.4 NA) and pulse energies near the damage threshold, the extent of the damage is found to be roughly equal in size to the focal volume.³⁰ At energies significantly above threshold, the threshold intensity for damage is reached

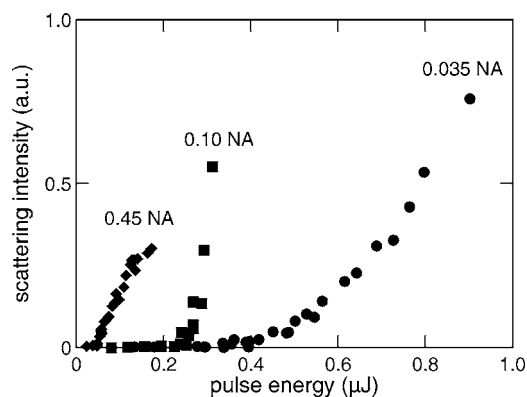


Fig. 5. Dependence of the He–Ne laser scattering signal on pulse energy and NA. For each data point the scattering intensity was determined after accumulating 5000 pulses on a single spot in the sample.

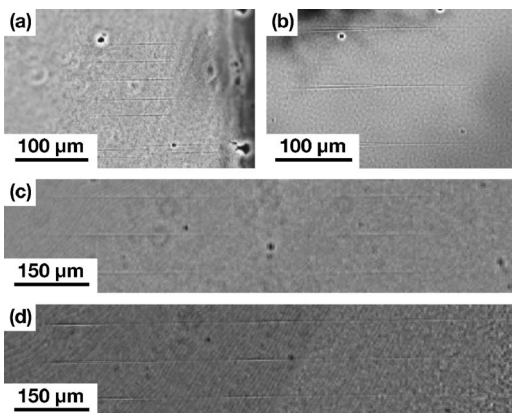


Fig. 6. Contrast-enhanced microscopy images of bulk damage in fused silica at low NA. The laser pulse is incident from the right. Vertically offset lines represent multiple repetitions of the experiment. The images are for an exposure of 10,000 pulses with (a) 0.055 NA at two times the damage threshold ($2E_{th}^D$), (b) 0.033 NA at $3E_{th}^D$, (c) 0.019 NA at $2E_{th}^D$, and (d) 0.020 NA at $3E_{th}^D$.

early in the pulse, as the leading edge reaches the focus. However, the more intense regions of the pulse produce above-threshold intensities in front of the focus, where the spot size is larger, resulting in a cone-shaped damage area.³⁰ We used side-view optical microscopy to confirm that damage was confined to the bulk and to determine if there is any change in the damage morphology as the NA is lowered. To this end we polished two opposite thin sides of a 1.5 mm thick, 25 mm × 25 mm square sample of fused silica and exposed the sample with the polished edges normal to the incident beam at NAs ranging from 0.019 to 0.25 and energies from threshold to nearly ten times threshold. Because the damage generated at a low shot number does not yield significant changes in the index of refraction, each spot was exposed to 10,000 pulses. In all cases, the damage is confined to the bulk; we did not observe any surface damage.

As in the previous study, our results showed that in the high NA regime the structures produced in the bulk near the energy threshold match the confocal parameter in length, but for low NAs the structures are shorter than the confocal parameter. Figure 6 shows representative optical microscope images of the 10,000-pulse damage in the medium and low NA regime. At 0.055 NA the confocal parameter is 255 μm, but the structures produced near the threshold energy extend for only 130 μm [Fig. 6(a)]. As the NA is reduced, the discrepancy between the confocal parameter and the length of the structure increases. At 0.033 NA the structures begin to include the conical region in front of the focus [Fig. 6(b)]. Including this conical region the observable structure is only about 230 μm long, while the confocal parameter is about 700 μm. At 0.023 NA, the confocal parameter is 1.4 mm, but the structure length near the threshold is only 290 μm long. At 0.019 NA the damage structures break up into two disconnected regions [see Fig. 6(c)], but the overall length of the structures is still much shorter than the confocal parameter.

In the low NA regime, the damage structures break up as the energy is increased to several times the energy threshold. For example, at 0.033 NA the single, cone-shaped damage structure seen in Fig. 6(b) breaks up into two regions similar to those seen in Fig. 6(c) when the energy is increased to four times the energy threshold. The region closest to the source is still cone shaped; the second region is located farther away from the source and is line shaped. The breaking up of the damage structures thus depends not only on the focusing conditions, but also on the laser energy.

We also investigated the dependence of the damage morphology on the number of laser pulses. To this end we made a series of damage structures at 0.020 NA and three times the energy threshold varying the number of laser pulses. At 1000 pulses two zones of damage are visible and at 5000 pulses a third zone becomes visible downstream. As more pulses accumulate, the three zones become more clearly visible [see Fig. 6(d)].

4. DISCUSSION

Our results indicate that the interaction of femtosecond laser pulses with transparent materials falls into three

regimes, depending on NA. For NAs larger than 0.25, we observe bulk damage above a certain pulse energy threshold but never any supercontinuum. In the range from 0.15 to 0.05 NA, we observe supercontinuum generation but multiple shots show the accumulation of bulk damage, causing the supercontinuum to disappear over time. Finally, below 0.05 NA, it is possible to damage the bulk, but only at energies significantly above the threshold for supercontinuum generation.

In the high-NA regime, the laser pulse energy at the damage threshold is not high enough to reach the critical power for self-focusing, and hence the external focusing dominates. The beam converges rapidly, producing intensities around 10^{18} W/m² and creating a carrier density of approximately 10^{27} m⁻³ via nonlinear absorption.³ Most of the pulse energy is thus deposited into the material at the focal volume either through nonlinear absorption or subsequent linear absorption by the plasma, resulting in bulk damage. What is left of the pulse quickly diverges after the focus. Because the pulse does not propagate at high intensity for an appreciable distance there is no interaction length over which self-phase modulation can accumulate or an optical shock can form and so no supercontinuum is generated.¹⁴ Even at pulse energies exceeding the critical power we observe no supercontinuum. The absorption of energy at the focus prevents the subsequent recollapse of the pulse via self-focusing. Indeed, a previous study¹⁸ confirmed that when $3\text{ }\mu\text{J}$, 110 fs pulses are focused into fused silica at 0.65 NA, the energy remaining in the pulse after propagation through the focus is always below the critical power at that pulse width.

At low NA, self-focusing increases the pulse intensity as it propagates through the sample. The increasing intensity creates a low-density electron plasma (10^{24} m⁻³) that counteracts self-focusing,^{8,14,15} prevents the formation of a critical density plasma, and prevents single-shot damage at energies available in our experiments. Supercontinuum is generated by the accumulation of self-phase modulation, self-steepening, and space-time focusing while the pulse propagates as a filament.^{14,31,32} As the NA is increased, the confocal parameter becomes smaller, yielding a shorter interaction length and therefore less blue-broadening.

The NA regime simply represents the transition between these two extremes. As the NA is decreased and the focused spot size increases, more energy is required to reach the breakdown intensity, bringing the pulse closer to or above the critical power for self-focusing. The more that self-focusing dominates the effects of the external focusing (NA), the closer the interaction moves toward the low-NA regime.

The optical microscopy images in Fig. 6 and the scattering intensity data suggest that the damage mechanism is different in the low- and high-NA regimes. The low-NA damage shows filaments that are much shorter than the confocal parameter of the external focusing. Also, there is no sharp energy threshold for damage at low NA (Fig. 5). It is possible that the supercontinuum that occurs at low NA causes color center formation or densification. Indeed, the formation of color centers was observed in the bulk of some silicate glasses under weakly focused femtosecond

irradiation.³³ This color center formation was attributed to the linear and two-photon absorption of the blue edge of the supercontinuum.³³ Additionally, ultraviolet radiation is known to cause densification of silica³⁴ and is widely used in the writing of fiber Bragg gratings.³⁵ At a high NA, on the other hand, the damage mechanism can be attributed to a combination of multiphoton absorption and avalanche ionization.^{3,18–20,27,29}

The breaking up of the damage structures shown in Figs. 6(c) and 6(d) can be attributed to the refocusing of femtosecond pulses in fused silica. Refocusing of femtosecond beams has been modeled^{36,37} and observed in air³⁸ and liquids³⁹ and imaged by plasma emission in solids at high⁴⁰ and low⁴¹ NAs. The multiple zones of damage we observe at a low NA are consistent with the observed plasma emission due to refocusing of femtosecond laser beams in fused silica.⁴¹

In conclusion, we studied the role of the NA of the external focusing in the interaction of femtosecond laser pulses with transparent materials. At a high NA (above 0.25 NA), single-shot, catastrophic damage occurs, and no supercontinuum generation is observed. Below 0.15 NA we observe supercontinuum generation and damage at a threshold significantly above the threshold for supercontinuum generation. Bulk micromachining is only practical for NAs of 0.25 NA and above, where self-focusing effects are minimal and spot size and focal position can be accurately predicted and controlled. Further, as the NA is increased, the energy necessary to cause material modification decreases, minimizing collateral damage. While supercontinuum can be produced at any NA below 0.15 NA, the spectrum is broadest at the lowest NA. Also, at the lowest NA, the supercontinuum is produced well below the damage threshold. Below 0.05 NA we observe multiple refocusing of the femtosecond laser beam. The results presented in this paper show that the NA, a linear optical parameter which is independent of the laser parameters, controls the interaction of ultrashort laser pulses with transparent materials, a highly nonlinear process.

ACKNOWLEDGMENTS

The research described in this paper was supported by the National Science Foundation under contracts PHY-998123 and DMI-0334984, and the Army Research Office under contract W911NF-05-1-0471. The authors would also like to acknowledge the use of the facilities of the Center for Nanoscale Systems, which is supported by the National Science Foundation's National Nanotechnology Infrastructure Network.

*Present address, MIT Lincoln Laboratory, Lexington, MA 02420.

†Present address, Department of Biomedical Engineering, Cornell University, Ithaca, NY 14853.

REFERENCES

1. E. N. Glezer, M. Milosavljevic, L. Huang, R. J. Finlay, T. H. Her, J. P. Callan, and E. Mazur, "Three-dimensional optical storage inside transparent materials," *Opt. Lett.* **21**, 2023–2025 (1996).

2. A. C. Tien, S. Backus, H. Kapteyn, M. Murnane, and G. Mourou, "Short-pulse laser damage in transparent materials as a function of pulse duration," *Phys. Rev. Lett.* **82**, 3883–3886 (1999).
3. B. C. Stuart, M. D. Feit, S. Herman, A. M. Rubenchik, B. W. Shore, and M. D. Perry, "Nanosecond-to-femtosecond laser-induced breakdown in dielectrics," *Phys. Rev. B* **53**, 1749–1761 (1996).
4. D. Ashkenasi, H. Varel, A. Rosenfeld, S. Henz, J. Herrmann, and E. E. B. Campbell, "Application of self-focusing of ps laser pulses for three-dimensional microstructuring of transparent materials," *Appl. Phys. Lett.* **72**, 1442–1444 (1998).
5. K. Yamada, W. Watanabe, T. Toma, K. Itoh, and J. Nishii, "In situ observation of photoinduced refractive-index changes in filaments formed in glasses by femtosecond laser pulses," *Opt. Lett.* **26**, 19–21 (2001).
6. R. R. Alfano and S. L. Shapiro, "Observation of self-phase modulation and small-scale filaments in crystals and glasses," *Phys. Rev. Lett.* **24**, 592–594 (1970).
7. A. Brodeur and S. L. Chin, "Ultrafast white-light continuum generation and self-focusing in transparent condensed media," *J. Opt. Soc. Am. B* **16**, 637–650 (1999).
8. A. Brodeur and S. L. Chin, "Band-gap dependence of the ultrafast white-light continuum," *Phys. Rev. Lett.* **80**, 4406–4409 (1998).
9. N. T. Nguyen, A. Salimnia, W. Liu, S. L. Chin, and R. Vallee, "Optical breakdown versus filamentation in fused silica by use of femtosecond infrared laser pulses," *Opt. Lett.* **28**, 1591–1593 (2003).
10. F. A. Ilkov, L. S. Ilkova, and S. L. Chin, "Supercontinuum generation versus optical-breakdown in CO₂ gas," *Opt. Lett.* **18**, 681–683 (1993).
11. Q. Feng, J. V. Moloney, A. C. Newell, and E. M. Wright, "Laser-induced breakdown versus self-focusing for focused picosecond pulses in water," *Opt. Lett.* **20**, 1958–1960 (1995).
12. W. Liu, O. Kosareva, I. S. Golubtsov, A. Iwasaki, A. Becker, V. P. Kandidov, and S. L. Chin, "Femtosecond laser pulse filamentation versus optical breakdown in H₂O," *Appl. Phys. B* **76**, 215–229 (2003).
13. M. R. Junnarkar, "Short pulse propagation in tight focusing conditions," *Opt. Commun.* **195**, 273–292 (2001).
14. A. L. Gaeta, "Catastrophic collapse of ultrashort pulses," *Phys. Rev. Lett.* **84**, 3582–3585 (2000).
15. J. H. Marburger, "Self-focusing: theory," *Prog. Quantum Electron.* **4**, 35–110 (1975).
16. B. E. A. Saleh and M. C. Teich, *Fundamentals of Photonics*, Wiley Series in Pure and Applied Optics (Wiley, 1991), pp. xviii.
17. M. Muller, J. Squier, and G. J. Brakenhoff, "Measurement of femtosecond pulses in the focal point of a high-numerical-aperture lens by two-photon absorption," *Opt. Lett.* **20**, 1038–1040 (1995).
18. C. B. Schaffer, A. Brodeur, and E. Mazur, "Laser-induced breakdown and damage in bulk transparent materials induced by tightly focused femtosecond laser pulses," *Meas. Sci. Technol.* **12**, 1784–1794 (2001).
19. B. C. Stuart, M. D. Feit, S. Herman, A. M. Rubenchik, B. W. Shore, and M. D. Perry, "Optical ablation by high-power short-pulse lasers," *J. Opt. Soc. Am. B* **13**, 459–468 (1996).
20. D. Du, X. Liu, G. Korn, J. Squier, and G. Mourou, "Laser-induced breakdown by impact ionization in SiO₂ with pulse widths from 7 ns to 150 fs," *Appl. Phys. Lett.* **64**, 3071–3073 (1994).
21. C. W. Carr, M. D. Feit, A. M. Rubenchik, P. De Mange, S. O. Kucheyev, M. D. Shirk, H. B. Radousky, and S. G. Demos, "Radiation produced by femtosecond laser-plasma interaction during dielectric breakdown," *Opt. Lett.* **30**, 661–663 (2005).
22. W. L. Smith, P. Liu, and N. Bloembergen, "Superbroadening in H₂O and D₂O by self-focused picosecond pulses from a YAlG:Nd laser," *Phys. Rev. A* **15**, 2396–2403 (1977).
23. P. B. Corkum, C. Rolland, and T. Srinivasanrao, "Supercontinuum generation in gases," *Phys. Rev. Lett.* **57**, 2268–2271 (1986).
24. J. K. Ranka, R. W. Schirmer, and A. L. Gaeta, "Observation of pulse splitting in nonlinear dispersive media," *Phys. Rev. Lett.* **77**, 3783–3786 (1996).
25. S. A. Akhmanov, R. V. Khokhlov, and A. P. Sukhorukov, "Self-focusing, self-defocusing and self-modulation of laser beams," in *Laser Handbook*, F. T. Arecchi, E. O. Schulz-Dubois, and M. L. Stitch, eds. (North-Holland, American Elsevier, 1972).
26. D. Du, X. Liu, and G. Mourou, "Reduction of multi-photon ionization in dielectrics due to collisions," *Appl. Phys. B* **63**, 617–621 (1996).
27. M. Lenzner, J. Kruger, S. Sartania, Z. Cheng, C. Spielmann, G. Mourou, W. Kautek, and F. Krausz, "Femtosecond optical breakdown in dielectrics," *Phys. Rev. Lett.* **80**, 4076–4079 (1998).
28. D. von der Linde and H. Schuler, "Breakdown threshold and plasma formation in femtosecond laser-solid interaction," *J. Opt. Soc. Am. B* **13**, 216–222 (1996).
29. W. Kautek, J. Kruger, M. Lenzner, S. Sartania, C. Spielmann, and F. Krausz, "Laser ablation of dielectrics with pulse durations between 20 fs and 3 ps," *Appl. Phys. Lett.* **69**, 3146–3148 (1996).
30. C. B. Schaffer, A. O. Jamison, and E. Mazur, "Morphology of femtosecond laser-induced structural changes in bulk transparent materials," *Appl. Phys. Lett.* **84**, 1441–1443 (2004).
31. F. Demartini, C. H. Townes, T. K. Gustafso, and P. L. Kelley, "Self-steepening of light pulses," *Phys. Rev.* **164**, 312–323 (1967).
32. J. E. Rothenberg, "Space-time focusing: breakdown of the slowly varying envelope approximation in the self-focusing of femtosecond pulses," *Opt. Lett.* **17**, 1340–1342 (1992).
33. O. M. Efimov, K. Gabel, S. V. Garnov, L. B. Glebov, S. Grantham, M. Richardson, and M. J. Soileau, "Color-center generation in silicate glasses exposed to infrared femtosecond pulses," *J. Opt. Soc. Am. B* **15**, 193–199 (1998).
34. D. C. Allan, C. Smith, N. F. Borrelli, and T. P. Seward, "193-nm excimer-laser-induced densification of fused silica," *Opt. Lett.* **21**, 1960–1962 (1996).
35. K. O. Hill, Y. Fujii, D. C. Johnson, and B. S. Kawasaki, "Photosensitivity in optical fiber waveguides—application to reflection filter fabrication," *Appl. Phys. Lett.* **32**, 647–649 (1978).
36. M. Mlejnek, M. Kolesik, E. M. Wright, and J. V. Moloney, "Recurrent femtosecond pulse collapse in air due to plasma generation: numerical results," *Math. Comput. Simul.* **56**, 563–570 (2001).
37. M. Mlejnek, E. M. Wright, and J. V. Moloney, "Dynamic spatial replenishment of femtosecond pulses propagating in air," *Opt. Lett.* **23**, 382–384 (1998).
38. A. Talebpour, S. Petit, and S. L. Chin, "Re-focusing during the propagation of a focused femtosecond Ti:sapphire laser pulse in air," *Opt. Commun.* **171**, 285–290 (1999).
39. W. Liu, S. L. Chin, O. Kosareva, I. S. Golubtsov, and V. P. Kandidov, "Multiple refocusing of a femtosecond laser pulse in a dispersive liquid (methanol)," *Opt. Commun.* **225**, 193–209 (2003).
40. Z. X. Wu, H. B. Jiang, L. Luo, H. C. Guo, H. Yang, and Q. H. Gong, "Multiple foci and a long filament observed with focused femtosecond pulse propagation in fused silica," *Opt. Lett.* **27**, 448–450 (2002).
41. Z. X. Wu, H. B. Jiang, H. Yang, and Q. H. Gong, "The refocusing behaviour of a focused femtosecond laser pulse in fused silica," *J. Opt. A, Pure Appl. Opt.* **5**, 102–107 (2003).

Reversible birefringence in microstructures fabricated by two-photon absorption polymerization

C. R. Mendonca^{a)}

Instituto de Física de São Carlos, Universidade de São Paulo, Caixa Postal 369, 13560-970, São Carlos, São Paulo, Brazil and Department of Physics and Division of Engineering and Applied Sciences, Harvard University, 9 Oxford Street, Cambridge, Massachusetts 02138

T. Baldacchini, P. Tayalia, and E. Mazur

Department of Physics and Division of Engineering and Applied Sciences, Harvard University, 9 Oxford Street, Cambridge, Massachusetts 02138

(Received 23 February 2007; accepted 23 May 2007; published online 10 July 2007)

This paper reports the fabrication of birefringent microstructures using two-photon absorption polymerization. The birefringence is caused by a light-driven molecular orientation of azoaromatic molecules (Disperse Red 13) upon excitation with an Ar⁺ laser at 514.5 nm. For an azoaromatic dye content of 1% by weight, we obtain a birefringence of 5×10^{-5} . This birefringence can be completely erased by overwriting the test spot with circularly polarized laser light or by heating the sample. Our results open the door to the development of alternative applications in optical data storage, waveguiding, and optical circuitry. © 2007 American Institute of Physics.

[DOI: [10.1063/1.2752113](https://doi.org/10.1063/1.2752113)]

INTRODUCTION

The interest in two-photon absorption induced processes has increased enormously during the past ten years. These processes involve the simultaneous absorption of two photons at wavelengths far from a material's linear absorption region. Whenever the material has an electronic energy level at twice the frequency of the input beam, two-photon absorption can occur. Because the two-photon absorption rate is proportional to the square of the excitation intensity, the absorption is confined to the focal volume. This nonlinear optical process has been used in applications requiring high spatial resolution such as two-photon microscopy,¹ two-photon photodynamic therapy,² and three-dimensional optical data storage.³ Two-photon absorption is also a valuable tool in the fabrication of complex three-dimensional microstructures because of the three-dimensional confinement of the nonlinear absorption process to the focal volume. In the past few years, two-photon absorption polymerization has been used to fabricate three-dimensional micromechanical actuators, photonic crystals, and optical devices.⁴

Most of the microstructures fabricated using two-photon polymerization are passive—their optical properties cannot be altered by external means.⁵ The lack of active elements motivated us to study microfabrication in photopolymerizable resins containing the azoaromatic chromophore DR13. The birefringence of these resins can be induced and erased optically, due to a reversible *trans-cis* photoisomerization of the azo group and a subsequent molecular orientation.^{6,7} In this paper we demonstrate the fabrication of optically active microstructures containing DR13 using two-photon absorption polymerization. The resulting microstructures become birefringent upon excitation with an Ar⁺ laser at 514.5 nm

and the optically induced birefringence can be erased with circularly polarized light or by heating the sample.

EXPERIMENT

The resin used in this work consists of a mixture of two triacrylate monomers and a monoacylphosphine oxide photoinitiator. We use tris(2-hydroxyethyl)isocyanurate triacrylate (monomer A) to increase the microstructure hardness and ethoxylated(6) trimethylolpropane triacrylate (monomer B) to reduce its shrinkage upon polymerization.⁸ The photoinitiator used to polymerize the resin is ethyl-2,4,6-trimethylbenzoylphenylphosphine.⁸ To the photosensitive resin we add Disperse Red 13, an azoaromatic chromophore which is known to exhibit photoinduced birefringence. We prepare ethanol solutions containing the desired proportion of monomers A and B (0%/100%, 30%/70%, 50%/50%, 70%/30%, 100%/0% by weight). To this solution we add DR13 (1% by weight), and stir it for 1 h in order to properly mix the components. Ethanol is then eliminated by evaporation at room temperature for 24 h, yielding a deep red viscous liquid. We add the photoinitiator (1% by weight) to this liquid and mix it for 1 h prior to use.

To evaluate the optical properties of the photopolymerized resin, we measured the absorbance of 200- μ m-thick films polymerized using an UV lamp. Figure 1 shows the absorption spectrum of such a polymerized film measured with a spectrophotometer equipped with an integrating sphere detector. The spectrum exhibits an absorption band at approximately 510 nm which corresponds to the $\pi \rightarrow \pi^*$ electronic transition of the azochromophore DR13. Excitation at 514.5 nm in this band is responsible for the photoisomerization and the subsequent molecular orientation process of DR13, yielding optical birefringence in the sample. The sample is completely transparent in the near infrared

^{a)}Electronic mail: crmendon@fas.harvard.edu

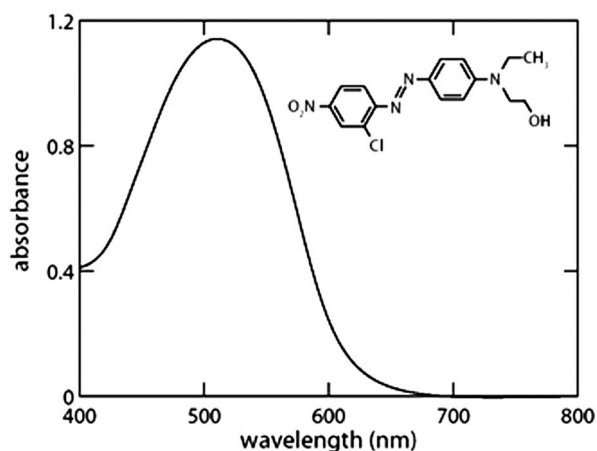


FIG. 1. Absorbance spectrum of a cast film (70% /30% by weight of monomers A and B) containing 1% of DR13. The inset shows the molecular structure of DR13.

region, where two-photon polymerization is carried out. We obtained identical spectra for all resin compositions.

To fabricate active microstructures, we place a drop of the resin inside a spacer located on a microscope slide whose surface is treated with (3 acryloxypropyl)trimethoxysilane in order to increase adhesion of the final structure to the glass substrate.⁸ After introducing the resin, a cover slip is placed on top of the spacer. The resin is polymerized using 130 fs pulses at 800 nm from a Ti:sapphire laser oscillator operating at 80 MHz. The average laser power is 20 mW before the 0.65 numerical aperture (NA) objective that focuses the laser beam into the sample. The sample is positioned in the axial z direction using a motorized stage, and the laser is scanned across the resin in the x - y direction with a pair of galvano mirrors. After fabricating the desired microstructure, the sample is immersed in ethanol to wash away any unsolidified resin and then dried.

RESULTS

To determine the composition that provides the largest and most stable birefringence, we studied the optically induced birefringence in films of various compositions. The birefringence in these films was induced by exposure to a continuous-wave, linearly polarized Ar^+ ion laser with an intensity of 6 kW/m^2 operating at 514.5 nm. To monitor the birefringence during the Ar^+ laser exposure, we measured the transmission of a low-power, linearly polarized 632.8 nm He-Ne laser beam through the sample and a set of crossed polarizer, as illustrated in Fig. 2.

Figure 3(a) shows the time evolution of the probe beam transmission for a 200- μm -thick film containing 70% /30% by weight of monomers A and B, respectively. Before exposure ($t < 60 \text{ s}$), the probe beam transmission is zero, indicating that the chromophores are isotropically distributed. When the Ar^+ ion laser is switched on at $t = 60 \text{ s}$, the transmission increases and saturates in about 1 min. At $t = 140 \text{ s}$ the Ar^+ ion laser is switched off and the transmission decreases to a nearly constant nonzero value of approximately 10% of the maximum value.

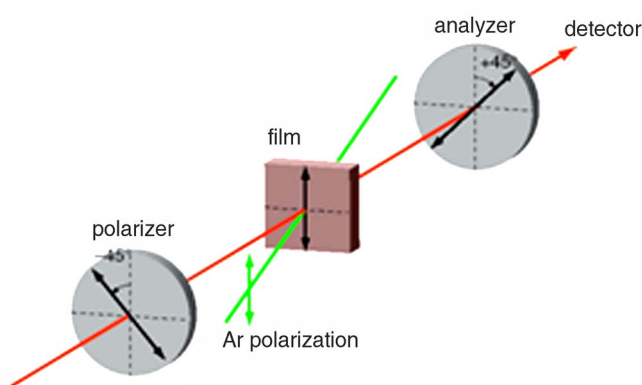


FIG. 2. (Color online) Experimental setup for birefringence measurements in film samples.

The optically induced birefringence Δn can be determined from the probe beam transmission T using

$$\Delta n = \lambda / \pi d \sin^{-1} \sqrt{T}, \quad (1)$$

where λ is the wavelength of the incident radiation and d is the film thickness.⁹ The maximum birefringence value achieved for this sample composition is 10^{-4} and the residual birefringence is about 4×10^{-5} . The residual birefringence can be completely erased with circularly polarized light or by heating the sample.

Films prepared with different resin compositions exhibit results similar to Fig. 3(a). Figure 3(b) shows the residual ratio for films that contain different proportions of monomers A and B (the final transmission divided by the maximum

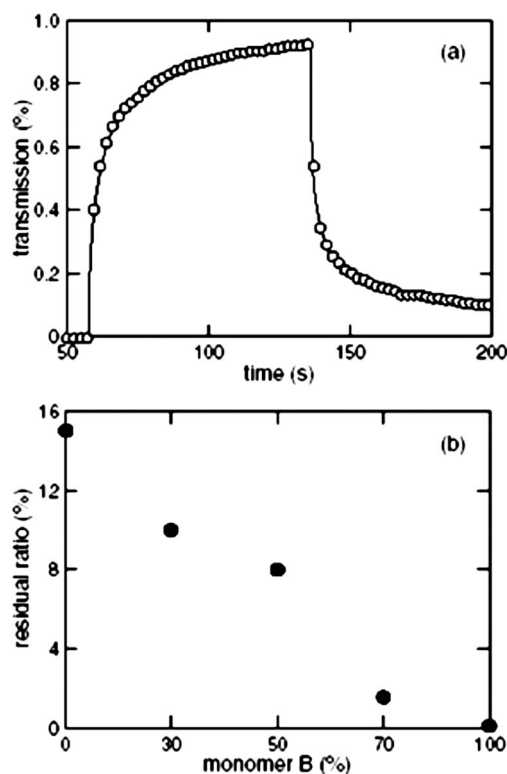


FIG. 3. (a) Time evolution of the transmission of an azopolymeric film illuminated by an Ar^+ laser between $t = 60 \text{ s}$ and $t = 140 \text{ s}$. (b) Dependence of the residual birefringence ratio obtained on resin composition.

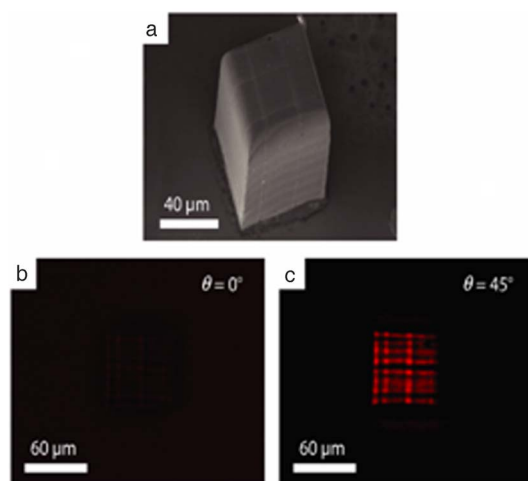


FIG. 4. (Color online) (a) Scanning electron micrograph of a solid square microstructure (70%/30% by weight of monomers A and B) containing DR13. The microstructure is about $70\text{ }\mu\text{m}$ tall, with transverse dimensions of approximately $60\text{ }\mu\text{m}$. [(b) and (c)] Polarization microscope images of a microstructure like the one shown in (a) at two angles between the polarizer and sample axis.

transmission). As expected, the residual ratio decreases with increasing concentration of monomer B in the resin because monomer A increases the hardness of the polymer. For the fabrication of the microstructures, we selected a composition of 70% (by weight) monomer A, 26% monomer B, 3% photoinitiator, and 1% Disperse Red 13. This composition yields a relatively high residual ratio while still containing enough of monomer B to minimize microstructure shrinkage upon polymerization.

We induced optical birefringence in the fabricated microstructures by irradiating the samples for 1 min with a polarized Ar^+ ion laser at an intensity of 6 kW/m^2 . After exposure to the Ar^+ ion laser light, the microstructure exhibits residual birefringence because the chromophore molecules become oriented in the direction perpendicular to the laser polarization. Figure 4 shows a scanning electron micrograph of a typical microstructure and the corresponding transmission microscope images obtained in the setup shown in Fig. 5. The microstructure is visible when the angle θ between the sample axis (defined by the Ar^+ ion laser exposure) and the

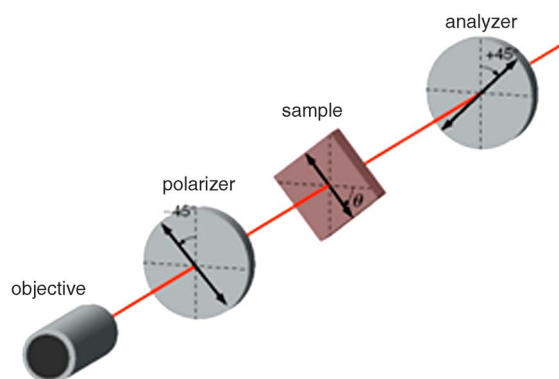


FIG. 5. (Color online) Experimental setup for birefringence measurements in microstructures.

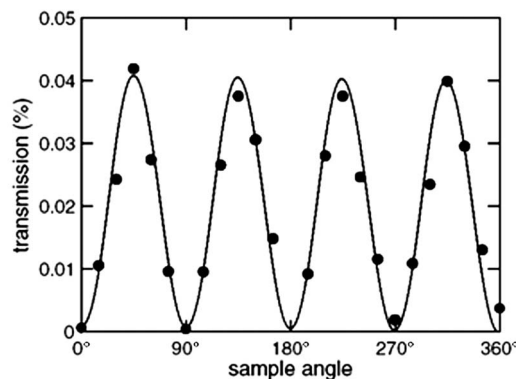


FIG. 6. Transmitted signal as a function of the sample angle θ for the microstructure shown in Fig. 4. The solid line represents a fit of Eq. (2) to the data.

polarizers is an odd multiple of 45° [Fig. 4(b)]; at even multiples of 45° the structure is not visible [Fig. 4(c)]. The stripes that are visible in the microstructure are surface imperfections that are produced during microfabrication.

Figure 6 shows the transmission of light as a function of the angle θ for the microstructure shown in Fig. 4. When the angle θ is zero, no light passes through the analyzer. The same occurs as the sample is rotated by integer multiples of 90° . Maximum transmission is obtained for angles that are odd multiples of 45° . The data in Fig. 6 show that the orientation of the chromophores in the microstructure leads to a sinusoidal behavior characteristic of birefringence. The solid line is obtained by fitting the following expression to the data:⁹

$$T = \sin^2\left(\frac{k\Delta nL}{2}\right)\sin^2(2\theta), \quad (2)$$

where k is the wave vector ($k=2\pi/\lambda$), Δn is the birefringence, and L is the sample thickness. Using a microstructure thickness $L=70\text{ }\mu\text{m}$, obtained from the scanning electron microscope [Fig. 4(a)], we obtain a birefringence value $\Delta n=5\times 10^{-5}$. This value is in good agreement with the one obtained for the same resin composition in a film ($\Delta n=4\times 10^{-5}$), as expected because this property should depend only on the polymer rigidity.

The induced birefringence in the microstructure can be completely erased by exposing it to circularly polarized light, using the same irradiance employed for the writing process. Under these conditions the erasing process takes about 1 min. Erasure can also be achieved by heating the sample for approximately 30 min to a temperature close to the polymer glass transition temperature.

DISCUSSION

The change in molecular orientation is brought about by the absorption of the pump beam light. Upon absorbing linearly polarized light of appropriate wavelength, the azochromophore undergoes a *trans-cis* isomerization. Subsequently, the *cis* form thermally relaxes back to the more stable *trans* form, a process that is accompanied by a change in the chromophore orientation.^{6,7} Once molecules have their dipole moments aligned perpendicular to the electric field, they no

longer absorb light and so they undergo no further conversions. At the end of several molecular isomerization cycles, the net result is a large fraction of molecules oriented perpendicularly to the laser polarization direction, yielding macroscopic birefringence.^{10,11} When the light source is switched off, molecular relaxation takes place, but a considerable number of molecules maintain their orientation, yielding stable birefringence. The low residual ratio observed in Fig. 3(a) is typical of azoaromatic dyes in guest-host films, where the chromophores are not covalently attached to the polymer chain and consequently there is large free volume for rotational diffusion.^{6,12} The final birefringence values remain stable for several weeks, despite exposure to ambient light, which suggests the microstructures may be sufficiently robust for optical applications. The writing and relaxation times for azoaromatic dyes in polymer films are usually on the order of several seconds, as expected for a molecular orientation mechanism. The maximum and residual values of induced birefringence are the most flexible parameters for engineering the optical properties of structures. Both values are determined by the polymer rigidity: a higher polymer rigidity yields a lower maximum induced birefringence.

Applications of these optically induced birefringent microstructures are limited by the small residual birefringence, which is a consequence of the large angular diffusion, typical of guest moieties in a polymer host. This limitation can be overcome if the azochromophore is attached as a side chain to the polymer backbone.^{11,13} The induced birefringence can also be enhanced by using different azochromophores or higher dye concentrations. Such modifications also affect the orientation response time, which might lead to faster response times.

The microstructures we fabricated, such as the one shown in Fig. 4(a), exhibit excellent integrity and good definition, indicating that the presence of the DR13 chromophore does not affect the two-photon absorption polymerization. Given the relatively small two-photon absorption cross section of DR13 (100 GM at 800 nm),¹⁴ we can conclude that this azocompound does not affect fabrication via two-photon absorption polymerization.

CONCLUSION

In conclusion, we demonstrated the fabrication of optically active microstructures doped with the azoaromatic compound DR13 via two-photon absorption polymerization. The optically induced birefringence achieved in our structures is caused by a light-driven orientation of the DR13 molecules. The optimum compositions for two-photon absorption polymerization and optically induced birefringence are 70% (by weight) of monomer A, 26% monomer B, 3% photoinitiator, and 1% Disperse Red 13. Using this combination, we achieved a birefringence of 5×10^{-5} . This birefringence can be completely erased with circularly polarized light or by heating the sample close to the polymer glass transition temperature.

ACKNOWLEDGMENTS

Several people contributed to the work described in this paper. One of the authors (C.R.M.) conceived the basic idea for this work and designed the experiment. Three of the authors (C.R.M., T.B., and P.T.) carried out the experiments. Another author (E.M.) supervised the research and edited the final manuscript. Other author (C.R.M.) wrote the first draft of the manuscript; all authors subsequently took part in the revision process. Eric Diebold, Geoffry Svacha, and Samuel Chung provided feedback on the manuscript throughout its development. The authors also would like to acknowledge Mustafa Haider-Syed for assistance with the birefringence measurements. The research described in this paper was supported by National Science Foundation under Contract No. DMI 0334984, the Army Research Office under Contract No. ARO W911NF-05-1-0471. The author (C.R.M.) acknowledges support from Fundação de Amparo a Pesquisa do Estado de São Paulo (FAPESP) and Coordenação de Aperfeiçoamento de Pessoal de Nível Superior (CAPES) from Brazil during his stay at Harvard University.

¹W. Denk, J. H. Strickler, and W. W. Webb, *Science* **248**, 73 (1990); R. H. Kohler, J. Cao, W. R. Zipfel, W. W. Webb, and M. R. Hansen, *ibid.* **276**, 2039 (1997).

²J. D. Bhawalkar, G. S. He, and P. N. Prasad, *Rep. Prog. Phys.* **59**, 1041 (1996); B. Herman, X. F. Wang, P. Wodnicki, A. Perisamy, N. Mahajan, G. Berry, and G. Gordon, in *Applied Fluorescence in Chemistry Biology and Medicine*, edited by B. Strehmel, W. Retting, S. Schrader, and H. Seifert (Springer, New York, 1999), p. 496.

³D. A. Parthenopoulos and P. M. Rentzepis, *Science* **245**, 843 (1989); A. S. Dvornikov and P. M. Rentzepis, *Opt. Commun.* **136**, 1 (1997); C. E. Olson, M. J. R. Previte, and J. T. Fourkas, *Nat. Mater.* **1**, 225 (2002).

⁴S. Kawata, H. B. Sun, T. Tanaka, and K. Takada, *Nature (London)* **412**, 697 (2001); F. Formanek, N. Takeyasu, T. Tanaka, K. Chiyoda, A. Ishikawa, and S. Kawata, *Opt. Express* **14**, 800 (2006); R. A. Farrer, C. N. LaFratta, L. J. Li, J. Praino, M. J. Naughton, B. E. A. Saleh, M. C. Teich, and J. T. Fourkas, *J. Am. Chem. Soc.* **128**, 1796 (2006).

⁵T. Watanabe, M. Akiyama, K. Totani, S. M. Kuebler, F. Stellacci, W. Wenseleers, K. Braun, S. R. Marder, and J. W. Perry, *Adv. Funct. Mater.* **12**, 611 (2002); H. B. Sun, T. Tanaka, K. Takada, and S. Kawata, *Appl. Phys. Lett.* **79**, 1411 (2001); S. Yokoyama, T. Nakahama, H. Miki, and S. Mashiko, *Thin Solid Films* **438**, 452 (2003).

⁶P. Rochon, J. Gosselin, A. Natansohn, and S. Xie, *Appl. Phys. Lett.* **60**, 4 (1992).

⁷T. Todorov, L. Nikolova, and N. Tomova, *Appl. Opt.* **23**, 4309 (1984).

⁸T. Baldacchini, C. N. LaFratta, R. A. Farrer, M. C. Teich, B. E. A. Saleh, M. J. Naughton, and J. T. Fourkas, *J. Appl. Phys.* **95**, 6072 (2004).

⁹E. Hecht and A. Zajac, *Optics* (Addison-Wesley, Reading, MA, 1974).

¹⁰S. Xie, A. Natansohn, and P. Rochon, *Chem. Mater.* **5**, 403 (1993); M. S. Ho, C. Barrett, J. Paterson, M. Esteghamat, A. Natansohn, and P. Rochon, *Macromolecules* **29**, 4613 (1996); T. S. Lee, D. Y. Kim, X. L. Jiang, L. A. Li, J. Kumar, and S. Tripathy, *Macromol. Chem. Phys.* **198**, 2279 (1997).

¹¹A. Natansohn, P. Rochon, C. Barrett, and A. Hay, *Chem. Mater.* **7**, 1612 (1995).

¹²X. Meng, A. Natansohn, and P. Rochon, *Polymer* **38**, 2677 (1997).

¹³C. R. Mendonça, D. S. dos Santos, D. T. Balogh, A. Dhanabalan, J. A. Giacometti, S. C. Zilio, and O. N. Oliveira, *Polymer* **42**, 6539 (2001); C. R. Mendonça, A. Dhanabalan, D. T. Balogh, L. Misoguti, D. S. dos Santos, M. A. Pereira-da-Silva, J. A. Giacometti, S. C. Zilio, and O. N. Oliveira, *Macromolecules* **32**, 1493 (1999).

¹⁴L. De Boni, L. Misoguti, S. C. Zilio, and C. R. Mendonça, *ChemPhysChem* **6**, 1121 (2005); L. De Boni, J. J. Rodrigues, D. S. dos Santos, C. Silva, D. T. Balogh, O. N. Oliveira, S. C. Zilio, L. Misoguti, and C. R. Mendonça, *Chem. Phys. Lett.* **361**, 209 (2002).

Faraday rotation in femtosecond laser micromachined waveguides

Tina Shih, Rafael R. Gattass, Cleber R. Mendonça†, Eric Mazur

Harvard School of Engineering and Applied Sciences, Harvard University, Cambridge, MA 02138

†Permanent address: Instituto de Física de São Carlos, Universidade de São Paulo,

Caixa Postal 369, 13560-970, São Carlos, SP, Brazil

mazur@physics.harvard.edu

<http://mazur-www.harvard.edu/>

Abstract: We demonstrate magneto-optic switching in femtosecond-laser micromachined waveguides written inside bulk terbium-doped Faraday glass. By measuring the polarization phase shift of the light as a function of the applied magnetic field, we find that there is a slight reduction in the effective Verdet constant of the waveguide compared to that of bulk Faraday glass. Electron Paramagnetic Resonance (EPR) measurements confirm that the micromachining leaves the concentration of the terbium ions that are responsible for the Faraday effect virtually unchanged.

©2007 Optical Society of America

OCIS codes: (320.7090) Ultrafast lasers; (230.7370) Waveguides; (230.2240) Faraday effect; (350.3390) Laser processing of materials.

References and links

1. K. M. Davis, K. Miura, N. Sugimoto, and K. Hirao, "Writing waveguides in glass with a femtosecond laser," *Opt. Lett.* **21**, 1729-1731 (1996).
2. C. Florea and K. A. Winick, "Fabrication and characterization of photonic devices directly written in glass using femtosecond laser pulses," *J. Lightwave Technol.* **21**, 246-253 (2003).
3. S. Nolte, M. Will, J. Burghoff, and A. Tuennermann, "Femtosecond waveguide writing: a new avenue to three-dimensional integrated optics," *Appl. Phys. A-Mater.* **77**, 109-111 (2003).
4. R. Osellame, S. Taccheo, M. Marangoni, R. Ramponi, P. Laporta, D. Polli, S. De Silvestri, and G. Cerullo, "Femtosecond writing of active optical waveguides with astigmatically shaped beams," *J. Opt. Soc. Am. B* **20**, 1559-1567 (2003).
5. C. B. Schaffer, A. Brodeur, J. F. Garcia, and E. Mazur, "Micromachining bulk glass by use of femtosecond laser pulses with nanojoule energy," *Opt. Lett.* **26**, 93-95 (2001).
6. G. Della Valle, R. Osellame, N. Chiodo, S. Taccheo, G. Cerullo, P. Laporta, A. Killi, U. Morgner, M. Lederer, and D. Kopf, "C-band waveguide amplifier produced by femtosecond laser writing," *Opt. Express* **13**, 5976-5982 (2005).
7. A. M. Kowalevich, V. Sharma, E. P. Ippen, J. G. Fujimoto, and K. Minoshima, "Three-dimensional photonic devices fabricated in glass by use of a femtosecond laser oscillator," *Opt. Lett.* **30**, 1060-1062 (2005).
8. K. Minoshima, A. M. Kowalevich, E. P. Ippen, and J. G. Fujimoto, "Fabrication of coupled mode photonic devices in glass by nonlinear femtosecond laser materials processing," *Opt. Express* **10**, 645-652 (2002).
9. Y. Sikorski, A. A. Said, P. Bado, R. Maynard, C. Florea, and K. A. Winick, "Optical waveguide amplifier in Nd-doped glass written with near-IR femtosecond laser pulses," *Electron. Lett.* **36**, 226-227 (2000).
10. A. M. Streltsov and N. F. Borrelli, "Fabrication and analysis of a directional coupler written in glass by nanojoule femtosecond laser pulses," *Opt. Lett.* **26**, 42-43 (2001).
11. S. Taccheo, G. Della Valle, R. Osellame, G. Cerullo, N. Chiodo, P. Laporta, O. Svelto, A. Killi, U. Morgner, M. Lederer, and D. Kopf, "Er : Yb-doped waveguide laser fabricated by femtosecond laser pulses," *Opt. Lett.* **29**, 2626-2628 (2004).
12. M. Born and E. Wolf, "Principles of Optics" (1980).
13. H. Dotsch, N. Bahlmann, O. Zhuromskyy, M. Hammer, L. Wilkens, R. Gerhardt, P. Hertel, and A. F. Popkov, "Applications of magneto-optical waveguides in integrated optics: review," *J. Opt. Soc. Am. B* **22**, 240-253 (2005).
14. M. Levy, H. Hegde, F. J. Cadieu, R. Wolfe, V. J. Fratello, and R. M. J. Osgood, "Integrated optical isolators with sputter-deposited thin-film magnets," *IEEE Photonic Technol. Lett.* **8**, 903-905 (1996).
15. M. Levy, I. Ilic, R. Scarmozzino, R. M. J. Osgood, R. Wolfe, C. J. Gutierrez, and G. A. Prinz, "Thin-film-magnet magnetooptic waveguide isolator," *IEEE Photonic. Tech. Lett.* **5**, 198-200 (1993).

16. M. Kamata, M. Obara, R. R. Gattass, L. R. Cerami, and E. Mazur, "Optical vibration sensor fabricated by femtosecond laser micromachining," *Appl. Phys. Lett.* **87**, 051106-051101-051103 (2005).
 17. R. Osellame, N. Chiodo, V. Maselli, A. Yin, M. Zavelani-Rossi, G. Cerullo, P. Laporta, L. Aiello, S. De Nicola, P. Ferraro, A. Finizio, and G. Pierattini, "Optical properties of waveguides written by a 26 MHz stretched cavity Ti : sapphire femtosecond oscillator," *Opt. Express* **13**, 612-620 (2005).
 18. H. Ebendorff-Heidepriem and D. Ehrh: "Effect of Tb³⁺ ions on X-ray induced defect formation in phosphate containing glasses," *Opt. Mater.* **18**, 419-422 (2002).
 19. H. Ebendorff-Heidepriem and D. Ehrh: "Electron spin resonance spectra of Eu²⁺ and Tb⁴⁺ ions in glasses" *J. Phys-Condens. Mat.* **11**, 7627-7629 (1999).
 20. J. Qiu, J. B. Qiu, H. Higuchi, Y. Kawamoto, and K. Hirao: "Faraday effect of GaS₃/2-GeS₂-LaS₃/2-based glasses containing various rare-earth ions" *J. Appl. Phys.* **80**, 5297-5300 (1996).
-

1. Introduction

Femtosecond laser micromachining of transparent materials has many potential applications in integrated optics [1-11]. Many devices such as waveguides [1-5], splitters [10], Mach-Zehnder interferometers [8], resonators [7] and amplifiers [6, 9, 11] have been fabricated using this technique. In this paper, we combine oscillator-only micromachining and an externally switchable substrate to fabricate integrated active waveguides. Oscillator-only micromachining of waveguides does not require an amplifier and the pairing of this technique with a material whose properties can be externally controlled enable the fabrication of waveguides that can serve as active optical logic devices for integrated circuits.

One externally controllable material property that can be exploited to make switchable active devices is the magneto-optic effect, also known as Faraday effect [12]. The Faraday effect is a rotation of the light-polarization induced by a magnetic field applied to the material. The linear constant of proportionality between the angle of rotation and the applied magnetic field is called the Verdet constant, and is given by $V = \theta / BL$, where θ is the relative angle of polarization rotation, B is the magnitude of the applied magnetic field parallel to the direction of light propagation, and L is the material length over which the magneto-optic interaction takes place. The higher the Verdet constant, the larger the polarization rotation in response to an applied magnetic field, and the more suitable the material is for optical switching. Faraday rotation is widely used in optical isolators, preventing feedback in optical circuits.

Previously fabricated Faraday rotating waveguides for integrated optics include rib waveguides etched from Garnet films deposited on semiconductors [13-15] and waveguides produced by laser annealing [13]. All these waveguide fabrication methods require the deposition of a film of magneto-optic material onto a suitable substrate, which is costly and time consuming. In contrast, the waveguides we present in this paper can be easily written into bulk transparent material using oscillator-only femtosecond-laser micromachining, and the magneto-optic material is bulk Faraday glass, for which no deposition or growth is necessary. Furthermore, previous work in our group has shown that we can micromachine waveguides across multiple pieces of glass while maintaining good optical coupling between them [16], enabling the fabrication of an integrated Faraday isolator using femtosecond micromachining.

We demonstrate that oscillator-only femtosecond-laser micromachining can be used to fabricate waveguides inside terbium-doped Faraday glass. The resultant waveguides are magneto-optically active, and can be used for photonic applications. The measured effective Verdet constant of the waveguide is $3600^\circ \pm 500^\circ \text{ T}^{-1}\text{m}^{-1}$ ($0.22 \pm 0.03 \text{ min/Oe}\cdot\text{cm}$), comparable to that of the original material, which is $4300^\circ \pm 200^\circ \text{ T}^{-1}\text{m}^{-1}$ ($0.26 \pm 0.01 \text{ min/Oe}\cdot\text{cm}$). We further investigated the compositional modification induced by femtosecond-laser micromachining by Electron Paramagnetic Resonance (EPR) spectra of the Faraday glass before and after irradiation. We observe a slight increase in the concentration of Tb⁺⁴ ions, which is not significant enough to affect the waveguide's Faraday behavior.

2. Experimental

In Faraday glass, one class of magneto-optically active materials, rare-earth ions are responsible for the material's magnetic susceptibility. The commercial Faraday glass used in

this experiment was purchased from Shanghai Institute of Optics and Fine Mechanics. The glass, known as TG20, is doped with Tb^{3+} ions and has a composition of $\text{Tb}_2\text{O}_3\text{-SiO}_2\text{-Al}_2\text{O}_3\text{-B}_2\text{O}_3$, with a homogenous Tb^{3+} ion concentration of 7.9×10^{18} ions/ mm^3 . The Faraday glass is micromachined using 60-fs, 800-nm, 10-nJ laser pulses from an extended cavity oscillator at a 25-MHz repetition rate. The pulses are focused through a 1.4-NA microscope objective (with a nearly spherical spot size of about 1 μm in diameter) into the bulk of a 50 mm \times 5 mm \times 1 mm Faraday glass sample that is translated at a speed of 10 mm/s with respect to the laser beam. The waveguides are each written in one pass along the entire 50-mm length of the sample, and are spaced by 200 μm to prevent crosstalk between waveguides, as seen in Fig. 1. The top left inset of Fig. 1 shows a cross-sectional view of the micromachined waveguides, which have an average diameter of 8 μm . After micromachining the ends of the sample are polished to allow light to be coupled into the waveguides. We found multimode behavior at 632 nm, as shown in the top right inset of Fig. 1, and single mode behavior at 1550 nm.

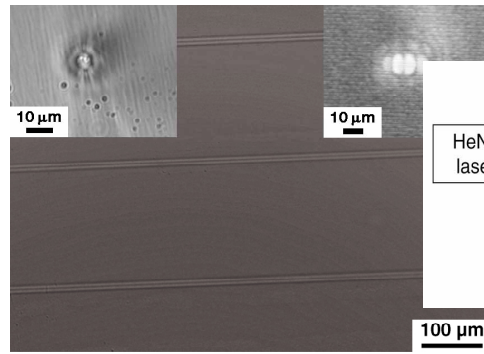


Fig. 1. Optical microscope image of micromachined waveguides inside the Faraday glass. Left Inset: Cross-sectional view of waveguide. Right Inset: Observed multimode behavior at 632 nm.

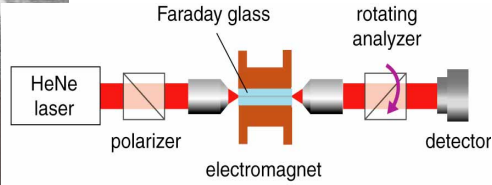


Fig. 2. Experimental setup for measuring Faraday rotation. A 632.8-nm laser beam is sent through a linear polarizer, coupled into and out of the sample using 10 \times microscope objectives, and finally analyzed by a rotating analyzer mounted on a motorized wheel.

We determined the magneto-optic response of the waveguides using the polarization rotation setup shown in Fig. 2. The micromachined Faraday sample is placed in an electromagnetic coil, which is mounted on a three-axis stage to facilitate alignment. HeNe laser light at 632.8 nm is coupled into and out of the waveguide using two 10 \times microscope objectives and an iris blocks any scattered light at the exit of the second objective lens. To determine the polarization rotation we use a rotating analyzer in front of the detector and a lock-in amplifier. The resulting signal is a sinusoidal function of the analyzer angle and any induced Faraday rotation inside the waveguide results in a phase shift of the detected sinusoidal signal.

As the field is not uniform across the length of the sample, the standard expression for the Faraday rotation has to be modified to account for the varying magnetic field profile, $B(x)$, along the length of the sample. Because the Faraday effect is a linear response of the material to the applied magnetic field, we can write

$$V = \frac{\theta}{\int_0^L B(x) dx} . \quad (1)$$

To determine the Verdet constant of the material, we plot the phase shift of the signal as a function of the integrated magnetic field profile; the slope of the data then gives the Verdet constant.

3. Results

Figure 1 shows a close up of the femtosecond laser micromachined waveguides spaced by 200 μm under transmission optical microscopy. The micromachined waveguides look similar to those fabricated in glass using this process [5, 8, 17].

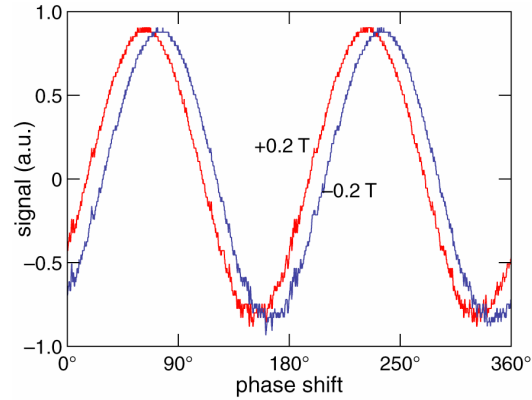


Fig. 3. Oscilloscope traces of the signal transmitted through the bulk Faraday glass for values of the integrated magnetic field profile of $\pm 0.2 \text{ T}\cdot\text{m}$. The observed phase shift gives the relative Faraday polarization rotation angle.

The dependence of the detector signal on the angle of the analyzer is shown in Fig. 3 for values of the integrated magnetic field profile of $\pm 0.2 \text{ T}\cdot\text{m}$. The phase shift between the two traces confirms that a Faraday rotation occurs inside the waveguide.

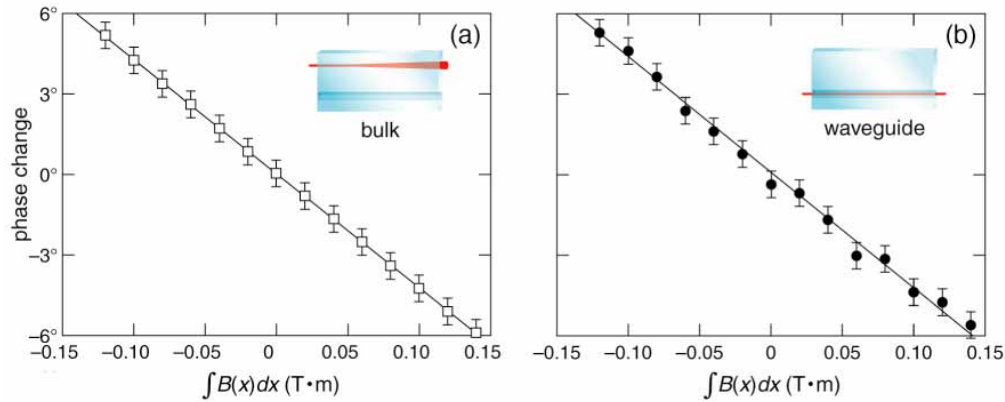


Fig. 4. Linear dependence of the induced phase change on the integrated magnetic field profile for (a) bulk Faraday glass and (b) a waveguide written in Faraday glass.

Figure 4(a) shows the dependence of the phase shift on the integrated magnetic field profile in bulk Faraday glass. In Fig. 4(b), we show the same data for the waveguide. The Verdet constant is the slope of a least-squares fit of the data to a straight line. Averaging several sets of data for both bulk glass and waveguides, we obtain an effective Verdet constant of $3600^\circ \pm 500^\circ \text{ T}^{-1}\text{m}^{-1}$ for the waveguides, which is a slight reduction in the Verdet

constant compared to that of the bulk Faraday glass ($4300^\circ \pm 200^\circ \text{ T}^{-1}\text{m}^{-1}$) to within the experimental error.

4. Discussion

Previous research [18, 19] has shown that UV irradiation can oxidize Tb^{3+} ions in Faraday glass into paramagnetic Tb^{4+} ions. Because our femtosecond micromachining technique relies on multiphoton absorption in the focal volume and because simultaneous absorption of three photons provides the same energy as a UV photon, it is possible that during micromachining Tb^{3+} ions are ionized into Tb^{4+} ions.

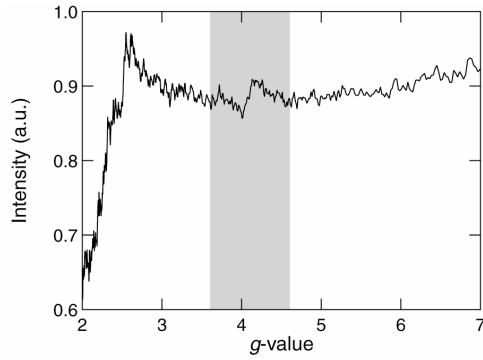


Fig. 5. Electron Paramagnetic Resonance spectrum of bulk Faraday glass. The shaded region shows the paramagnetic resonance due to the Tb^{4+} ions.

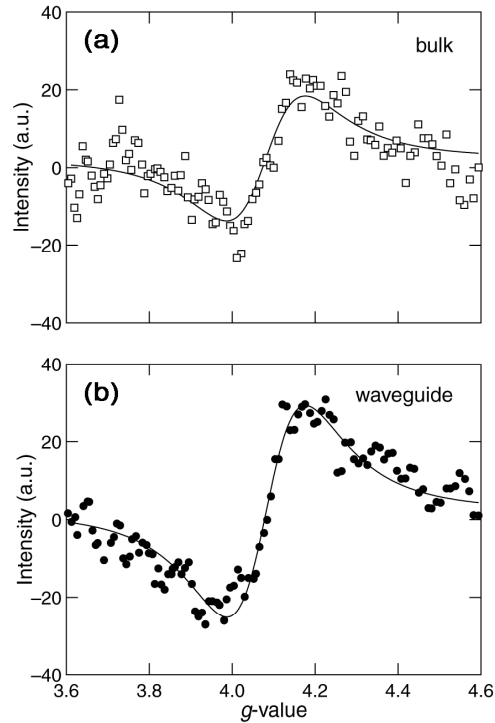


Fig. 6. Paramagnetic resonance due to the Tb^{4+} ions in the Electron Paramagnetic Resonance spectrum of Faraday glass (a) before and (b) after irradiation with femtosecond laser pulses. The curves show a Lorentzian fit to the data.

Because the terbium ions are responsible for the Faraday effect [20], we examined how femtosecond micromachining affects the concentration of Tb^{4+} ions using EPR spectroscopy. Figure 5 shows the EPR spectrum of the bulk Faraday glass. The highlighted region shows the resonant signature of the paramagnetic Tb^{4+} ions at a gyromagnetic ratio value of $g = 4.1$; this region is shown in greater detail in Fig. 6(a). The amplitude of the resonance is a measure of the ion concentration. For comparison, an additional sample was prepared by micromachining waveguides spaced $25 \mu\text{m}$ apart across the length of a piece of Faraday glass, irradiating approximately 2% of the sample's volume before grinding it up and obtaining an EPR spectrum [Fig. 6(b)]. Fitting both spectra in Fig. 6 with a Lorentzian curve, we find a 60% increase in the Tb^{4+} spectral intensity after laser micromachining, indicating that Tb^{4+} ions are generated during the waveguide writing process. Using a theoretical model and accounting for

the percentage irradiated, [20] we estimate that there are a total of $5.5 \times 10^{19} \text{ cm}^{-3} \text{ Tb}^{4+}$ ions after femtosecond-laser irradiation [20]. This resulting Tb^{4+} ion concentration is still negligible compared to the initial Tb^{3+} ion concentration of $7.9 \times 10^{21} \text{ cm}^{-3}$, confirming that the micromachining process does not affect the ions responsible for the Faraday effect.

5. Conclusion

In summary, we demonstrate that it is possible to fabricate waveguides in Faraday materials using femtosecond micromachining. The fabricated waveguides exhibit no significant reduction in Verdet constant and the micromachined waveguides can be used as magneto-optic switches. We confirmed that the femtosecond-laser micromachining does not convert a significant fraction of the active Tb^{3+} ions into Tb^{4+} ions. These findings pave the way for light-by-light magneto-optic switching and integrated optical isolators.

Acknowledgments

The authors would like to acknowledge B. Tull and I. Maxwell for their help editing the manuscript. R. Gattass provided the idea for this experiments and assisted T. Shih in carrying out the experiments. C.R. Mendonca helped with the acquisition and analysis of the experimental data. T. Shih acknowledges financial support from an NSF Graduate Research Fellowship and C. R. Mendonca acknowledges financial support from the Fundação de Amparo a Pesquisa do Estado de São Paulo. The research described in this paper was supported by the NSF under contracts DMI-0334984 and ARO-W911NF-05-1-0471.

C.R. MENDONCA^{1,2,✉}
D.S. CORREA¹
T. BALDACCHINI²
P. TAYALIA²
E. MAZUR²

Two-photon absorption spectrum of the photoinitiator Lucirin TPO-L

¹ Instituto de Física de São Carlos, Universidade de São Paulo, Caixa Postal 369, 13560-970 São Carlos, SP, Brazil

² Department of Physics and Harvard School of Engineering and Applied Sciences, Harvard University, 9 Oxford Street, Cambridge, MA 02138, USA

Received: 17 November 2007 / Accepted: 19 November 2007
Published online: 29 December 2007 • © Springer-Verlag 2007

ABSTRACT Two-photon absorption induced polymerization provides a powerful method for the fabrication of intricate three-dimensional microstructures. Recently, Lucirin TPO-L was shown to be a photoinitiator with several advantageous properties for two-photon induced polymerization. Here we measure the two-photon absorption cross-section spectrum of Lucirin TPO-L, which presents a maximum of 1.2 GM at 610 nm. Despite its small two-photon absorption cross-section, it is possible to fabricate excellent microstructures by two-photon polymerization due to the high polymerization quantum yield of Lucirin TPO-L. These results indicate that optimization of the two-photon absorption cross-section is not the only material parameter to be considered when searching for new photoinitiators for microfabrication via two-photon absorption.

PACS 42.65.-k; 78.40.Me; 42.70.Jk; 81.05.Lg

1 Introduction

Two-photon absorption processes have attracted much interest due to their potential applications in optical sciences, biology and microfabrication technologies. The quadratic dependence of the two-photon absorption rate on laser intensity allows spatial confinement of the excitation, a feature exploited in three-dimensional optical storage [1–4], two-photon fluorescence imaging [5, 6], two-photon photodynamic therapy [7, 8], and microfabrication via two-photon induced polymerization [9–11]. Two-photon initiated polymerization in particular is a very interesting tool to fabricate sophisticated microstructures for optical circuitry [12], optical data storage [13], three-dimensional micromechanical actuators [14–16] and photonic crystals [13, 17].

In general, photopolymerization of mixtures of monomers and oligomers requires a photoinitiator, many of which are commercially available. Although new photoinitiators with higher two-photon absorption cross-sections, a key parameter for two-photon polymerization, have been de-

signed in the last five years [13, 18], these molecules are still not readily available. To determine the optimal conditions for two-photon polymerization, the two-photon absorption cross-sections of some conventional commercial photoinitiators have been measured [19]. Lucirin TPO-L (ethyl-2,4,6-trimethylbenzoylphenylphosphine), an acylphosphine oxide radical photoinitiator whose molecular structure is shown in Fig. 1, was demonstrated to be an efficient initiator of polymerization under two-photon excitation [20]. Furthermore, unlike most radical photoinitiators, Lucirin TPO-L is a liquid with broad solubility that can be mixed easily with most resin formulations.

In this paper we present the degenerate two-photon absorption cross-section spectrum of Lucirin TPO-L and interpret this spectrum with the aid of quantum chemistry calculations. Although the two-photon absorption cross-section of Lucirin TPO-L is small (< 1.2 GM), we can microfabricate structures with high integrity and definition using moderate laser powers (10 mW), due to the high polymerization efficiency of Lucirin TPO-L (radical quantum yield of 0.99). The high polymerization efficiency makes Lucirin TPO-L an excellent photoinitiator for microfabrication via two-photon absorption polymerization over a large spectral range in the visible/infrared.

2 Experimental

We prepared Lucirin TPO-L/ethanol solution with concentrations of 7×10^{-3} and $9 \times 10^{-1} \text{ mol L}^{-1}$, for linear and nonlinear optical measurements, respectively. The samples were placed in 2 mm thick quartz cuvettes for spectroscopic measurements. The linear absorption spectrum was recorded using a spectrophotometer equipped with an inte-

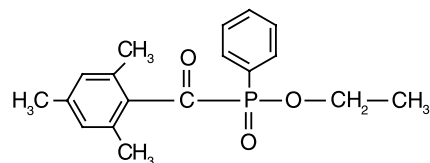


FIGURE 1 Molecular structure of lucirin TPOL-L

grating sphere detector. The two-photon absorption spectrum was obtained using the Z-scan technique [21].

In the Z-scan technique, the two-photon absorption cross section is determined by moving the sample through the focal plane of a focused Gaussian beam and monitoring the changes in the far field intensity. For a two-photon absorption process, the light field creates an intensity dependent absorption, $\alpha = \alpha_0 + \beta I$, where I is the laser beam intensity, α_0 is the linear absorption coefficient and β the two-photon absorption coefficient. For non-resonant conditions, such as two-photon absorption, the change in the transmitted power is integrated over time (assuming a pulse with a Gaussian temporal profile) to give the normalized energy transmittance [21],

$$T = \frac{1}{\sqrt{\pi} q_0(z, 0)} \int_{-\infty}^{\infty} \ln [1 + q_0(z, 0) e^{-\tau^2}] d\tau, \quad (1)$$

where $q_0(z, t) = \beta I_0(t) L (1 + z^2/z_0^2)^{-1}$, L is the sample thickness, z_0 the Rayleigh length, z the sample position and I_0 the laser intensity.

The nonlinear coefficient β is obtained by fitting (1) to the Z-scan data [21] with β as a free parameter. The two-photon absorption cross-section, δ , is determined from $\delta = h\nu\beta/N$, where $h\nu$ is the excitation photon energy and N is the number of molecules per cm^3 . Usually the two-photon absorption cross-section δ is expressed in units of Göppert-Mayer (GM), where $1 \text{ GM} = 1 \times 10^{-50} \text{ cm}^4 \text{ s mol}^{-1} \text{ photon}^{-1}$.

For the Z-scan experiment we used a 150 fs, 775 nm and 1 kHz Ti:sapphire laser as the pump for an optical parametric amplifier, which delivers 120 fs pulses with wavelengths ranging from 600 to 810 nm. The output beam of the optical parametric amplifier is spatially filtered to produce a Gaussian beam profile. The transmitted signal through the sample is measured using a silicon photo-detector coupled to a lock-in amplifier. To further improve the sensitivity of the Z-scan technique we used the fastscan Z-scan method, [22] which averages Z-scan traces while the sample is oscillated through the focal plane, allowing the measurement of transmittance changes of only a few percent. In order to avoid photodegradation during the Z-scan, besides using relatively small irradiances, we performed the measurements in a flow cell geometry.

The resin used in this work consists of a mixture of two tri-acrylate monomers and Lucirin TPO-L as photoinitiator. Tris(2-hydroxyethyl)isocyanurate triacrylate (monomer A) increases the microstructure hardness, while ethoxylated(6) trimethylolpropane triacrylate (monomer B) reduces shrinkage upon polymerization [20].

To fabricate microstructures we used a 130 fs, 800 nm Ti:sapphire laser oscillator beam focused into the sample with a 0.65 NA microscope objective. We used an average laser power of 10 mW measured after the objective. The sample consists of a drop of resin placed inside a spacer located on top of a microscope slide whose surface is treated with (3 acryloxypropyl)trimethoxysilane to increase adhesion of the final structure to the glass substrate. The resin is contained inside the spacer by a cover slip. The sample is positioned in the axial z -direction using a motorized stage, and the laser is scanned across the resin in the xy direction using a pair of galvano mir-

rors. After the desired microstructure is fabricated, the sample is immersed in ethanol to wash away the unsolidified resin.

3 Results

Figure 2 shows a Z-scan curve [21] for Lucirin TPO-L, for an off-resonance pump wavelength of 610 nm. The decrease in the normalized transmittance at the focal point $z = 0$ is due to two-photon absorption. By fitting (1) to the experimental data (solid line) we obtain a value for the two-photon absorption cross-section δ . The value we obtain for δ is independent of the incident laser intensity, as one would expect for a pure two-photon absorption process.

Figure 3 shows the linear absorption spectrum of Lucirin TPO-L as a solid line and the values of δ (circles) obtained from Z-scan measurements at different excitation wavelengths. The linear absorption increases towards shorter wavelengths and displays a peak around 365 nm. The spectrum shows that Lucirin TPO-L does not exhibit any linear absorption beyond 440 nm; it is completely transparent at the near-infrared wavelength used in the Z-scans experiments and

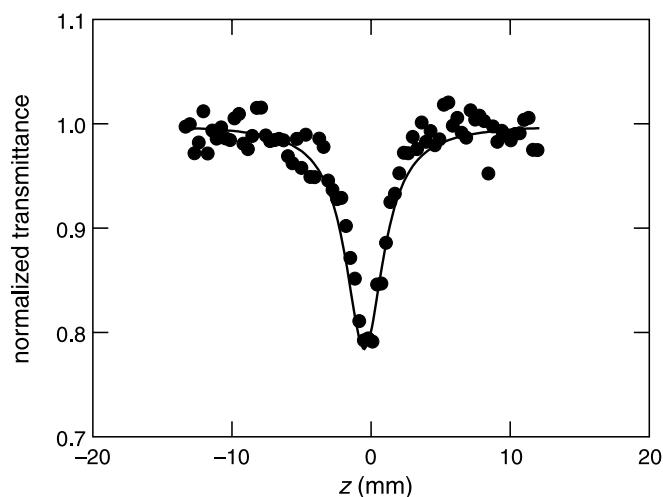


FIGURE 2 Z-scan curve at 610 nm for lucirin TPO-L (circles), using an intensity of approximately 2 GW/mm^2 . The curve represents a fit of Eq. (1) to the data

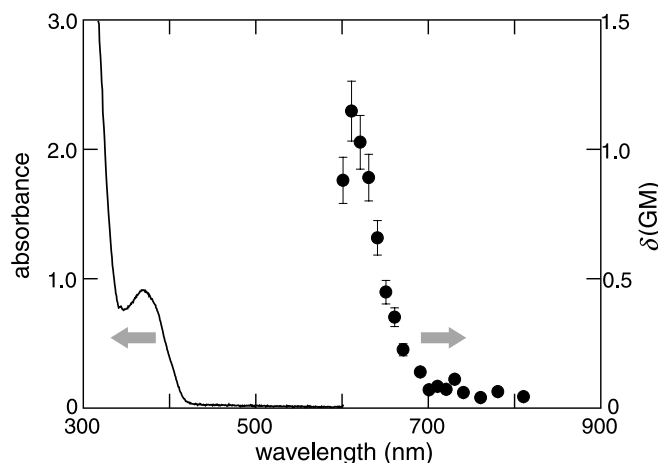


FIGURE 3 Linear absorption spectrum (curve; left axis) and two-photon absorption cross-section spectrum (circles; right axis) of lucirin TPO-L

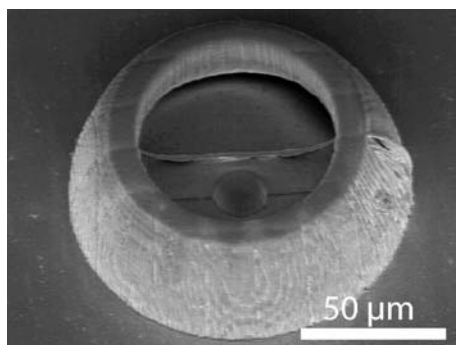


FIGURE 4 Scanning electron micrograph of microstructures fabricated by two-photon absorption polymerization; 30° tilted view of a hemispherical structure

the two-photon polymerization microfabrication. The two-photon absorption spectrum, on the other hand, has a large peak at 610 nm and a second, much smaller peak at 730 nm.

Figure 4 shows a scanning electron micrograph of a three-dimensional microstructure fabricated in the acrylate-based resin using Lucirin TPO-L as a photoinitiator for the two-photon polymerization at 800 nm. It should be pointed out that the two-photon absorption cross-section at this wavelength is very small, as seen in Fig. 3. The fabricated microstructure is an open hemisphere containing a smaller hemisphere that is divided by a plane. Microstructures fabricated in this way have high definition and excellent integrity, indicating that Lucirin TPO-L efficiently induces photopolymerization via two-photon absorption.

4 Discussion

The peak in the two-photon absorption spectrum at 610 nm (Fig. 3, circles) corresponds to a two-photon transition to the band located around 300 nm in the linear absorption spectrum (Fig. 3, curve). The value of the two-photon absorption peak (1.2 GM) is comparable with results obtained for other photoinitiators [19]. The small two-photon absorption peak at 730 nm corresponds to twice the wavelength of the one-photon absorption peak at 365 nm. For symmetric molecules, one-photon allowed transitions are two-photon forbidden [23–26]. However, Lucirin TPO-L has an asymmetric molecular geometry (Fig. 1), and so we can expect these selection rules to be relaxed. Indeed, as evidenced by the correspondence between the peaks in the two-photon and linear absorption spectra in Fig. 3, two-photon transitions can reach the same final state as one-photon transitions.

To explain the small two-photon absorption cross-section values observed in Fig. 3 we determined the molecular geometry of Lucirin TPO-L and the frontier molecular orbitals. Figure 5a shows the molecular geometry of Lucirin TPO-L obtained via *ab initio* (6–31 G*) calculations. Due to the presence of the phosphorus atom the molecule has a nonplanar structure. The lowest unoccupied and highest occupied molecular orbitals, shown in Fig. 5b and c, respectively, were obtained using the semi-empirical ZINDO/1 method [27, 28]. The orbitals indicate that Lucirin TPO-L does not have a high conjugation length with most of the charge localized in the central portion of the molecule. A high two-photon

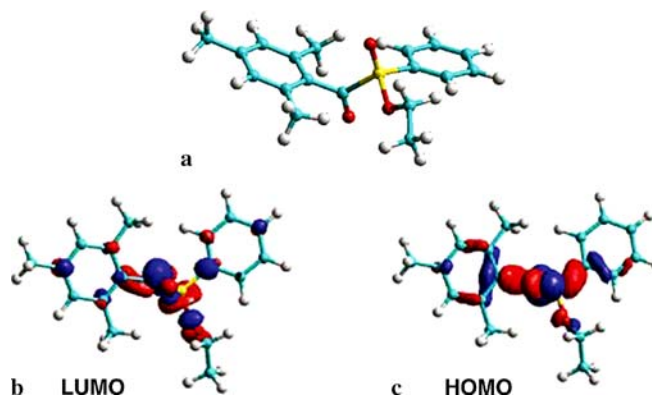


FIGURE 5 (a) Molecular geometry of the lucirin TPO-L molecule obtained from *ab initio* calculations. (b) Lowest unoccupied molecular orbital and (c) highest occupied molecular orbital obtained using the semi-empirical ZINDO/1 method

cross section requires high conjugation and molecular planarity [29, 30], both of which are absent in Lucirin TPO-L, which explains the small two-photon absorption cross-section of this photoinitiator.

In spite of the small two-photon absorption cross-section, Lucirin TPO-L has been recently shown to be an effective photoinitiator [20]. The polymerization action spectrum, which is proportional to the product of the two-photon absorption cross section $\delta(\omega)$ and the radical quantum yield $\phi_2(\omega)$, contains a peak around 725 nm [20]. The authors attribute this peak to a corresponding peak in the two-photon absorption spectrum and estimate the radical quantum yield to be 0.99 at 800 nm. Our measurements of the two-photon absorption spectrum $\delta(\omega)$ in Fig. 3 confirm this conclusion: we directly observed a peak in $\delta(\omega)$ at 730 nm and the two-photon cross-section is small, indicating that the radical quantum yield must be high. It is this high radical quantum yield that makes Lucirin TPO-L an effective photoinitiator.

Lucirin TPO-L generates radicals when it is excited to the triplet state [31]. Due to the two-photon excitation puts the molecule in a singlet state, the high radical quantum yield must therefore be due to an efficient singlet–triplet conversion. Indeed, the low fluorescence quantum yield of Lucirin TPO-L [31] suggests a high singlet–triplet conversion efficiency. This high efficiency can be attributed to the presence of the phosphorous atom in the molecule, which enhances the spin–orbit coupling, increasing the intersystem crossing rate [32].

Although photoinitiators with much higher two-photon absorption cross-sections [13, 18] are available, our results point out that initiators with small two-photon absorption cross-sections are also suitable for the fabrication of microstructures as long as they have a high radical quantum yield, in agreement with other results already reported for other initiators [18, 33–35].

5 Conclusion

We measured the two-photon absorption cross-section spectrum of Lucirin T-POL in the wavelength range from 600 to 810 nm using the Z-scan technique. The maximum value of two-photon absorption cross-section is

1.2 GM, which is low compared to some organic molecules [30, 36, 37], but comparable to other photoinitiators reported in the literature [19]. Using quantum-chemical calculations we established that the low nonlinear optical properties of this molecule arise from its nonplanarity and low conjugation length. Despite the small two-photon absorption cross-section exhibited by Lucirin TPO-L, its high polymerization quantum yield permits the fabrication of microstructures with excellent structural integrity and definition, demonstrating the potential of Lucirin TPO-L for microfabrication by two-photon polymerization.

ACKNOWLEDGEMENTS Several people contributed to the work described in this paper. C.R. Mendonca and T. Baldacchini conceived the basic idea for this work and designed the experiment. C.R. Mendonca, D.S. Correa, T. Baldacchini and P. Tayalia carried out the experiments. E. Mazur supervised the research and contributed to the development of the manuscript. C.R. Mendonca wrote the first draft of the manuscript; all authors subsequently took part in the revision process. Rafael Gattass and Tobias Voss provided feedback on the manuscript throughout its development. The research described in this paper was supported by National Science Foundation under contract DMI 0334984, the Army Research Office under contract ARO W911NF-05-1-0471. Cleber Mendonca acknowledges support from Fundação de Amparo a Pesquisa do Estado de São Paulo (FAPESP) and Coordenação de Aperfeiçoamento de Pessoal de Nível Superior (CAPES) from Brazil during his stay at Harvard University. The authors would also like to acknowledge the use of facilities of the Center for Nanoscale Systems, which is supported by the National Science Foundation's National Nanotechnology Infrastructure Network.

REFERENCES

- 1 S. Kawata, Y. Kawata, *Chem. Rev.* **100**, 1777 (2000)
- 2 A.S. Dvornikov, P.M. Rentzepis, *Opt. Commun.* **119**, 341 (1995)
- 3 D.A. Parthenopoulos, P.M. Rentzepis, *J. Appl. Phys.* **68**, 5814 (1990)
- 4 D.A. Parthenopoulos, P.M. Rentzepis, *Science* **245**, 843 (1989)
- 5 C. Xu, W. Zipfel, J.B. Shear, R.M. Williams, W.W. Webb, *Proc. Nat. Acad. Sci. USA* **93**, 10763 (1996)
- 6 P.T.C. So, C.Y. Dong, B.R. Masters, K.M. Berland, *Ann. Rev. Biomed. Eng.* **2**, 399 (2000)
- 7 J.D. Bhawalkar, G.S. He, P.N. Prasad, *Rep. Prog. Phys.* **59**, 1041 (1996)
- 8 T.J. Dougherty, B.W. Henderson, S. Schwartz, J.W. Winkelman, R.L. Lipson, In: *Photodynamic Therapy*, ed. by B.W. Henderson, T.J. Dougherty (Marcel Dekker, New York, 1992), p. 1
- 9 S. Kawata, H.B. Sun, T. Tanaka, K. Takada, *Nature* **412**, 697 (2001)
- 10 H.B. Sun, S. Kawata, *Nmr – 3d Analysis – Photopolymerization* (Springer, Berlin, 2004), p. 169
- 11 M. Miwa, S. Juodkazis, T. Kawakami, S. Matsuo, H. Misawa, *Appl. Phys. A* **73**, 561 (2001)
- 12 M.P. Joshi, H.E. Pudavar, J. Swiatkiewicz, P.N. Prasad, B.A. Reianhardt, *Appl. Phys. Lett.* **74**, 170 (1999)
- 13 B.H. Cumpston, S.P. Ananthavel, S. Barlow, D.L. Dyer, J.E. Ehrlich, L.L. Erskine, A.A. Heikal, S.M. Kuebler, I.Y.S. Lee, D. McCord-Maughon, J.Q. Qin, H. Rockel, M. Rumi, X.L. Wu, S.R. Marder, J.W. Perry, *Nature* **398**, 51 (1999)
- 14 P. Galajda, P. Ormos, *Appl. Phys. Lett.* **78**, 249 (2001)
- 15 T. Watanabe, M. Akiyama, K. Totani, S.M. Kuebler, F. Stellacci, W. Wenseleers, K. Braun, S.R. Marder, J.W. Perry, *Adv. Funct. Mater.* **12**, 611 (2002)
- 16 Z. Bayindir, Y. Sun, M.J. Naughton, C.N. LaFratta, T. Baldacchini, J.T. Fourkas, J. Stewart, B.E.A. Saleh, M.C. Teich, *Appl. Phys. Lett.* **86**, 064105 (2005)
- 17 J. Serbin, A. Ovsianikov, B. Chichkov, *Opt. Express* **12**, 5221 (2004)
- 18 S.M. Kuebler, K.L. Braun, W.H. Zhou, J.K. Cammack, T.Y. Yu, C.K. Ober, S.R. Marder, J.W. Perry, *J. Photochem. Photobiol. A* **158**, 163 (2003)
- 19 K.J. Schafer, J.M. Hales, M. Balu, K.D. Belfield, E.W. Van Stryland, D.J. Hagan, *J. Photochem. Photobiol. A* **162**, 497 (2004)
- 20 T. Baldacchini, C.N. LaFratta, R.A. Farrer, M.C. Teich, B.E.A. Saleh, M.J. Naughton, J.T. Fourkas, *J. Appl. Phys.* **95**, 6072 (2004)
- 21 M. Sheik-Bahae, A.A. Said, T.H. Wei, D.J. Hagan, E.W. Van Stryland, *IEEE J. Quantum Electron.* **QE-26**, 760 (1990)
- 22 I.J. Blewett, J. Stokes, A. Tookey, A.K. Kar, B.S. Wherrett, *Opt. Laser Technol.* **29**, 355 (1997)
- 23 R.R. Birge, B. Parsons, Q.W. Song, J.R. Tallent, In: *Molecular Electronics*, ed. by J. Jortner, M. Ratner (Blackwell Science, London, 1997)
- 24 W.L. Peticola, *Ann. Rev. Phys. Chem.* **18**, 233 (1967)
- 25 L. Antonov, K. Kamada, K. Ohta, F.S. Kamounah, *Phys. Chem. Chem. Phys.* **5**, 1193 (2003)
- 26 D.P. Craig, T. Thirunamachandran, *Molecular Quantum Electrodynamics – An Introduction to Radiation Molecule Interaction* (Dover Publications, New York, 1998)
- 27 M.J.S. Dewar, E.G. Zoebisch, E.F. Healy, J.J.P. Stewart, *J. Am. Chem. Soc.* **107**, 3902 (1985)
- 28 J. Ridley, M. Zerner, *Theoret. Chim. Acta* **32**, 111 (1973)
- 29 J.W. Perry, M. Albota, S. Ananthavel, D. Beljonne, J.L. Bredas, B. Cumpston, D.L. Dyer, J.E. Ehrlich, A.A. Heikal, S.E. Hess, T. Kogej, S.M. Kuebler, I.Y.S. Lee, M.D. Levin, S.R. Marder, D. McCord-Maughon, H. Rockel, M. Rumi, G. Subramanian, W.W. Webb, X.L. Wu, C. Xu, *Abstr. Pap. Am. Chem. Soc.* **217**, U378 (1999)
- 30 M. Albota, D. Beljone, J.L. Breda, J.E. Ehrlich, J.Y. Fu, A.A. Heikal, S.E. Hess, T. Kogej, M.D. Levin, S. Marder, D. McCord-Maughon, J.W. Perry, H. Rockel, M. Rumi, G. Subramanian, W.W. Webb, X.L. Wu, C. Xu, *Science* **281**, 1653 (1998)
- 31 C.S. Colley, D.C. Grills, N.A. Besley, S. Jockusch, P. Matousek, A.W. Parker, M. Towrie, N.J. Turro, P.M.W. Gill, M.W. George, *J. Am. Chem. Soc.* **124**, 14952 (2002)
- 32 N.J. Turro, *Modern Molecular Photochemistry* (University Science Books, Sausalito, 1991)
- 33 K.D. Belfield, K.J. Schafer, Y.U. Liu, J. Liu, X.B. Ren, E.W. Van Stryland, *J. Phys. Organ. Chem.* **13**, 837 (2000)
- 34 W.H. Zhou, S.M. Kuebler, K.L. Braun, T.Y. Yu, J.K. Cammack, C.K. Ober, J.W. Perry, S.R. Marder, *Science* **296**, 1106 (2002)
- 35 C. Martineau, R. Anemian, C. Andraud, I. Wang, M. Bouriau, P.L. Baldeck, *Chem. Phys. Lett.* **362**, 291 (2002)
- 36 A. Bhaskar, G. Ramakrishna, Z.K. Lu, R. Twieg, J.M. Hales, D.J. Hagan, E. Van Stryland, T. Goodson, *J. Am. Chem. Soc.* **128**, 11840 (2006)
- 37 S.L. Oliveira, D.S. Correa, L. Misoguti, C.J.L. Constantino, R.F. Aroca, S.C. Zilio, C.R. Mendonca, *Adv. Mater.* **17**, 1890 (2005)

Femtosecond laser micromachining in the conjugated polymer MEH–PPV

C.R. Mendonca^{a,b}, S. Orlando^{a,c}, G. Cosendey^a,
M. Winkler^a, E. Mazur^{a,*}

^a School of Engineering and Applied Science and Department of Physics, Harvard University, 9 Oxford Street, 02138-Cambridge, Massachusetts, USA

^b Instituto de Física de São Carlos, Universidade de São Paulo, Caixa Postal 369, 13560-970 São Carlos, SP, Brazil

^c CNR-Istituto di Metodologie Inorganiche e dei Plasm, Sezione di Potenza, Zona Industriale, I-85050 Tito Scalco, PZ, Italy

Received 19 May 2007; received in revised form 25 June 2007; accepted 31 July 2007

Available online 9 August 2007

Abstract

Femtosecond-laser micromachining of poly[2-methoxy-5-(2'-ethylhexyloxy)-*p*-phenylene vinylene] films is investigated using 130 fs pulses at 800 nm from a laser oscillator operating at 76 MHz repetition rate. We investigate the effect of pulse energy and translation speed on the depth and morphology of the micromachined regions. We quantified the MEH–PPV photobleaching induced by the fs-laser, and the conditions in which the emission of MEH–PPV is preserved after the micromachining.

© 2007 Elsevier B.V. All rights reserved.

Keywords: Micromachining; Femtosecond laser; Conjugated polymer

1. Introduction

Polymeric materials are promising candidates for fabricating micro- and nano-photonics devices in optical communications and sensing [1–5]. Several methods exist to structure polymeric materials in an inexpensive and reproducible manner, but most of these methods—standard photolithography, electron beam writing, or photopatterning in photosensitive polymers [6–11]—are limited to structuring surfaces. Femtosecond laser micromachining has received considerable attention due to its precision and ability to structure in three-dimensions.

When femtosecond laser pulses are focused into a material, the light intensity at the focal volume is sufficient to induce multi-photon absorption, leading to permanent structural changes in the material [12,13]. Such changes can be used to fabricate devices; for example, modification of the refractive

index enables the direct integration of photonic devices in three-dimensions [14,15]. Several studies have been reported on the micromachining of polymers, most of them transparent, with laser light, exploiting fundamental aspects of the micromachining process as well as devices fabrication [1–3,5,16–19].

In this paper, we investigate femtosecond laser micromachining in poly[2-methoxy-5-(2'-ethylhexyloxy)-*p*-phenylene vinylene] (MEH–PPV)[20], whose chemical structure is presented in Fig. 1. MEH–PPV is a conjugated polymer with photo- and electro-luminescent properties desirable for fabricating optoelectronic devices such as organic light-emitting diodes, chemical sensors, semiconductors and flexible displays [21,22].

We studied the influence of pulse energy and translation speed on MEH–PPV micromachining using optical and atomic force microscopy. We determined the energy threshold for polymer removal, and distinguished polymer removal from surface modification or photobleaching. We quantified polymer photobleaching during microfabrication via measurements of the absorption spectrum before and after laser irradiation. Finally, fluorescence microscopy of the microstructures reveals that the characteristic MEH–PPV emission persists after fabrication under appropriate micromachining conditions.

* Corresponding author at: School of Engineering and Applied Science and Department of Physics, Harvard University, 9 Oxford Street, 02138-Cambridge, Massachusetts, USA. Tel.: +1 617 495 9616; fax: +1 617 496 4654.

E-mail address: mazur@physics.harvard.edu (E. Mazur).

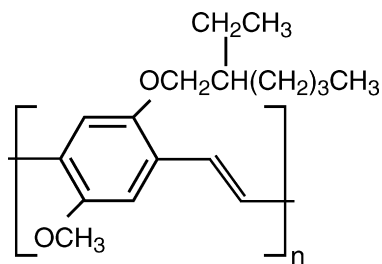


Fig. 1. Chemical structure of MEH-PPV.

2. Experimental

MEH-PPV was dissolved in chloroform with a concentration of 5 mg/ml. This solution was spin-coated on a glass substrate at 700 rpm, yielding films with thicknesses of approximately 350 nm. The films were stored at room temperature and protected from light to avoid photodegradation.

The MEH-PPV films were micromachined using 130 fs, 800 nm laser pulses from an oscillator at a 76 MHz repetition rate. The pulses were focused through 0.65 NA microscope objective onto the sample surface, which was translated at a constant speed with respect to the laser beam. The speed was maintained by a computer controlled translation stage.

The micromachined samples were analyzed by atomic force microscopy (Asylum Research MFP-3D), transmission optical microscopy (Nikon Eclipse ME600L), and fluorescence microscopy (Nikon Eclipse TE2000-E). To evaluate the optical properties of the samples, we measured their UV and visible absorbance with a spectrophotometer.

3. Results

Fig. 2 shows optical microscope images of microstructures produced in MEH-PPV at a translation speed of 20 $\mu\text{m/s}$ and various pulse energies. The transmission of visible light by the micromachined lines clearly increases with the pulse energy. At an energy of 0.07 nJ, the smallest pulse energy employed, little contrast is obtained, whereas at higher pulse energies a much higher contrast is observed (cf. Fig. 2a and d). The widths of the microstructured lines varies from 2 to 4 μm when the pulse energy is increased from 0.07 to 2.4 nJ. For a translation

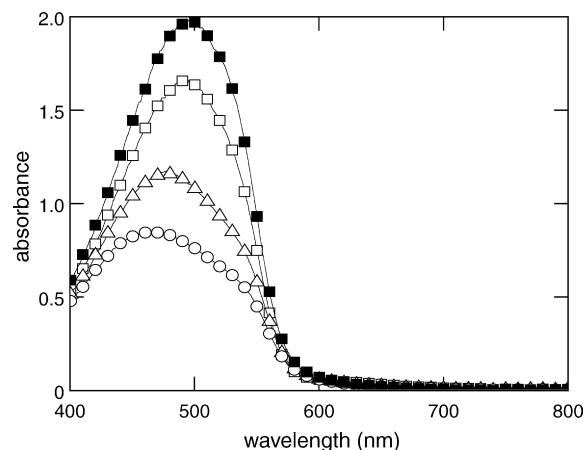


Fig. 3. Absorbance spectra for a MEH-PPV films not irradiated (solid squares), and after irradiation with 0.27 nJ (open squares), 0.55 nJ (open triangles) and 0.89 nJ (open circles) laser pulses.

speed of 20 $\mu\text{m/s}$, the threshold energy for inducing visible modification in the MEH-PPV sample was measured to be 0.05 nJ.

To evaluate the optical properties of the micromachined samples, we measured the absorbance of 3 mm \times 3 mm areas, fabricated at various pulse energies with a translation speed of 20 $\mu\text{m/s}$. Fig. 3 (open symbols) shows the absorption spectra of such areas. For comparison, the solid squares in Fig. 3 show the absorption spectrum of a sample that has not been irradiated. The absorption band around 500 nm, which corresponds to the $\pi \rightarrow \pi^*$ electronic transition of MEH-PPV [21], decreases with the pulse energy used for the micromachining. This decrease indicates that the MEH-PPV photobleaches during the micromachining.

In order to determine the effect of the laser pulse energy on the depth and morphology of the micromachining, we micromachined a set of lines for pulse energies ranging from 0.07 to 2.4 nJ and a fixed translation speed of 20 $\mu\text{m/s}$. Fig. 4 shows two representative atomic force micrographs of grooves machined at pulse energies of 0.3 and 2.0 nJ. The depths of the grooves were determined from the atomic force micrographs, and are plotted as a function of pulse energy in Fig. 5.

As seen in Fig. 5, there are two distinct regimes for the depths of the grooves as a function of pulse energy. For energies

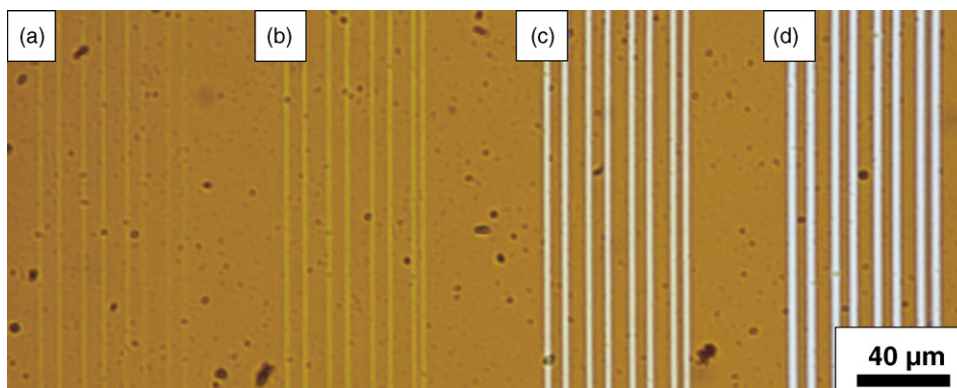


Fig. 2. Transmission optical microcopy of lines micromachined in MEH-PPV with pulse energies of (a) 0.07 nJ, (b) 0.14 nJ, (c) 0.34 nJ and (d) 0.68 nJ.

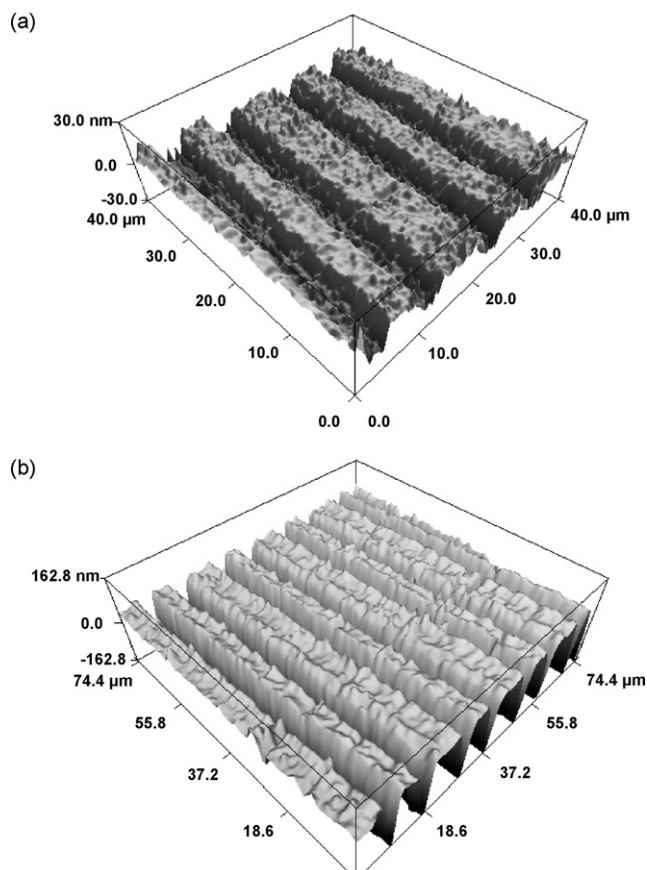


Fig. 4. Atomic force micrograph of grooves micromachined in the MEH-PPV films with (a) 0.3 nJ and (b) 2.0 nJ laser pulses.

up to 1 nJ, the groove depths varies from 7 to 30 nm, indicating only slight material removal from the polymer surface. For energies higher than 1.4 nJ, however, the groove depth becomes comparable to the 240 nm films thickness. The mid-point between the two regimes observed in Fig. 5 at 1.2 nJ defines the threshold between slight surface removal and material ablation.

From the atomic force micrographs (Fig. 4) we also observed an increase in the average surface roughness of the

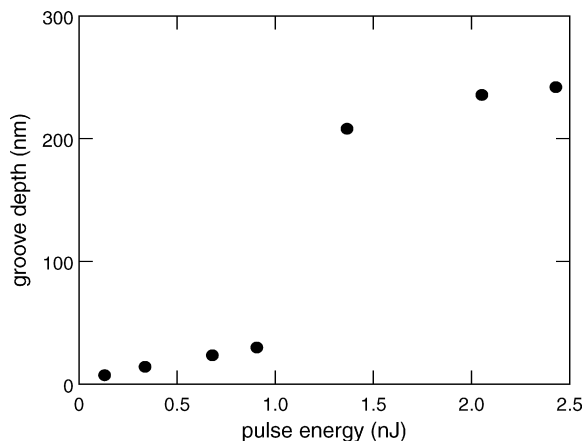


Fig. 5. Depth of the grooves as a function of the pulse energy for a translation speed of 20 $\mu\text{m/s}$.

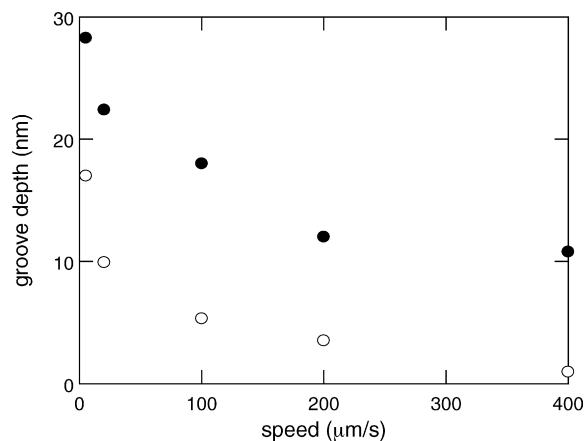


Fig. 6. Depth of the grooves versus translation speed for two different pulse energies: 0.7 nJ (solid circles) and 0.14 nJ (open circles).

irradiated regions. Below the ablation threshold RMS roughness increases from 4 to 10 nm; above threshold surface roughnesses up to 50 nm are observed.

To study the effect of the translation speed on the fs-laser micromachining of MEH-PPV, we prepared two sets of grooves with different pulse energies, for speeds ranging from 5 to 400 $\mu\text{m/s}$. As before, the morphology of such grooves was analyzed through atomic force microscopy. In Fig. 6, we show the depth of the grooves as a function of the translation speed and energies of 0.7 nJ (solid circles) and 0.14 nJ (open circles). The groove depth decreases with increasing translation speed. We also found that for fixed pulse energy the translation speed has little effect on the width of the groove.

We also carried out fluorescence microscopy measurements of the micromachined MEH-PPV films. As shown in Fig. 7, the MEH-PPV film (not exposed to the fs laser) exhibits fluorescence at approximately 600 nm when excited at 540 nm. The inset in this figure corresponds to the fluorescence microscopy image, obtained with excitation at 540 nm, for the sample micromachined at an energy of 0.07 nJ. As can be seen, the micromachined lines present the characteristic fluorescent emission of MEH-PPV, although with smaller intensity in

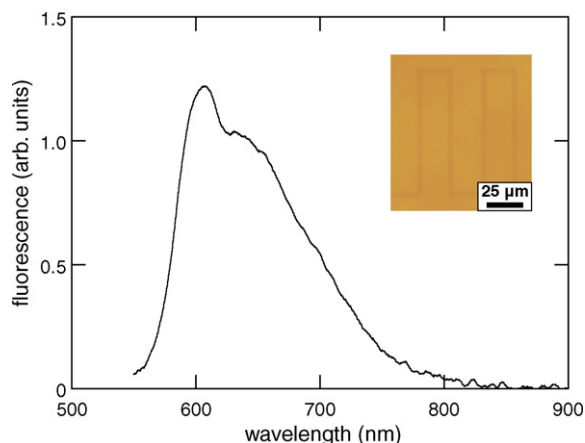


Fig. 7. Fluorescence spectrum of a MEH-PPV film obtained under excitation at 540 nm. The inset shows an image obtained through fluorescence microscopy (excitation at 540 nm) of lines micromachined with an pulse energy of 0.07 nJ.

comparison to the not irradiated region. Similar fluorescence microscopy images were obtained for samples micromachined with energies up to 0.2 nJ, indicating that the conjugated polymer emission is preserved after the fs-laser micromachining under appropriate conditions.

4. Discussion

Our results indicate that the interaction of fs laser pulses with the conjugated polymer MEH–PPV falls into two regimes, depending on the pulse energy [18,23]. For pulses energies up to the ablation threshold of 1.2 nJ, only slight material removal from the film surface occurs, and the maximum observed groove depth is approximately 30 nm, which corresponds to less than 10% of the total film thickness. Above the ablation threshold, we observe groove depths equal to the thickness of the films. Below threshold the depth of the micromachined groove can also be controlled by changing the translation speed, as revealed by the results of Fig. 6.

The increase we observe in the average surface roughness after micromachining has also been reported for poly(methyl-methacrylate) [5,19]. However, as shown in Refs. [5,19], thermal annealing can be used to reduce the laser-machining-induced surface roughness. Therefore, if applications require smooth surfaces, micromachined MEH–PPV samples could be thermally annealed.

As observed in the optical transmission microscopy image (Fig. 2), a decrease in the absorption of MEH–PPV occurs for pulse energies below the ablation threshold. The decrease in MEH–PPV absorbance with pulse energy shown in Fig. 3 cannot be accounted for by the decrease in film thickness. The maximum decrease in the film thickness is 10%, while at the same pulse energy the absorption drops by 62%. Furthermore, the absorbance spectrum observed in Fig. 3 after micromachining with a pulse energy of 0.89 nJ (open circles) is very distinct from the other ones, indicating that photochemical changes to the MEH–PPV structure start to take place around this pulse energy.

A similar response to light exposure (a decrease of MEH–PPV absorbance peak, followed by a change in the spectrum shape) has been reported in the literature [24,25]. Such changes in MEH–PPV absorption was attributed to photo-oxidation induced by one-photon absorption (photobleaching) [24,25]. As the same general features were observed in our results, we attribute the photobleaching observed after the fs-laser micromachining to a two-photon induced oxidation of MEH–PPV. This polymer is completely transparent in the near infrared region (as seen in Fig. 3), but exhibits a large two-photon absorption cross-section at 800 nm (the wavelength employed in the micromachining) [26,27]. These facts support the two-photon induced oxidation hypothesis.

The fluorescence exhibited by MEH–PPV films micromachined with pulse energies below 1.2 nJ (Fig. 7) reveal that the sample preserves its characteristic emission. Although the emission intensity of the micromachined region is diminished due to photobleaching, Fig. 3 shows that an appreciable amount of unbleached MEH–PPV remains in the sample provided the

right pulse energy is used. These results suggest that the polymer's conductive properties may also be preserved after the fs-laser micromachining if the right energy regime is used.

It has been demonstrated that the photo-oxidation of MEH–PPV can be diminished, or even eliminated, when the sample is irradiated in an inert atmosphere [24,25,28]. Although this procedure, irradiation in an inert atmosphere, has been performed only with visible continuum-wave light sources, we believe it also could be employed during fs-laser micromachining (near infra-red irradiation) of MEH–PPV to minimize photobleaching and, consequently, providing samples with a stronger photoluminescence and larger electrical conductivity.

5. Conclusion

In conclusion, we studied the role of pulse energy and translation speed in the resulting morphology of femtosecond laser micromachined MEH–PPV. For pulse energies higher than 1.2 nJ, film removal from the glass substrate occurs. Below 1.2 nJ only superficial material removal occurs, with a maximum groove depth of 30 nm. Furthermore, we demonstrated that although photobleaching occurs during the micromachining process, for the energy regime up to 1.2 nJ, the optical properties of the polymer remain unchanged. The results presented in this paper provide the optimum parameters for fs-laser micromachining of MEH–PPV for applications in polymeric-based photonic devices.

Acknowledgements

This work was carried out with the financial support of the National Science Foundation under contract DMI-0334984 and the Army Research Office under contract W911NF-05-1-0471. C.R. Mendonca acknowledges financial support from FAPESP and CAPES (Brazil).

References

- [1] D. Cristea, P. Obreja, M. Kusko, E. Manea, R. Rebigan, *Mater. Sci. Eng. C* 26 (2006) 1049.
- [2] S. Sowa, W. Watanabe, T. Tamaki, J. Nishii, K. Itoh, *Opt. Express* 14 (2006) 291.
- [3] M.S. Bakir, C.O. Chui, A.K. Okay, K.C. Saraswat, J.D. Meindl, *IEEE Trans. Electron Dev.* 51 (2004) 1084.
- [4] J. Kruger, W. Kautek, *Polymers and Light*, Springer-Verlag, Berlin, 2004.
- [5] J.Y. Cheng, C.W. Wei, K.H. Hsu, T.H. Young, *Sens. Actuators B* 99 (2004) 186.
- [6] N. Yurt, K. Mune, R. Naito, T. Fukuoka, A. Mochizuki, K. Matsumoto, G. Meredith, N. Peyghambarian, G.E. Jabbour, *J. Lightwave Technol.* 23 (2005) 1291.
- [7] E.H. Conradie, D.F. Moore, *J. Micromech. Microeng.* 12 (2002) 368.
- [8] Y.N. Xia, G.M. Whitesides, *Annu. Rev. Mater. Sci.* 28 (1998) 153.
- [9] G.T. Paloczi, J. Scheuer, A. Yariv, *IEEE Photon. Technol. Lett.* 17 (2005) 390.
- [10] A. Yeniyay, R.Y. Gao, K. Takayama, R.F. Gao, A.F. Garito, *J. Lightwave Technol.* 22 (2004) 154.
- [11] W.H. Wong, E.Y.B. Pun, *Appl. Phys. Lett.* 79 (2001) 3576.
- [12] C.B. Schaffer, A. Brodeur, J.F. Garcia, E. Mazur, *Opt. Lett.* 26 (2001) 93.
- [13] D.B. Wolfe, J.B. Ashcom, J.C. Hwang, C.B. Schaffer, E. Mazur, G.M. Whitesides, *Adv. Mater.* 15 (2003) 62.

- [14] E.N. Glezer, M. Milosavljevic, L. Huang, R.J. Finlay, T.H. Her, J.P. Callan, E. Mazur, *Opt. Lett.* 21 (1996) 2023.
- [15] L.M. Tong, R.R. Gattass, I. Maxwell, J.B. Ashcom, E. Mazur, *Opt. Commun.* 259 (2006) 626.
- [16] D.F. Farson, H.W. Choi, C.M. Lu, L.J. Lee, *J. Laser Appl.* 18 (2006) 210.
- [17] W. Watanabe, S. Sowa, T. Tamaki, K. Itoh, J. Nishii, *Jpn. J. Appl. Phys.* 45 (2006) L765.
- [18] T.H.R. Crawford, A. Borowiec, H.K. Haugen, *Appl. Phys. A* 80 (2005) 1717.
- [19] H. Klank, J.P. Kutter, O. Geschke, *Lab on a Chip* 2 (2002) 242.
- [20] G. Yu, J. Gao, J.C. Hummelen, F. Wudl, A.J. Heeger, *Science* 270 (1995) 1789.
- [21] R.H. Friend, R.W. Gymer, A.B. Holmes, J.H. Burroughes, R.N. Marks, C. Taliani, D.D.C. Bradley, D.A. Dos Santos, J.L. Bredas, M. Logdlund, W.R. Salaneck, *Nature* 397 (1999) 121.
- [22] J.H. Burroughes, D.D.C. Bradley, A.R. Brown, R.N. Marks, K. Mackay, R.H. Friend, P.L. Burns, A.B. Holmes, *Nature* 347 (1990) 539.
- [23] K. Furusawa, K. Takahashi, H. Kumagai, K. Midorikawa, M. Obara, *Appl. Phys. A* 69 (1999) S359.
- [24] D.G.J. Sutherland, J.A. Carlisle, P. Elliker, G. Fox, T.W. Hagler, I. Jimenez, H.W. Lee, K. Pakbaz, L.J. Terminello, S.C. Williams, F.J. Himpsel, D.K. Shuh, W.M. Tong, J.J. Jia, T.A. Callcott, D.L. Ederer, *Appl. Phys. Lett.* 68 (1996) 2046.
- [25] W. Holzer, A. Penzkofer, M. Pichlmaier, D.D.C. Bradley, W.J. Blau, *Chem. Phys.* 248 (1999) 273.
- [26] S.L. Oliveira, D.S. Correa, L. De Boni, L. Misoguti, S.C. Zilio, C.R. Mendonca, *Appl. Phys. Lett.* 88 (2006) 021911.
- [27] L. De Boni, A.A. Andrade, D.S. Correa, D.T. Balogh, S.C. Zilio, L. Misoguti, C.R. Mendonca, *J. Phys. Chem. B* 108 (2004) 5221.
- [28] J.C. Scott, J.H. Kaufman, P.J. Brock, R. DiPietro, J. Salem, J.A. Goitia, *J. Appl. Phys.* 79 (1996) 2745.

Femtosecond laser micromachining in transparent materials

Femtosecond laser micromachining can be used either to remove materials or to change a material's properties, and can be applied to both absorptive and transparent substances. Over the past decade, this technique has been used in a broad range of applications, from waveguide fabrication to cell ablation. This review describes the physical mechanisms and the main experimental parameters involved in the femtosecond laser micromachining of transparent materials, and important emerging applications of the technology.

RAFAEL R. GATTASS AND ERIC MAZUR

Department of Physics and School of Engineering and Applied Sciences,
Harvard University, 9 Oxford Street, Cambridge, Massachusetts 02138, USA
e-mail: mazur@seas.harvard.edu

Femtosecond laser micromachining was first demonstrated in 1994, when a femtosecond laser was used to ablate micrometre-sized features on silica and silver surfaces^{1,2}. In less than ten years the resolution of surface ablation has improved to enable nanometre-scale precision^{3,4}. Several review articles are available on femtosecond lasers^{5,6}, nonlinear processes^{7–9}, optical breakdown^{7,9}, surface micromachining^{10,11} and the history of femtosecond laser micromachining¹². In this review we shall focus on the femtosecond micromachining of bulk transparent materials — that is, materials that do not have any linear absorption at the wavelength of the femtosecond laser — for the fabrication of photonic devices, as well as other applications.

There are unique advantages in favour of femtosecond laser micromachining of transparent materials over other photonic-device fabrication techniques. First, the nonlinear nature of the absorption confines any induced changes to the focal volume. This spatial confinement, combined with laser-beam scanning or sample translation, makes it possible to micromachine geometrically complex structures in three dimensions. Second, the absorption process is independent of the material, enabling optical devices to be fabricated in compound substrates of different materials. Third, femtosecond laser micromachining can be used for the fabrication of an 'optical motherboard', where all interconnects are fabricated separately, before (or even after) bonding several photonic devices to a single transparent substrate.

PHYSICAL MECHANISMS FOR FEMTOSECOND LASER MICROMACHINING

Femtosecond laser micromachining results from laser-induced optical breakdown (Box 1), a process by which optical energy is transferred to the material, ionizing a large number of electrons that, in turn, transfer energy to the lattice. As a result of the irradiation, the material can undergo a phase or structural modification, leaving behind a localized permanent change in the refractive index or even a void.

The absorption of light in a transparent material must be nonlinear because there are no allowed electronic transitions at the energy of the incident photon^{7,13}. For such nonlinear absorption to occur, the electric-field strength in the laser pulse must be approximately equal to the electric field that binds the valence electrons in the atoms — of the order of 10^9 V m^{-1} , corresponding to a laser intensity of $5 \times 10^{20} \text{ W m}^{-2}$ (ref. 9). To achieve such electric-field strengths with a laser pulse, high intensities and tight focusing are required. For example, a 1- μJ , 100-fs laser pulse must be focused to a 200- μm^2 area. The tight focusing and the nonlinear nature of the absorption make it possible to confine the absorption to the focal volume inside the bulk of the material without causing absorption at the surface, yielding micromachined volumes as small as 0.008 μm^3 (ref. 14).

During irradiation, the laser pulse transfers energy to the electrons through nonlinear ionization^{15,16}. For pulse durations greater than 10 fs, the nonlinearly excited electrons are further excited through phonon-mediated linear absorption, until they acquire enough kinetic energy to excite other bound electrons — a process called avalanche ionization. When the density of excited electrons reaches about 10^{29} m^{-3} , the electrons behave as a plasma with a natural frequency that is resonant with the laser — leading to reflection and absorption of the remaining pulse energy^{15,17}.

Figure 1 shows the timescales for a number of relevant physical processes involved in femtosecond laser micromachining. Part of the optical energy absorbed by the electrons is transferred to the lattice over a picosecond timescale. Within a couple of nanoseconds, a pressure or a shock wave separates from the dense, hot focal volume^{18,19,20}. On the microsecond timescale, the thermal energy diffuses out of the focal volume. At a sufficiently high energy these processes cause melting or non-thermal ionic motion and leave behind permanent structural changes²¹.

Understanding the different timescales involved in converting the laser pulse energy into a structural change provides an insight into why ultrashort laser pulses are well suited for micromachining applications. Laser-induced damage has been studied since the early days of the laser¹², but damage caused by femtosecond laser pulses is fundamentally different from damage caused by laser pulses with a duration greater than one picosecond. For pulses of subpicosecond duration, the timescale over which the electrons are excited is smaller than the electron–phonon scattering time (about 1 ps). Thus, a femtosecond laser pulse ends before the electrons thermally

excite any ions. Heat diffusion outside the focal area is minimized, increasing the precision of the method^{22,23}. Additionally, femtosecond laser processing is a deterministic process because no defect electrons are needed to seed the absorption process; enough seed electrons are generated through nonlinear ionization from the first tens of femtoseconds of the pulse^{1,16}. The confinement and repeatability of the nonlinear excitation make it possible to use the femtosecond-laser-induced damage for practical purposes.

BULK DAMAGE AND EXPERIMENTAL PARAMETERS

If the energy transfer from the laser pulse was caused solely by nonlinear ionization, the intensity required to induce a permanent change would depend nonlinearly on the bandgap of the irradiated material. The probability of light being absorbed in a material that has a bandgap energy equivalent to N photons through nonlinear absorption is I^N , where I is the electric-field intensity. Because the bandgap energy (and therefore N) varies from material to material, the nonlinear absorption would vary enormously. Experimentally, however, the threshold intensity, I_{th} , required to damage a material is found to vary only very slightly with the bandgap energy (Fig. 2), indicating the importance of avalanche ionization, which depends linearly on I . Because of this low dependence on the bandgap energy, femtosecond laser micromachining can be used in a broad range of materials.

The intensity required to damage a material is determined by three experimental parameters: the laser pulse duration, τ , the pulse energy, E , and the focusing numerical aperture, NA. The minimum τ and maximum E are usually fixed by the laser system, leaving only the variable NA free. At first glance, the effects of τ , E and NA on the intensity at a given wavelength, λ , would be expected to follow²⁴:

$$I \propto E NA^2 / [\tau \lambda^2 (1 - NA^2)]. \quad (1)$$

However, as shown below, the dependence of I_{th} for micromachining on these three parameters does not follow the expected behaviour.

The dependence of I_{th} on τ has been explored for values of τ down to 10 fs, and experiments do not reveal the expected inverse relation between I and τ given by equation 1. For $\tau > 10$ ps, I_{th} varies as $\tau^{1/2}$, indicating that Joule heating of the electrons excited at the beginning of the pulse is responsible for the optical damage¹⁷. For $\tau < 10$ ps, I_{th} increases threefold for a tenfold increase in τ (ref. 25). The low level of dependence on τ is due to avalanche ionization: nonlinear ionization creates the initial seed population, but the linear dependence of the avalanche process on I is responsible for the high excitation density necessary for micromachining^{13,16}. The relatively small effect of altering τ on I_{th} provides flexibility in the choice of laser system, which is important for commercial applications of femtosecond laser micromachining.

For conditions where τ and NA are fixed, the absorption process has a strong dependence on E . The minimum E required for the nonlinear absorption that seeds electrons is the threshold energy. When E is kept close to this threshold, the absorption produces a change in the index of refraction that is localized to the focal volume. The magnitude of the refractive-index change varies from material to material, with both positive and negative index contrasts being reported. The refractive-index change is usually of the same order of magnitude as that found in standard optical fibres, that is, around 10^{-3} (refs 26–30). The change in the refractive index is not spatially homogeneous, and the mechanisms responsible for the spatially dependent change are under investigation; stress-induced changes, densification, changes in effective fictive temperature, and colour-centre formation contribute differently for each material system and for each set of processing conditions^{27,30–35}. Increasing E beyond the threshold increases the size of the affected area and the average energy of the plasma. As the plasma energy increases, ionic shielding is reduced causing Coulomb repulsion between ions. A surge of Coulomb repulsion with sufficient energy leads to void formation³². Even if E is not large enough for void formation, interference between the incident pulse and the electron plasma can occur, resulting in a

Box 1 A nonlinear absorption process

When a femtosecond laser pulse with a high enough pulse peak intensity is focused into a material, optical breakdown is observed (Fig. B1a). The laser pulse energy is partially transferred to the electrons in the short duration of the pulse. The highly excited electrons thermalize with the ions and alter the material permanently. Depending on the degree of excitation, cracking, void formation or localized melting occurs. In the absence of impurities, carriers are generated initially by multiphoton absorption, promoting electrons from the valence to the conduction band (Fig. B1b). Several photons must be incident

on an electron at the same time for the process to occur with a high probability. For example, the six-photon absorption cross-section of fused silica is approximately $6 \times 10^4 \text{ m}^3 \text{ ps}^{-1} (\text{m}^2/\text{TW})^6$ (ref. 13). The micromachined feature size will depend on many experimental parameters: E (the pulse energy), τ (the pulse duration) and NA (the focusing numerical aperture). However, under special conditions, exposure to multiple pulses can further change the feature size. Figure B1c shows microscope images of the large variation in the features of femtosecond-laser-induced changes, due to experimental conditions.

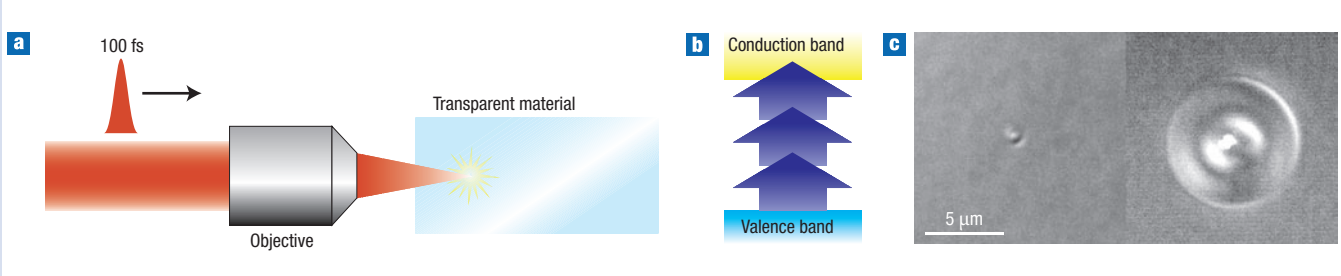


Figure B1 Femtosecond laser micromachining process. **a**, Schematic of the laser incident on a transparent material. **b**, Diagram of the excitation of electrons to the conduction band. **c**, Microscope images showing the large variation in the feature characteristics depending on the experimental conditions. Left: single 10-nJ pulse and right: 25,000 5-nJ pulses at a frequency of 25 MHz (both with the same focal spot).

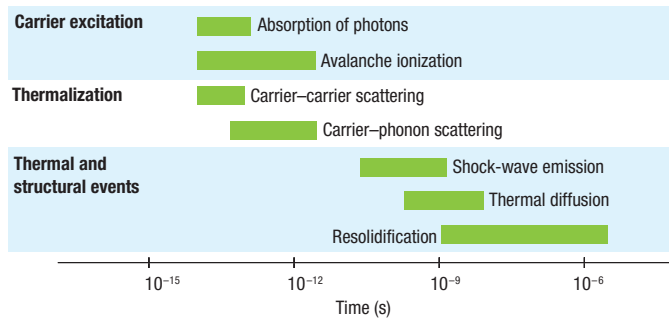


Figure 1 Timescale of the physical phenomena associated with the interaction of a femtosecond laser pulse with transparent materials. The green bars represent typical timescales for the relevant process. Note that although the absorption of light occurs at the femtosecond timescale, the material can continue to undergo changes microseconds later.

birefringent periodic modulation^{36–40}. Most photonic applications use values of E that are close to the absorption threshold and thus result in changes in the refractive index.

The third experimental parameter, NA, determines the width of the focal volume and therefore the resulting feature size. The range of NAs that can be used, however, is limited. Numerical apertures larger than 0.002 are required to achieve I_{th} with the millijoule values of E that are available with commercial amplified laser systems. In practice, the minimum NA is significantly larger than this value because at low NA, two nonlinear processes compete with the energy deposition: self-focusing and white-light generation. Self-focusing — an intensity-dependent distortion of the propagating wavefront — manifests itself when the laser-pulse power exceeds a critical value (about 4 MW for fused silica)⁴¹, causing the pulse to collapse into a filament with a diameter that is smaller than the one expected from the external focusing^{42,43}. White-light generation causes spectral broadening of the laser pulse as it propagates⁴⁴. For NAs below 0.1, the intensity threshold of both these nonlinear processes is lower than I_{th} (refs 24,45). The nonlinear effects reduce the repeatability and the control over the micromachining processes, and the resulting feature size is no longer determined by the external focusing^{24,46,47}.

At NAs close to or larger than unity, femtosecond laser micromachining can be accomplished in glasses with femtosecond laser oscillators delivering just nanojoules of energy per pulse⁴⁸. Laser oscillators, with their high repetition rates, can be used to increase the area that can be patterned in a given amount of time and to allow control over the size of the micromachined area. In oscillator-only machining, the time interval between pulses is smaller than the heat diffusion time (about 1 μ s). The energy delivered by each pulse accumulates at the focus before diffusing out, forming a point source of heat^{48,49}. Because of this ensuing diffusion, the feature sizes can significantly exceed the focal volume, creating spherical features up to 50 μ m in diameter, using a focal spot of only 0.5 μ m (ref. 48). Although at high NAs, the NA sets the threshold energy, the feature size is controlled by the number of incident pulses.

Besides altering I , the NA also affects the geometry of the final structure in single-shot experiments. Above an NA of 0.6, the micromachined features are almost spherically symmetric; below this value, the resulting structures become larger and asymmetric. Changing the spatial profile and divergence of the input beam prior to focusing, such that the focal-spot profile is closer to a symmetric circular cross-section, can mitigate the asymmetry^{50,51}.

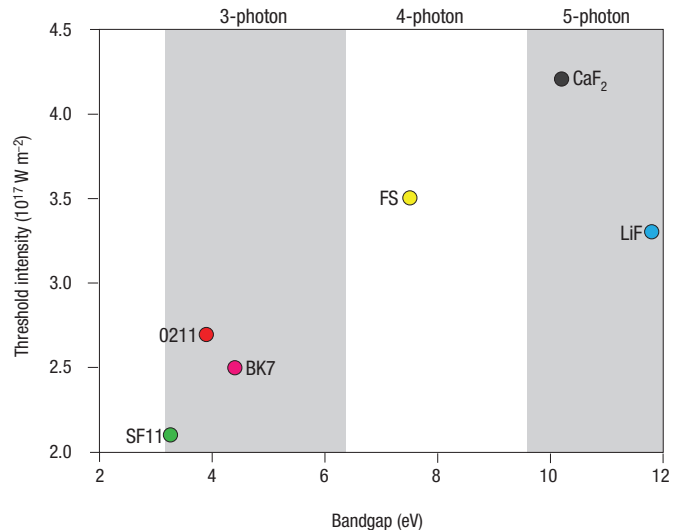


Figure 2 Bandgap dependence of the threshold fluence for femtosecond laser micromachining by pulses centred at a wavelength of 800 nm with a duration of 100 fs. The bandgaps of the materials depicted by coloured circles range over various multiphoton orders for the incident photon energy of 1.55 eV. The threshold intensity does not follow a power law, increasing by only about a factor of two as the energy required to span the bandgap increases from three to five photons. Because femtosecond laser micromachining is nearly independent of the bandgap of the material it can be used in a wide range of materials.

Beam shaping to alter the final geometry at low NAs remains an active topic of research.

PHOTONIC APPLICATIONS

Femtosecond micromachining has been used to fabricate photonic devices using a variety of transparent substrates, including glasses, crystals and polymers. Owing to their high purity and large transparency window, glasses and crystals are commonly used as base materials. A wide variety of femtosecond-laser-micromachined devices, discussed in more detail below, have been demonstrated using glasses and crystals, including waveguides, active devices, filters and resonators.

The use of transparent polymers as a substrate material for fabrication presents advantages over other transparent materials. First, for polymer processing, I_{th} is at least one order of magnitude lower than for glass processing. Polymers are also an attractive medium owing to the ease with which dopants can be incorporated into them, the diversity of available compositions and physical properties, and their low cost. However, compared with glasses and crystals, polymers have higher transmission losses. So far only a few photonic devices have been directly fabricated in polymers, such as ring-mode⁵² and single-mode⁵³ waveguides in polymethylmethacrylate.

WAVEGUIDES

Along with data storage¹⁴, waveguide fabrication was one of the first demonstrations of the potential of femtosecond laser micromachining for photonic applications^{30,54}. Femtosecond-laser-micromachined waveguides can serve as interconnects in a variety of host glasses, and have opened up the possibility of three-dimensional layering of waveguides. The pulse energy required for fabricating devices can be as low as a few nanojoules, requiring only a laser oscillator^{26,48} (see, for example, Fig. 3a). The

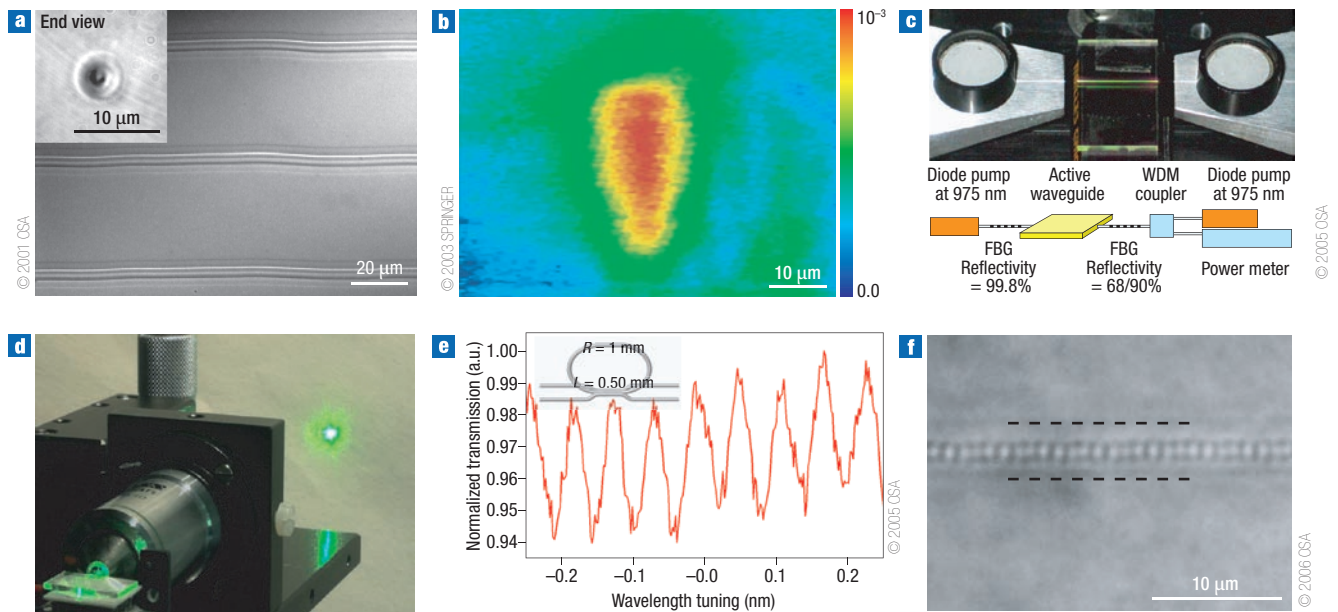


Figure 3 Photonic applications of femtosecond laser micromachining. **a**, Optical microscope image of an oscillator-only femtosecond-laser-micromachined waveguide inside bulk glass. The inset shows one end face of the waveguide. Reprinted with permission from ref. 48. **b**, Measured refractive-index profile of a waveguide micromachined using a 0.45-NA objective with the laser beam incident from the top. False colour bar added to show the magnitude of the refractive-index change. Reproduced with permission from ref. 60. **c**, Image of a femtosecond laser micromachined lasing waveguide. FBG is fibre Bragg grating and WDM is wavelength-division multiplexer. Courtesy of Roberto Osellame. **d**, Image of a frequency conversion waveguide in a lithium niobate crystal. Courtesy of Stefan Nolte. **e**, Normalized transmission through the resonator versus wavelength (relative to the laser centre wavelength of 800 nm). The inset shows a schematic of a vertical resonator design. R is the radius of curvature and L is the overlap length. Reprinted with permission from ref. 71. **f**, Optical micrograph of a waveguide Bragg grating structure. The horizontal black lines indicate the edge of the waveguide. Reprinted with permission from ref. 72.

oscillator-only technique increases the rate of fabrication by three to four orders of magnitude, and also enables simple control over the cross-sectional diameter without altering the focusing conditions. Although femtosecond laser fabrication is a serial process, 10- μm waveguides spaced by 10 μm can be micromachined over an area of $10 \times 10 \text{ mm}^2$ in about 10 minutes. Because there is no need for either a mask or post-development processing, the rate of fabrication using femtosecond lasers is now approaching that of lithographic techniques.

Over the past decade, the transmission losses, refractive-index contrast and bending radii of femtosecond-laser-micromachined interconnects have been characterized. Transmission losses are of the order of 0.1 dB mm^{-1} for a large variety of materials and processing conditions^{27–29,49,55–58}. The spatial profile of the refractive index of waveguides is strongly dependent on the material and the processing conditions^{26–30,59}, and is close to that of a fibre for fused silica substrates^{27,60} (see, for example, Fig. 3b). Additionally, minimum bending radii of the order of tens of millimetres have been achieved^{55,58}. Photonic-circuit designs might require micromachining interconnects across several substrates. Optically connected waveguides have already been fabricated in bonded doped and undoped phosphate glass⁶⁰, and also through multiple pieces of glass separated by air gaps⁶¹.

ACTIVE DEVICES

The initial application of femtosecond laser micromachining to active devices involved devices with optical gain⁶². Both femtosecond-laser-micromachined amplifiers^{62,63} with a gain of 0.25 dB mm^{-1} (ref. 64) and an Er:Yb-doped phosphate glass laser based on a femtosecond-laser-written waveguide have been

demonstrated⁶⁵ (Fig. 3c). The materials used for micromachining photonic devices have not been restricted to glasses. Waveguides have been fabricated in electro-optic crystals, such as lithium niobate (albeit with no demonstration of electro-optic switching)⁶⁶. Nonlinear frequency conversion in femtosecond-laser-micromachined waveguides in lithium niobate shows a 49% conversion efficiency over a length of 9.3 mm (see ref. 67 and Fig. 3d). The feasibility of magnetic switching has also been demonstrated with waveguide micromachining in a Faraday material, with the micromachined region showing almost no change in the Verdet constant from the non-irradiated material⁶⁸.

FILTERS AND RESONATORS

In principle, devices fabricated with planar lithographic techniques can be fabricated with femtosecond laser micromachining. Indeed, couplers, filters and interleavers have already been demonstrated^{26,28,46,55,60,69,70}. The three-dimensional degree of freedom permits the fabrication of vertical resonators, and vertical and lateral splitters^{55,60,71} (see, for example, Fig. 3e). Femtosecond laser micromachining of fibre Bragg grating filters in the bulk of a material was first demonstrated using multiple exposures (Fig. 3f, ref. 72), but recently greater than 30-dB-strength Bragg gratings have been fabricated with a single exposure^{73,74}. The long-term stability of the laser-induced index change makes femtosecond laser micromachining also attractive for both long-period fibre gratings^{75,76} and normal gratings^{77–79}.

POLYMERIZATION

The intrinsic nonlinear spatial confinement of femtosecond laser microfabrication can be used not only to process cured polymers,

but also to induce polymerization in a resin⁸⁰. Usually referred to as two-photon polymerization⁸¹, or laser direct writing⁸², this polymerization technique makes it possible to fabricate polymer structures with a high degree of complexity. Many interesting optical applications of two-photon polymerization exist⁸³, most notably three-dimensional photonic crystals^{84,85}. Two-photon polymerization is a large field with applications far exceeding the domain of photonics, most of which have already been reviewed^{80,83}.

NEW AVENUES OF RESEARCH

NANOSURGERY

Lasers have been used for selective targeting of structures and cells for more than four decades⁸⁶. Until recently, this work involved pulses with durations in the range of picoseconds or longer⁸⁷. As a consequence of these long pulse durations, large amounts of energy are required to induce a material change. Although subwavelength resolution has been reported⁸⁸, heating and shock-wave propagation leads to collateral damage⁸⁹. In biological applications, control over the energy deposition is crucial; for cells even a minor rise in temperature leads to cell death⁸⁹. Femtosecond laser pulses make precise energy delivery possible, resulting in clear, highly localized cuts in biological samples⁹⁰. The ability to selectively ablate an area using femtosecond laser pulses was first demonstrated in the process of chromosome division⁹⁰, and later extended to subcellular organelles^{91–93} (for example, Fig. 4a). With these initial demonstrations, femtosecond lasers have established themselves as versatile tools in biology with a broad range of applications, including selective neurosurgery for behaviour assays of the neuronal network in the roundworm, *C. elegans* (refs 94,95).

MATERIAL PROCESSING

The controlled delivery of thermal energy during femtosecond laser micromachining can be used for material processing. Bonding of dissimilar materials is an engineering challenge because the mismatch between thermal expansion coefficients causes thermo-mechanical stress at the joint, weakening the bond⁹⁶. Also, bonding two transparent materials requires an additional, partially opaque intermediate layer⁹⁶. Femtosecond laser processing based on nonlinear absorption overcomes the need for this intermediate layer, and the rapid cooling strengthens the bond. For example, processing with femtosecond laser pulses forms a 14.9-MPa bond between borosilicate glasses^{97,98} (Fig. 4b), a 15.3-MPa bond between transparent materials with dissimilar thermal expansion coefficients (such as borosilicate and fused silica)⁹⁶ and a 3.7-MPa bond between non-alkali glass and silicon crystal⁹⁹.

Femtosecond lasers can also be used to induce spatially selective phase transitions within a material. For example, crystals can be grown inside a piece of glass by exposing it to a series of femtosecond pulses^{100,101}. The laser pulses heat the glass in the focal volume beyond the melting point, acting as a localized source of heat. Once a seed crystal is formed, the repeated heating and cooling causes these seed crystals to grow. This technique for inducing phase transitions can also be used for data-storage applications. For example, when samarium ions embedded in a glass host are irradiated with a femtosecond laser pulse, a transition from Sm^{3+} to Sm^{2+} is induced¹⁰². The exposed ions fluoresce at a different wavelength from the unexposed ions, and so each exposed area can act as a data-storage bit (Fig. 4c).

MICROFLUIDIC DEVICES

The fast automated and parallel processing of small quantities of fluid requires an increasing miniaturization of chemical and

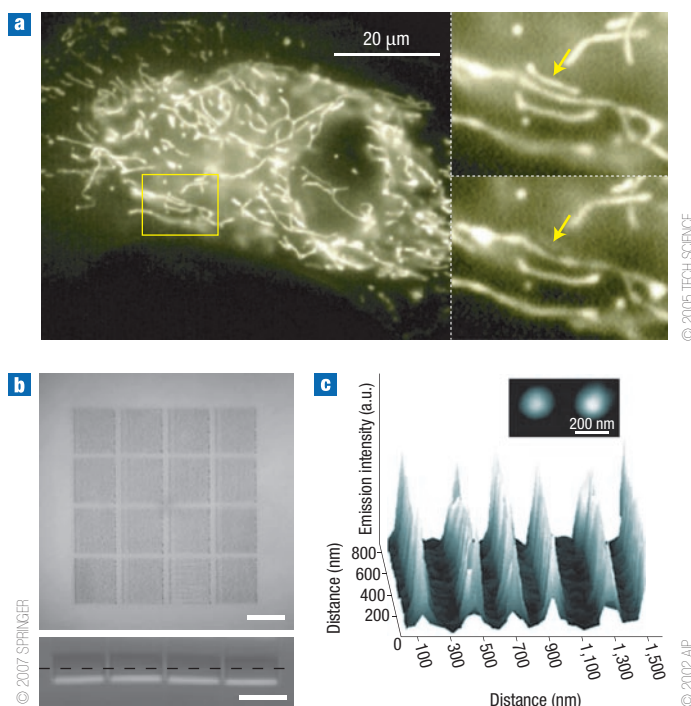


Figure 4 Example applications of femtosecond micromachining in biology, material processing and data storage. **a**, Ablation of a single mitochondrion in a living cell. Fluorescence microscopic image showing multiple mitochondria in yellow before femtosecond laser irradiation. Target mitochondrion (marked by arrow) before (top inset) and after (bottom inset) laser ablation with 2-nJ, 100-fs pulses. Reprinted with permission from ref. 92. **b**, Microscope optical image of a femtosecond laser bonded borosilicate glass interface. Top view (top) and side view (bottom) of the joining area bonded using 1-μJ pulse energy and 0.1-mm s⁻¹ translation velocity. The scale bar is 100 μm. Reprinted with permission from ref. 98. **c**, Photoluminescence emission of femtosecond photoreduced Sm^{2+} ions. The inset shows a samarium-ion bit that has 200-nm resolution. Reprinted with permission from ref. 102.

biological set-ups^{103–105}. So far the fabrication of such so-called microfluidic devices is mainly planar. Because the dimensions required for channels, valves and other components are within the realm of femtosecond-laser-micromachining capabilities, three-dimensional microfluidic devices have become feasible. Three-dimensional channel fabrication was demonstrated by hydrofluoric acid (HF) etching of regions in silica that had been exposed to femtosecond laser pulses (for example, Fig. 5a). Although HF etches silica too, the laser-exposed material reacts more readily with HF than unexposed areas¹⁰⁶. Alternatively, the etching rate can be increased by selective precipitation of a crystalline phase inside photosensitive glasses that have been irradiated with femtosecond laser pulses, enabling the fabrication of channels¹⁰⁷ and complete so-called ‘micro total analysis’ systems¹⁰⁸. Although the laser processing time for a micro-total-analysis system is large compared with the time required for lithographic and replication processing, femtosecond laser micromachining allows new channel geometries and glass-based devices. Femtosecond laser micromachining also opens the possibility for direct integration with optical detection by *in situ* fabrication of waveguides¹⁰⁹.

RAPID PROTOTYPING

Because femtosecond laser micromachining does not require any mask or post-development steps, it is a suitable technique for rapid

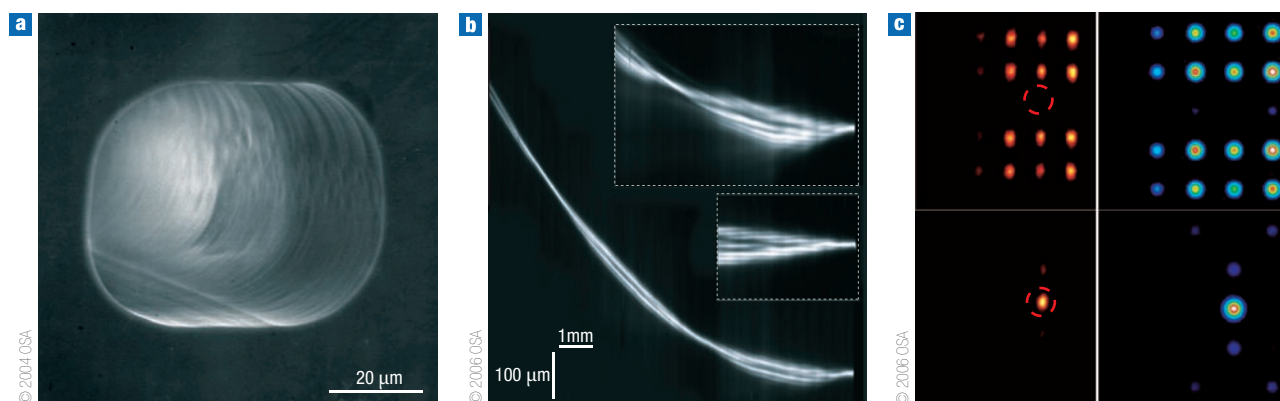


Figure 5 Examples of microfluidic and rapid prototyping applications of femtosecond micromachining. **a**, Scanning electron micrograph of a microfluidic channel fabricated by HF-etching femtosecond-micromachined areas inside fused silica. Reprinted with permission from ref. 113. **b**, Fluorescence imaging of Bloch oscillations inside a bulk piece of glass for the central waveguide excitation of a straight array with period $a = 10 \mu\text{m}$. The top inset shows a curved array with radius of curvature $R = 77 \text{ mm}$ and period $a = 10 \mu\text{m}$. The bottom inset shows a curved array with $R = 77 \text{ mm}$ and $a = 8 \mu\text{m}$. Reprinted with permission from ref. 110. **c**, Measured (right) and theoretical (left) outputs from a square waveguide array at a peak power of 40 kW (top) and 1,000 kW (bottom). Reprinted with permission from ref. 111.

prototyping of photonic devices. Arrays of curved waveguides were micromachined in a glass substrate doped with a fluorescent molecule, to study the optical equivalent of Bloch oscillations (Fig. 5b, ref. 110). Two-dimensional arrays of waveguides were used to study spatial solitons¹¹¹. Figure 5c shows the transition between a delocalized state and a spatial soliton as the pulse intensity through these coupled waveguides is increased. In both studies, the short turnaround time of femtosecond laser micromachining has been used to optimize the fabricated structures and demonstrate new aspects of waveguide coupled-mode theory¹¹².

CONCLUSION

Femtosecond laser micromachining presents unique capabilities for three-dimensional, material-independent, subwavelength processing. It enables the fabrication of three-dimensional photonic devices with far greater ease than lithography, and the field is maturing at an extraordinary pace. Because femtosecond laser micromachining also holds great promise beyond the field of photonics, it is a technology that creates new markets for the laser industry and enables innovative applications.

doi:10.1038/nphoton.2008.48

References

- Du, D., Liu, X., Korn, G., Squier, J. & Mourou, G. Laser-induced breakdown by impact ionization in SiO_2 with pulse widths from 7 ns to 150 fs. *Appl. Phys. Lett.* **64**, 3071–3073 (1994).
- Pronko, P. P. *et al.* Machining of submicron holes using a femtosecond laser at 800-nm. *Opt. Commun.* **114**, 106–110 (1995).
- Joglekar, A. P. *et al.* A study of the deterministic character of optical damage by femtosecond laser pulses and applications to nanomachining. *Appl. Phys. B* **77**, 25–30 (2003).
- Chimmalgai, A., Choi, T. Y., Grigoropoulos, C. P. & Komvopoulos, K. Femtosecond laser apertureless near-field nanomachining of metals assisted by scanning probe microscopy. *Appl. Phys. Lett.* **82**, 1146–1148 (2003).
- Backus, S., Durfee III, C. G., Murnane, M. M. & Kapteyn, H. C. High power ultrafast lasers. *Rev. Sci. Instrum.* **69**, 1207–1223 (1998).
- Keller, U. Recent developments in compact ultrafast lasers. *Nature* **424**, 831–838 (2003).
- Brabec, T. & Krausz, F. Intense few-cycle laser fields: Frontiers of nonlinear optics. *Rev. Mod. Phys.* **72**, 545–591 (2000).
- Steinmeyer, G., Sutter, D. H., Gallmann, L., Matuschek, N. & Keller, U. Frontiers in ultrashort pulse generation: Pushing the limits in linear and nonlinear optics. *Science* **286**, 1507–1512 (1999).
- Boyd, R. W. *Nonlinear optics* 2nd edn (Academic, Amsterdam, 2003).
- Kruger, J. & Kautek, W. in *Polymers and Light* Vol. 168 (ed. Lippert, T.) 247–289 (Springer, Berlin, 2004).
- Dausinger, F., Lichtner, F. & Lubatschowski, H. *Femtosecond Technology for Technical and Medical Applications* (Springer, Berlin, 2004).

- Bloembergen, N. A brief history of light breakdown. *J. Nonlinear Opt. Phys.* **6**, 377–385 (1997).
- Schaffer, C. B., Brodeur, A. & Mazur, E. Laser-induced breakdown and damage in bulk transparent materials induced by tightly-focused femtosecond laser pulses. *Meas. Sci. Technol.* **12**, 1784–1794 (2001).
- Glezer, E. N. *et al.* Three-dimensional optical storage inside transparent materials. *Opt. Lett.* **21**, 2023–2025 (1996).
- Stuart, B. C., Feit, M. D., Rubenchik, A. M., Shore, B. W. & Perry, M. D. Laser-induced damage in dielectrics with nanosecond to subpicosecond pulses. *Phys. Rev. Lett.* **74**, 2248–2251 (1995).
- Stuart, B. C. *et al.* Nanosecond-to-femtosecond laser-induced breakdown in dielectrics. *Phys. Rev. B* **53**, 1749–1761 (1996).
- Bloembergen, N. Laser-induced electric breakdown in solids. *IEEE J. Sel. Top. Quant. Electron.* **10**, 375–386 (1974).
- Schaffer, C. B., Nishimura, N., Glezer, E. N., Kim, A. M. T. & Mazur, E. Dynamics of femtosecond laser-induced breakdown in water from femtoseconds to microseconds. *Opt. Express* **10**, 196–203 (2002).
- Sakakura, M. & Terazima, M. Initial temporal and spatial changes of the refractive index induced by focused femtosecond pulsed laser irradiation inside a glass. *Phys. Rev. B* **71**, 024113 (2005).
- Sakakura, M., Terazima, M., Shimotsuma, Y., Miura, K. & Hirao, K. Observation of pressure wave generated by focusing a femtosecond laser pulse inside a glass. *Opt. Express* **15**, 5674–5686 (2007).
- Sundaram, S. K. & Mazur, E. Inducing and probing non-thermal transitions in semiconductors using femtosecond laser pulses. *Nature Mater.* **1**, 217–224 (2002).
- Chichkov, B. N., Momma, C., Nolte, S., von Alvensleben, F. & Tunnermann, A. Femtosecond, picosecond and nanosecond laser ablation of solids. *Appl. Phys. A* **63**, 109–115 (1996).
- Liu, X., Du, D. & Mourou, G. Laser ablation and micromachining with ultrashort laser pulses. *IEEE J. Sel. Top. Quant. Electron.* **33**, 1706–1716 (1997).
- Ashcom, J. B., Gattass, R. R., Schaffer, C. B. & Mazur, E. Numerical aperture dependence of damage and supercontinuum generation from femtosecond laser pulses in bulk fused silica. *J. Opt. Soc. Am. B* **23**, 2317–2322 (2006).
- Tien, A. C., Backus, S., Kapteyn, H., Murnane, M. & Mourou, G. Short-pulse laser damage in transparent materials as a function of pulse duration. *Phys. Rev. Lett.* **82**, 3883–3886 (1999).
- Streltsov, A. M. & Borrelli, N. F. Fabrication and analysis of a directional coupler written in glass by nanojoule femtosecond laser pulses. *Opt. Lett.* **26**, 42–43 (2001).
- Will, M., Nolte, S., Chichkov, B. N. & Tunnermann, A. Optical properties of waveguides fabricated in fused silica by femtosecond laser pulses. *Opt. Lett.* **27**, 4360–4364 (2002).
- Florea, C. & Winick, K. A. Fabrication and characterization of photonic devices directly written in glass using femtosecond laser pulses. *J. Lightwave Tech.* **21**, 246–253 (2003).
- Osellame, R. *et al.* Optical properties of waveguides written by a 26 MHz stretched cavity Ti:sapphire femtosecond oscillator. *Opt. Express* **13**, 612–620 (2005).
- Miura, K., Qiu, J. R., Inouye, H., Mitsuyu, T. & Hirao, K. Photowritten optical waveguides in various glasses with ultrashort pulse laser. *Appl. Phys. Lett.* **71**, 3329–3331 (1997).
- Bruckner, R. Properties and structure of vitreous silica. I. *J. Non-Cryst. Solids* **5**, 123 (1970).
- Glezer, E. N. & Mazur, E. Ultrafast-laser driven micro-explosions in transparent materials. *Appl. Phys. Lett.* **71**, 882–884 (1997).
- Chan, J. W., Huser, T., Risbud, S. & Krol, D. M. Structural changes in fused silica after exposure to focused femtosecond laser pulses. *Opt. Lett.* **26**, 1726–1728 (2001).
- Streltsov, A. M. & Borrelli, N. F. Study of femtosecond-laser-written waveguides in glasses. *J. Opt. Soc. Am. B* **19**, 2496–2504 (2002).
- Schaffer, C. B., Garcia, J. F. & Mazur, E. Bulk heating of transparent materials using a high repetition-rate femtosecond laser. *Appl. Phys. A* **76**, 351–354 (2003).
- Sudrie, L., Franco, M., Prade, B. & Mysyrowicz, A. Study of damage in fused silica induced by ultra-short IR laser pulses. *Opt. Commun.* **191**, 333–339 (2001).
- Shimotsuma, Y., Kazansky, P. G., Qiu, J. R. & Hirao, K. Self-organized nanogratings in glass irradiated by ultrashort light pulses. *Phys. Rev. Lett.* **91**, 247405 (2003).

38. Bricchi, E., Klappauf, B. G. & Kazansky, P. G. Form birefringence and negative index change created by femtosecond direct writing in transparent materials. *Opt. Lett.* **29**, 119–121 (2004).
39. Kazansky, P. G. *et al.* "Quill" writing with ultrashort light pulses in transparent materials. *Appl. Phys. Lett.* **90**, 151120 (2007).
40. Rajeev, P. P. *et al.* Transient nanoplasmonics inside dielectrics. *J. Phys. B* **40**, S273–S282 (2007).
41. Brodeur, A. & Chin, S. L. Band-gap dependence of the ultrafast white-light continuum. *Phys. Rev. Lett.* **80**, 4406–4409 (1998).
42. Marburger, J. H. Self-focusing: Theory. *Prog. Quant. Electron.* **4**, 35–110 (1975).
43. Shen, Y. R. Self-focusing: Experimental. *Prog. Quant. Electron.* **4**, 1–34 (1975).
44. Alfano, R. R. & Shapiro, S. L. Observation of self-phase modulation and small-scale filaments in crystals and glasses. *Phys. Rev. Lett.* **24**, 592–594 (1970).
45. Nguyen, N. T., Salimnia, A., Liu, W., Chin, S. L. & Vallee, R. Optical breakdown versus filamentation in fused silica by use of femtosecond infrared laser pulses. *Opt. Lett.* **28**, 1591–1593 (2003).
46. Homoele, D., Wielandy, S., Gaeta, A. L., Borrelli, N. F. & Smith, C. Infrared photosensitivity in silica glasses exposed to femtosecond laser pulses. *Opt. Lett.* **24**, 1311–1313 (1999).
47. Kamata, M. & Obara, M. Control of the refractive index change in fused silica glasses induced by a loosely focused femtosecond laser. *Appl. Phys. A* **78**, 85–88 (2004).
48. Schaffer, C. B., Brodeur, A., Garcia, J. F. & Mazur, E. Micromachining bulk glass by use of femtosecond laser pulses with nanojoule energy. *Opt. Lett.* **26**, 93–95 (2001).
49. Eaton, S. M. *et al.* Heat accumulation effects in femtosecond laser-written waveguides with variable repetition rate. *Opt. Express* **13**, 4708–4716 (2005).
50. Cheng, G. H., Wang, Y. S., Liu, Q., Zhao, W. & Chen, G. F. Study of three-dimensional storage by parallel writing in PMMA with femtosecond laser pulses. *Acta Phys. Sinica* **53**, 436–440 (2004).
51. Osellame, R. *et al.* Femtosecond writing of active optical waveguides with astigmatically shaped beams. *J. Opt. Soc. Am. B* **20**, 1559–1567 (2003).
52. Zoubir, A., Lopez, C., Richardson, M. & Richardson, K. Femtosecond laser fabrication of tubular waveguides in poly(methyl methacrylate). *Opt. Lett.* **29**, 1840–1842 (2004).
53. Sowa, S., Watanabe, W., Tamaki, T., Nishii, J. & Itoh, K. Symmetric waveguides in poly(methyl methacrylate) fabricated by femtosecond laser pulses. *Opt. Express* **14**, 291–297 (2006).
54. Davis, K. M., Miura, K., Sugimoto, N. & Hirao, K. Writing waveguides in glass with a femtosecond laser. *Opt. Lett.* **21**, 1729–1731 (1996).
55. Takeshi, F., Shimon, I., Tomoko, F., Ken, S. & Hideyuki, H. In *Photon Processing in Microelectronics and Photonics III, SPIE, San Jose, California* **5339**, 524–538 (2004).
56. Shah, L., Arai, A. Y., Eaton, S. M. & Herman, P. R. Waveguide writing in fused silica with a femtosecond fiber laser at 522 nm and 1 MHz repetition rate. *Opt. Express* **13**, 1999–2006 (2005).
57. Zhang, H., Eaton, S. M. & Herman, P. R. Low-loss Type II waveguide writing in fused silica with single picosecond laser pulses. *Opt. Express* **14**, 4826–4834 (2006).
58. Tong, L. M., Gattass, R. R., Maxwell, I., Ashcom, J. B. & Mazur, E. Optical loss measurements in femtosecond laser written waveguides in glass. *Opt. Commun.* **259**, 626–630 (2006).
59. Bhardwaj, V. R. *et al.* Femtosecond laser-induced refractive index modification in multicomponent glasses. *J. Appl. Phys.* **97**, 083102 (2005).
60. Nolte, S., Will, M., Burghoff, J. & Tünnemann, A. Femtosecond waveguide writing: A new avenue to three-dimensional integrated optics. *Appl. Phys. A* **77**, 109–111 (2003).
61. Kamata, M., Obara, M., Gattass, R. R., Ceram, L. R. & Mazur, E. Optical vibration sensor fabricated by femtosecond laser micromachining. *Appl. Phys. Lett.* **87**, 051106 (2005).
62. Sikorski, Y. *et al.* Optical waveguide amplifier in Nd-doped glass written with near-IR femtosecond laser pulses. *Electron. Lett.* **36**, 226–227 (2000).
63. Osellame, R. *et al.* Optical gain in Er-Yb doped waveguides fabricated by femtosecond laser pulses. *Electron. Lett.* **38**, 964–965 (2002).
64. Della Valle, G. *et al.* C-band waveguide amplifier produced by femtosecond laser writing. *Opt. Express* **13**, 5976–5982 (2005).
65. Taccheo, S. *et al.* Er: Yb-doped waveguide laser fabricated by femtosecond laser pulses. *Opt. Lett.* **29**, 2626–2628 (2004).
66. Gui, L., Xu, B. X. & Chong, T. C. Microstructure in lithium niobate by use of focused femtosecond laser pulses. *IEEE Photon. Tech. Lett.* **16**, 1337–1339 (2004).
67. Burghoff, J., Grebing, C., Nolte, S. & Tünnemann, A. Efficient frequency doubling in femtosecond laser-written waveguides in lithium niobate. *Appl. Phys. Lett.* **89**, 081108 (2006).
68. Shih, T., Gattass, R. R., Mendonca, C. R. & Mazur, E. Faraday rotation in femtosecond laser micromachined waveguides. *Opt. Express* **15**, 5809–5814 (2007).
69. Minoshima, K., Kowalevich, A. M., Hartl, I., Ippen, E. P. & Fujimoto, J. G. Photonic device fabrication in glass by use of nonlinear materials processing with a femtosecond laser oscillator. *Opt. Lett.* **26**, 1516–1518 (2001).
70. Minoshima, K., Kowalevich, A. M., Ippen, E. P. & Fujimoto, J. G. Fabrication of coupled mode photonic devices in glass by nonlinear femtosecond laser materials processing. *Opt. Express* **10**, 645–652 (2002).
71. Kowalevich, A. M., Sharma, V., Ippen, E. P., Fujimoto, J. G. & Minoshima, K. Three-dimensional photonic devices fabricated in glass by use of a femtosecond laser oscillator. *Opt. Lett.* **30**, 1060–1062 (2005).
72. Marshall, G. D., Ams, M. & Withford, M. J. Direct laser written waveguide-Bragg gratings in bulk fused silica. *Opt. Lett.* **31**, 2690–2691 (2006).
73. Zhang, H. B., Eaton, S. M., Li, J. Z., Nejadmalayeri, A. H. & Herman, P. R. Type II high-strength Bragg grating waveguides photowritten with ultrashort laser pulses. *Opt. Express* **15**, 4182–4191 (2007).
74. Zhang, H., Eaton, S. M. & Herman, P. R. Single-step writing of Bragg grating waveguides in fused silica with an externally modulated femtosecond fiber laser. *Opt. Lett.* **32**, 2559–2561 (2007).
75. Kondo, Y. *et al.* Fabrication of long-period fiber gratings by focused irradiation of infrared femtosecond laser pulses. *Opt. Lett.* **24**, 646–648 (1999).
76. Fertein, E. *et al.* Refractive-index changes of standard telecommunication fiber through exposure to femtosecond laser pulses at 810 nm. *Appl. Opt.* **40**, 3506–3508 (2001).
77. Martinez, A., Dubov, M., Khrushchev, I. & Bennion, I. Direct writing of fibre Bragg gratings by femtosecond laser. *Electron. Lett.* **40**, 1170–1172 (2004).
78. Wikszak, E. *et al.* Erbium fiber laser based on intracore femtosecond-written fiber Bragg grating. *Opt. Lett.* **31**, 2390–2392 (2006).
79. Nikogosyan, D. N. Multi-photon high-excitation-energy approach to fibre grating inscription. *Meas. Sci. Technol.* **18**, R1–R29 (2007).
80. Sun, H. B. & Kawata, S. in *NMR - 3D Analysis - Photopolymerization* Vol. 170 (ed. Lee, S.-K.) 169–273 (Springer, Berlin, 2004).
81. Maruo, S., Nakamura, O. & Kawata, S. Three-dimensional microfabrication with two-photon-absorbed photopolymerization. *Opt. Lett.* **22**, 132–134 (1997).
82. Kawata, S., Sun, H. B., Tanaka, T. & Takada, K. Finer features for functional microdevices. *Nature* **412**, 697–698 (2001).
83. LaFratta, C. N., Fourkas, J. T., Baldacchini, T. & Farrer, R. A. Multiphoton Fabrication. *Angew. Chem. Int. Edn* **46**, 6238–6258 (2007).
84. Sun, H. B., Matsuo, S. & Misawa, H. Three-dimensional photonic crystal structures achieved with two-photon-absorption photopolymerization of resin. *Appl. Phys. Lett.* **74**, 786–788 (1999).
85. Deubel, M. *et al.* Direct laser writing of three-dimensional photonic-crystal templates for telecommunications. *Nature Mater.* **3**, 444–447 (2004).
86. Berns, M. W., Olson, R. S. & Rounds, D. E. *In vitro* production of chromosomal lesions with an argon laser microbeam. *Nature* **221**, 74–75 (1969).
87. Liang, H., Wright, W. H., Cheng, S., He, W. & Berns, M. W. Micromanipulation of chromosomes in Ptk2 cells using laser microsurgery (optical scalpel) in combination with laser-induced optical force (optical tweezers). *Exp. Cell Res.* **204**, 110–120 (1993).
88. Berns, M. W. *et al.* Laser micro-surgery in cell and developmental biology. *Science* **213**, 505–513 (1981).
89. Vogel, A., Noack, J., Huttman, G. & Paltuf, G. Mechanisms of femtosecond laser nanosurgery of cells and tissues. *Appl. Phys. B* **81**, 1015–1047 (2005).
90. König, K., Riemann, I., Fischer, P. & Halhuber, K. H. Intracellular nanosurgery with near infrared femtosecond laser pulses. *Cell. Mol. Biol.* **45**, 195–201 (1999).
91. Watanabe, W. *et al.* Femtosecond laser disruption of subcellular organelles in a living cell. *Opt. Express* **12**, 4203–4213 (2004).
92. Shen, N. *et al.* Ablation of cytoskeletal filaments and mitochondria in live cells using a femtosecond laser nanoscissor. *Mech. Chem. Biosystems* **2**, 17–25 (2005).
93. Supatto, W. *et al.* *In vivo* modulation of morphogenetic movements in *Drosophila* embryos with femtosecond laser pulses. *Proc. Natl Acad. Sci. USA* **102**, 1047–1052 (2005).
94. Yanik, M. F. *et al.* Functional regeneration after laser axotomy. *Nature* **432**, 822 (2004).
95. Chung, S. H., Clark, D. A., Gabel, C. V., Mazur, E. & Samuel, A. D. T. The role of the AFD neuron in *C-elegans* thermotaxis analyzed using femtosecond laser ablation. *Bmc Neuroscience* **7**, 30 (2006).
96. Watanabe, W., Onda, S., Tamaki, T., Itoh, K. & Nishii, J. Space-selective laser joining of dissimilar transparent materials using femtosecond laser pulses. *Appl. Phys. Lett.* **89**, 021106 (2006).
97. Tamaki, T., Watanabe, W., Nishii, J. & Itoh, K. Welding of transparent materials using femtosecond laser pulses. *Jpn J. Appl. Phys.* **44**, L687–L689 (2005).
98. Watanabe, W., Onda, S., Tamaki, T. & Itoh, K. Direct joining of glass substrates by 1 kHz femtosecond laser pulses. *Appl. Phys. B* **87**, 85–89 (2007).
99. Tamaki, T., Watanabe, W. & Itoh, K. Laser micro-welding of transparent materials by a localized heat accumulation effect using a femtosecond fiber laser at 1558 nm. *Opt. Express* **14**, 10460–10468 (2006).
100. Miura, K., Qiu, J. R., Mitsuyu, T. & Hirao, K. Space-selective growth of frequency-conversion crystals in glasses with ultrashort infrared laser pulses. *Opt. Lett.* **25**, 408–410 (2000).
101. Yu, B. *et al.* Study of crystal formation in borate, niobate, and titanate glasses irradiated by femtosecond laser pulses. *J. Opt. Soc. Am. B* **21**, 83–87 (2004).
102. Miura, K., Qiu, J. R., Fujiwara, S., Sakaguchi, S. & Hirao, K. Three-dimensional optical memory with rewriteable and ultrahigh density using the valence-state change of samarium ions. *Appl. Phys. Lett.* **80**, 2263–2265 (2002).
103. Manz, A., Graber, N. & Widmer, H. M. Miniaturized total chemical-analysis systems - A novel concept for chemical sensing. *Sens. Actuators B* **1**, 244–248 (1990).
104. Reyes, D. R., Iossifidis, D., Aurox, P. A. & Manz, A. Micro total analysis systems. 1. Introduction, theory, and technology. *Anal. Chem.* **74**, 2623–2636 (2002).
105. Aurox, P. A., Iossifidis, D., Reyes, D. R. & Manz, A. Micro total analysis systems. 2. Analytical standard operations and applications. *Anal. Chem.* **74**, 2637–2652 (2002).
106. Marcinkiewicz, A. *et al.* Femtosecond laser-assisted three-dimensional microfabrication in silica. *Opt. Lett.* **26**, 277–279 (2001).
107. Kondo, Y., Qiu, J., Mitsuyu, T., Hirao, K. & Yoko, T. Three-dimensional microdrilling of glass by multiphoton process and chemical etching. *Jpn J. Appl. Phys.* **38**, L1146–L1148 (1999).
108. Masuda, M. *et al.* 3-D microstructuring inside photosensitive glass by femtosecond laser excitation. *Appl. Phys. A* **76**, 857–860 (2003).
109. Maselli, V. *et al.* Fabrication of long microchannels with circular cross section using astigmatically shaped femtosecond laser pulses and chemical etching. *Appl. Phys. Lett.* **88**, 191107 (2006).
110. Chiodo, N. *et al.* Imaging of Bloch oscillations in erbium-doped curved waveguide arrays. *Opt. Lett.* **31**, 1651–1653 (2006).
111. Szameit, A. *et al.* Two-dimensional soliton in cubic fs laser written waveguide arrays in fused silica. *Opt. Express* **14**, 6055–6062 (2006).
112. Pierce, J. R. Coupling of modes of propagation. *J. Appl. Phys.* **25**, 179–183 (1954).
113. Belloard, Y., Said, A., Dugan, M. & Bado, P. Fabrication of high-aspect ratio, micro-fluidic channels and tunnels using femtosecond laser pulses and chemical etching. *Opt. Express* **12**, 2120–2129 (2004).

Acknowledgments

The authors would like to acknowledge C. R. Mendonca, J. Dowd, M. Haider-Syed and T. Baldacchini for input on the manuscript. The authors are supported by the Army Research Office under contract W911NF-05-1-0471.

3D Cell-Migration Studies using Two-Photon Engineered Polymer Scaffolds**

By Prakriti Tayalia, Cleber R. Mendonca, Tommaso Baldacchini, David J. Mooney, and Eric Mazur*

Recent research reveals intriguing differences between cell migration in two and three dimensions. Studies of cell migration are important for understanding a variety of physiological and pathological processes such as embryonic development, cancer metastasis, blood vessel formation and remodeling, tissue regeneration, immune surveillance, and inflammation.^[1] Researchers have extensively studied the mechanisms and regulation of cell migration in two-dimensional (2D) cell-culture models, where migration is predominantly a function of adhesion and de-adhesion events and where there are no spatial barriers to the advancing cell body.^[2,3] However, discrepancies between the behavior of cells in culture (2D) and in vivo (3D) indicate it is important to use 3D models to better represent the microenvironment of living tissues with respect to dimensionality, architecture and cell polarity. Unlike cells migrating in 2D, cells in 3D need to overcome the physical resistance provided by the matrix, change shape and morphology, or enzymatically degrade matrix components.^[1,4–6]

Fibrous matrices like collagen, matrigel and fibrinogen derived from tissue are widely used for studying 3D cell migration in vitro.^[6–8] 3D cell tracking has also been done in vivo in live zebrafish embryos.^[9] The natural matrices used for in vitro studies are inherently adhesive and have random pore and mesh sizes. However, these matrices do not allow control

of adhesion, matrix architecture, and mechanical stiffness, and thus it is difficult to determine the effect of each of these parameters on cell migration. Synthetic matrices provide greater control over material properties and cell behavior to provide insight into the complexity of cell-signaling mechanisms. Although techniques like soft lithography, photolithography, and microprinting have been extensively used to study cell behavior on 2D patterned substrates,^[10,11] few tools exist for studying cells in a well-controlled 3D environment. Current fabrication techniques for 3D porous scaffolds, such as solvent casting/particulate leaching, gas foaming, and phase inversion, do not permit precise control of pore size, of pore geometry, and of the spatial distribution of pores, nor is it possible to construct internal channels within the scaffold.^[12–17] Rapid prototyping of scaffolds allows control of complex internal features of scaffolds, but the resolution and smallest feature size is usually constrained by the process parameters and properties of the building materials. For most of the rapid prototyping techniques currently used to fabricate scaffolds, the smallest pore size is about 50–100 μm .^[13,18] Powder-based techniques, such as three-dimensional printing (3DP) and selective laser sintering (SLS), are not suitable for cell studies because it is difficult to remove material trapped in the scaffold structures. Thus, matrices obtained by conventional scaffold fabrication techniques do not provide the precision required to control and understand cell attachment and migration in a 3D environment. Recently, two-photon polymerization was used to create ossicular replacement prostheses and other medical devices with a larger range of sizes, shapes and materials than previously demonstrated with other microfabrication techniques.^[19]

We use two-photon polymerization to precisely control the pore size of a 3D matrix. The technique permits control of architectural parameters like pore size, shape, porosity and permeability down to the submicrometer scale. It is also possible to control the presentation of biochemical and biophysical cues in the matrix to study cell function. We could present different cues by using materials with different mechanical properties or by modifying the material with specific or non-specific cell adhesion peptides. Lutolf et al. have demonstrated that modification of acrylate hydrogels with peptides can be readily achieved.^[20] In this paper we present standard protocols for microfabrication and cell culture, a three-dimensional imaging technique and quantitative analysis method for studying 3D cell migration, and compare cell migration in 2D and 3D.

[*] Prof. E. Mazur, Prof. D. J. Mooney, P. Tayalia
School of Engineering and Applied Sciences, Harvard University
9 Oxford Street, Cambridge, Massachusetts 02138 (USA)
E-mail: mazur@seas.harvard.edu

Dr. C. R. Mendonca
Instituto de Física de São Carlos, Universidade de São Paulo
Caixa Postal 369, 13560-970 São Carlos, SP (Brazil)

Dr. T. Baldacchini
Technology and Applications Center, Newport Corporation
1791 Deere Avenue, Irvine, CA 92606 (USA)

[**] Several people contributed to the work described in this paper. P.T. conceived of the basic idea for this work, designed and carried out the experiments, and analyzed the results. T.B. provided expertise on two-photon polymerization and polymer chemistry. C.M. assisted with the experiments. D.M. and E.M. supervised the research, analysis of the data, and the development of the manuscript. P.T. wrote the first draft of the manuscript; all authors subsequently took part in the revision process and approved the final copy of the manuscript. M. Winkler, J. Dowd and C. Evans provided feedback on the manuscript throughout its development. The research described in this paper was supported by the NSF-sponsored Materials Research Science and Engineering Center under contract DMR-0213805 and NIH under contract R37 DE013033. Supporting Information is available online from Wiley InterScience or from the author.

Three-dimensional microfabrication by two-photon polymerization takes advantage of the spatial selectivity of two-photon absorption^[21] to fabricate 3D polymeric structures of any shape and size with submicrometer resolution.^[22,23] The nonlinear nature of the two-photon absorption process confines the photopolymerization to the focal volume. In the current work, we use a viscous triacrylate two-monomer composition for the fabrication of scaffolds.^[24] This monomer is transparent at the laser wavelength of 800 nm, so that it cross-links only within the focal region where nonlinear absorption occurs. Figure 1a shows a schematic of the set-up. A 76-MHz train of 120-fs laser pulses of 800-nm wavelength is focused through a microscope objective in to the sample. The focal point of the laser beam is translated in the sample to create complex three-dimensional patterns. After the laser exposure is completed, we wash away the unexposed resin with a solvent, leaving behind the 3D interconnected scaffolds fabricated for the current study.

The scaffolds used in this study are interconnected woodpile structures having alternate layers of orthogonal beams in the z -direction (Fig. 1b). Figure 1b defines various parameters of the scaffold design. The pores are square in shape and permit fluid flow and migration of cells. We used four different lateral pore sizes in this study: $A = 12, 25, 52$ and $110 \mu\text{m}$. This range of pore size spans from a little below the size of a single cell (approximately $15 \mu\text{m}$) to ten times the cell size. The lateral beam size is kept fixed at $B = 5 \mu\text{m}$ and the z -distance between parallel beams is kept fixed at $C = 12 \mu\text{m}$ for all scaffolds. The height and width of each scaffold is $D = 100 \mu\text{m}$ and $E = 350 \mu\text{m}$, respectively. Figure 1c is a top view of a 1.75-mm long and 350- μm wide scaffold with a 110- μm pore size. Figure 1d shows a similar scaffold with a 52- μm pore size. Figures 1e and 1f are side views of scaffolds with 25- μm and 52- μm pore sizes, respectively.

We measured the mechanical properties of the photopolymerized triacrylate, from which the scaffolds are fabricated, and confirmed its biocompatibility for cell growth. Using methanol as a solvent, we leach out the unpolymerized monomer from the polymer. After the leaching, we seeded the substrate with cells and observed the cell number to increase (Figs. 1g, 1h), confirming the material to be compatible for cell attachment and cell growth. Figure 1i shows the bulk mechanical stiffness of the polymer after UV photopolymerization as a function of composition of the two monomers in the triacrylate system, before and after solvent leaching. The leaching process does not affect the elastic modulus of the polymer, and the elastic modulus of the polymer system can be varied from 0.1 GPa to 1.2 GPa. This range of values is in agreement with the elastic modulus of microcantilevers prepared by two-photon polymerization of the same monomer mixture.^[25] Thus, regardless of the polymerization process, the polymerized material has similar mechanical properties. We confirmed biocompatibility over the entire range of compositions shown in Fig. 1i.

We studied cell migration in the scaffolds using the human fibrosarcoma cell line HT1080. To minimize photobleaching and the light-induced phototoxic effects of commercially available artificial dyes, we fluorescently labeled the cells by transfecting them with green fluorescent protein (GFP) plasmid. We confirmed that the transfection process does not affect cell motility by comparing cell migration of transfected and untransfected cells. The GFP-labeling permits 3D imaging of cells inside scaffolds using confocal microscopy and also allows

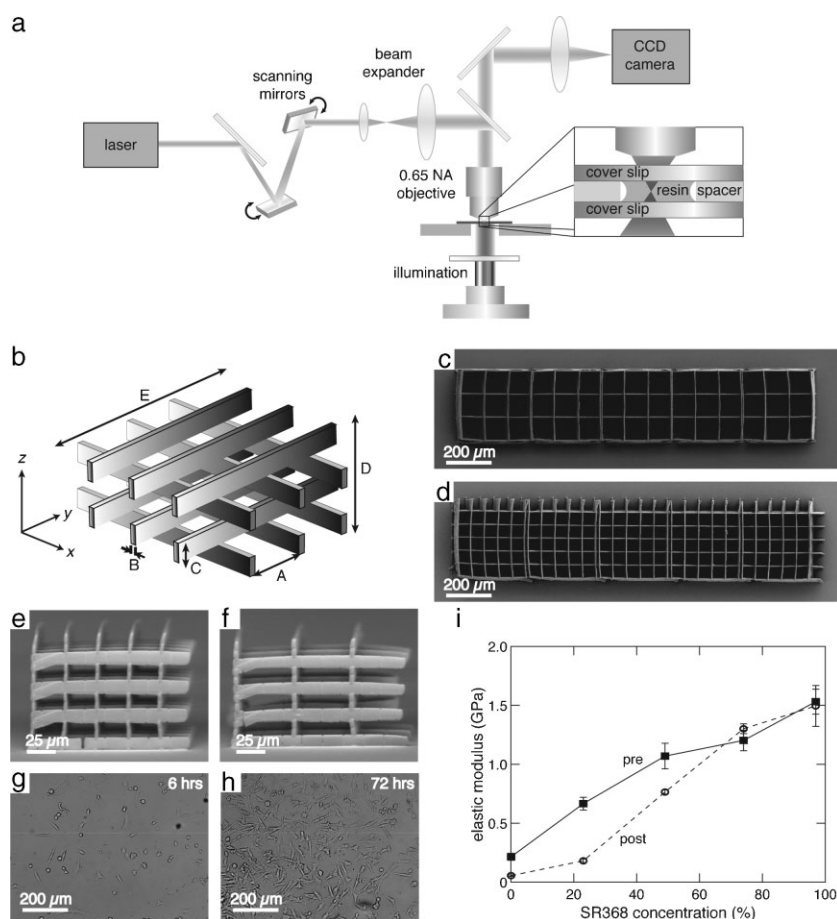


Figure 1. a) Schematic of the laser set-up used for fabrication. b) Schematic of the scaffold design illustrating different parameters of the scaffold. $A = 12, 25, 52$ or $110 \mu\text{m}$; $B = 5 \mu\text{m}$; $C = 12 \mu\text{m}$; $D = 100 \mu\text{m}$; $E = 375 \mu\text{m}$. Top view scanning electron micrographs (SEM) of scaffolds with (c) 110- μm pore size and (d) 52- μm pore size. Side view SEM of (e) 25- μm and (f) 52- μm pore-sized scaffolds. Optical micrographs showing increase in the number of cells attached to a polymerized triacrylate 2D disc (g) 6 h and (h) 72 h after cell seeding. i) Bulk elastic modulus of UV photopolymerized triacrylate measured as a function of monomer concentration (solid line: before solvent treatment; broken line: after solvent treatment).

long-term live cell imaging. Periodically, we filter out bright fluorescent cells from dim fluorescent population using fluorescence activated cell sorting to maintain overall high fluorescence intensity for long-term imaging.

We seed the fluorescently-labeled cells onto the scaffolds at a density of $500\,000\text{ cells mL}^{-1}$. Figure 2a shows a top-view bright-field image of cells taken 5 h after seeding inside a $52\text{-}\mu\text{m}$ pore-sized scaffold. Initially, the cells are located only on the cover slip, but start moving in 3D after a few hours. One day after cell seeding, we image the scaffolds using a $20\times$ objective with a numerical aperture of 0.75 on a spinning-disc confocal microscope with a heated stage maintained at physiological conditions of 37°C , $5\%\text{ CO}_2$, and humidified atmosphere. For each experiment, we image z stacks (images with same xy positions but different z positions) at regular intervals. We record images in differential interference contrast and fluorescence imaging modes at 10-min intervals for a period of 8 h. To compare 2D and 3D migration, we prepare 2D films of UV polymerized triacrylate polymer on glass and treat them similarly for removal of monomer toxicity. We seed cells on the 2D substrates and image them in the same way as described above.

To track cell movement, we used commercial 3D imaging software. Based on the intensity and size of a cell, the software assigns it an x , y , and z coordinate at each instant. To characterize cell migration, we calculate the average speed, probability of movement, and motion persistence of the cells in the x , y , and z directions. Speed is defined as the sum of all the distances between subsequent images divided by the total time over which the imaging took place (10 min). Probability of movement is the number of imaging intervals during which the

cell's displacement is larger than $1\text{ }\mu\text{m}$ divided by 48 (the total number of imaging intervals). Motion persistence is defined as the number of imaging intervals during which the cell's displacement is larger than $1\text{ }\mu\text{m}$ in the same direction for three consecutive time intervals divided by the total number of imaging intervals. This last parameter is a measure of the cell's tendency to continue moving in a certain direction.

We find that the cells readily move in three-dimensions inside the scaffold, as seen from a 3D-rendered image of GFP labeled cells (Fig. 2b) and the movie in Supporting Information. The cells attach and move predominantly along the beams in the $110\text{-}\mu\text{m}$ scaffold (Fig. 2c), while they occupy the entire pore in the smaller scaffolds (see movies in Supporting Information). Also, the cells are more uniformly dispersed inside the $52\text{-}\mu\text{m}$ scaffold than inside the 25- and $12\text{-}\mu\text{m}$ scaffold (Figs. 2d and 2f, respectively). Figure 3a depicts a typical track of the motion of a cell in a $25\text{-}\mu\text{m}$ scaffold. The overall mean speed of the cells is higher in the scaffold than it is on 2D substrate (Fig. 3b), but the lateral speed and persistence in the x and y directions are the same (Fig. 3c). In contrast, Figure 3d shows that the probability of movement in the x and y directions is lower in the scaffold than it is on 2D substrate, where cells encounter fewer obstructions. As the pore size is increased, the overall mean speed increases, but the persistence and probability of movement remain the same.

The higher value of the overall mean cell speed 3D compared to that in 2D is likely due to the additional degree of freedom for cell movement (Fig. 3b). In contrast, for collagen matrices the cell migration speed is lower in 3D than it is on a 2D substrate.^[26] The collagen has pore sizes from nanometers to micrometers, but is degradable and softer than our matrix system. To migrate through the collagen matrix, the cells must therefore degrade the collagen or modify their shape. Our scaffolds, on the other hand, are stiff non-degradable polymer matrices that do not allow matrix proteolysis and only allow cell shape change and adhesion-deadhesion events for any movement.

The random-motion track in Fig. 3a confirms the interconnectedness of the 3D scaffolds and shows that the cell has freedom of movement along all three coordinate axes for a scaffold with pore size of $25\text{ }\mu\text{m}$. However, the decrease in cell distribution uniformity with pore size observed in Figs. 2c–f indicates that the matrix obstructs the cells and prevents their free movement inside smaller pore-size scaffolds. The monotonic increase in overall mean speed with pore size (Fig. 3b) supports this interpretation. Earlier studies of collagen matrices show that pore size decreases as collagen concentration increases.^[8,27,28] Modeling suggests that the cell speed should depend parabolically on pore size with a maximum at a pore size of

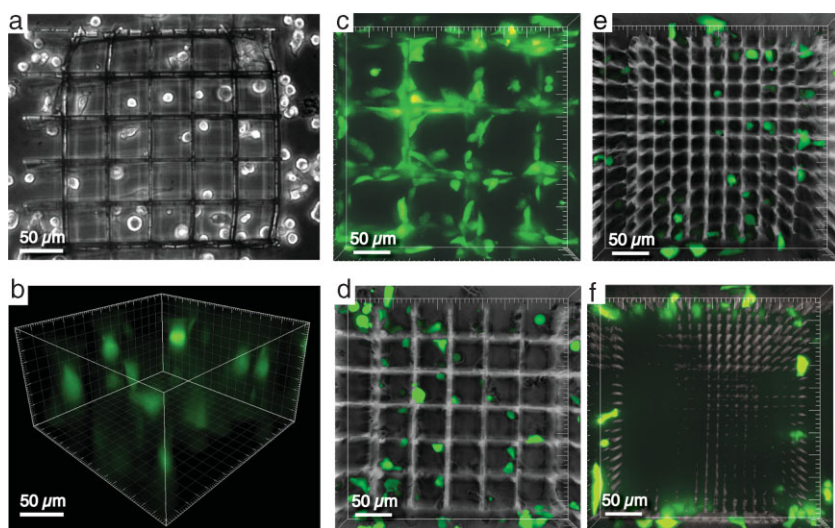


Figure 2. a) Brightfield optical image showing top view of cells inside a $52\text{-}\mu\text{m}$ pore-sized scaffold 5 h after seeding cells. b) Fluorescence image showing isometric 3D rendered view of HT1080 cells inside a scaffold 24 h after seeding cells c–f) Top view overlay of fluorescence and differential interference contrast images of cells in 110 , 52 , 25 and $12\text{-}\mu\text{m}$ pore-sized scaffolds showing non-uniformity in the distribution of cells in different matrices owing to variations in physical obstruction.

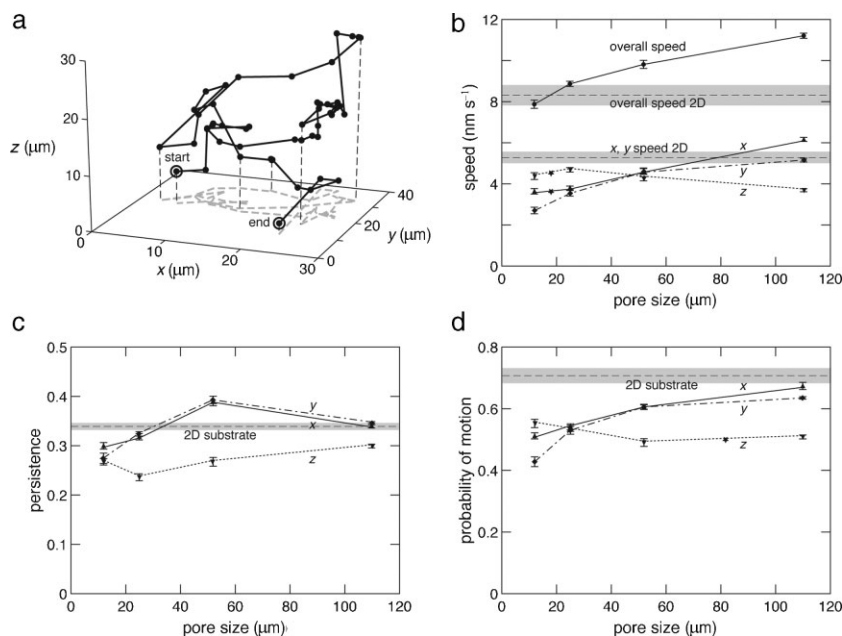


Figure 3. a) Typical track of a cell in a 25- μm scaffold. b) Overall mean speed and directional speed, (c) persistence and (d) probability of movement as a function of pore size. Data points: 3D matrices; dashed lines: values obtained on 2D substrates. The error bars represent the standard error around the mean value. Statistical significance was evaluated for difference in values between adjacent pore-sized scaffolds. It was also evaluated between 2D and 110- μm pore-sized scaffold. The difference between adjacent data points has p values of less than 0.05 for all pairs except those marked by an asterisk (*).

approximately 25 μm .^[28] We do not see such a parabolic trend; instead cell speed continues to increase up to the largest pore size (110 μm), where the cells predominantly migrate along beams (Fig. 2c) without encountering many obstructions. Contrary to the prediction of models for a non-degradable matrix,^[8,28] the migration speed of the cells in the 12- μm pore-sized scaffold is not zero. We observe that the cells change their shape and manage to squeeze through small pores (see Supporting Information), in accordance with observations by Wolf et al.^[5]

To summarize, we developed a model three-dimensional (3D) extracellular matrix that provides precise and independent control of architectural parameters and that can be used for controlled cell adhesion and migration studies. We find that the 3D environment produces higher cell speeds than a 2D substrate. As the pore size of the 3D matrix is decreased, we observe a decrease in mean speed due to obstruction from the matrix. The fabrication and analysis techniques we describe in this paper open the door to systematic studies of the effects of mechanical properties, adhesion peptide concentration, and biodegradability on cell migration in three-dimensional environments.

Experimental

Materials: We purchased triacrylate monomers tris (2-hydroxy ethyl) isocyanurate triacrylate (SR368) and ethoxylated (6) trimethy-

lolpropane triacrylate (SR499) from Sartomer Company, Inc and the photoinitiator, Lucirin-TPOL from BASF. We purchased the cell line HT1080 from ATCC. Invitrogen supplied all the cell culture media. We purchased the GFP plasmid from Clontech.

Scaffold Fabrication: We clean a cover-glass and silanize it with acryloxy-propyl-trimethoxy silane to facilitate the adhesion of a polymerized triacrylate film on the glass surface. The composition of liquid resin used for photopolymerization is a 48:49 ratio of the two triacrylate monomers SR368 and SR499, respectively, and 3% of the photoinitiator Lucirin-TPOL. We spin coat a thin film of the resin on a silanized cover-glass and polymerize it under a UV lamp for 10 min. We use this sample for 2D cell migration studies. For fabrication of 3D scaffolds, we place a drop of resin on a silanized acrylate-coated cover glass positioned on a sample stage and irradiate it with 130-fs, 800-nm laser pulses from a Ti-sapphire laser oscillator operating at a 80 MHz repetition rate (Fig. 1a). We use a 40 \times objective with numerical aperture 0.65 to focus the laser beam inside the resin. We fabricate the scaffolds by scanning the laser beam using a pair of galvanometer mirrors and moving the computer-controlled sample stage in the x, y and z directions. An increase in the index of refraction (1.522 vs. 1.493) of the polymer after photopolymerization allows visualizing the fabrication process with a charge coupled device camera using transmitted white light. The unpolymerized resin is washed off in ethanol leaving behind the 3D microfabricated scaffolds.

Mechanical Characterization: The bulk mechanical stiffness of the photopolymer is measured in a tensile testing machine. The specimen for the tensile test is a “dog-bone” shaped specimen made by polymerizing the liquid monomer/s under UV light for 10 min using a silicone mold sandwiched between two glass plates. The shape and dimensions of the dog-bone complies with ISO 527-2 for plastics and measures 75 mm long with the center section 5 mm wide by 1 mm thick by 30 mm long. We test three samples for each composition to add statistical significance to the measurements. We do the tests before and after solvent treatment to study the effect of the leaching of unpolymerized monomers on the mechanical stiffness of the photopolymer.

Cell Culture: We culture HT1080 fibrosarcoma cells in Eagle’s Minimum Essential Medium (EMEM) supplemented with 10% fetal bovine serum (FBS) and 1% antibiotics (penicillin and streptomycin).

Cell Compatibility: We use silicone isolators as molds sandwiched between two glass slides to UV polymerize the triacrylate resin in the shape of discs 20 mm in diameter and 1 mm thick. We keep these discs in methanol placed on a shaker for 3 days to leach out the unpolymerized, toxic monomer. Then we place these polymer discs inside a non-tissue culture treated 12 well plate and seed HT1080 fibrosarcoma cells at a density of 100 cells per mm². We monitor cell growth by taking images every few hours and measure cell proliferation by detaching the cells using trypsin and counting them at different times using a cell counter. Same procedure of solvent leaching is used for 2D substrates and 3D scaffolds.

GFP Transfection: For transfection of cells, we seed 5×10^5 cells in a six-well plate in an EMEM medium with 10% FBS without any antibiotics. We dilute 2 μg of GFP plasmid in 250 μL of low serum medium (Optimem) and 2.5 μL of Lipofectamine-2000 in another 250 μL Optimem. We mix the two solutions and incubate them at room temperature for 45 min to allow lipid-DNA complexes to form. After 24 h, we replace the cell medium with 500 μL Optimem and add the lipid-DNA complex to each well. After incubating the cells for 5 h at

37 °C in a 5% CO₂ incubator, we add medium with 10% FBS to the cells and allow them to incubate for another 24–36 h. At the end of 36 h, we sort and resort the cells a few times using a fluorescence assisted cell-sorting instrument to obtain a transient GFP-transfected population of cells.

Cell Migration Studies: We seed the scaffolds at a cell density of 500,000 cells/mL and allow the cells to attach and proliferate for 24 h before starting live imaging. Using 3D rendering and tracking software Imaris from Bitplane, Inc, we analyze the 3D time-lapse images for each experiment. After we adjust the overall threshold of the image, the software assigns coordinates to each cell and tracks them over time. From these data we obtain the overall mean speed and the speed in the *x*, *y*, and *z* directions. In calculating values for persistence and probability of movement of cells, we set a threshold value of 1 μm to differentiate between moving and non-moving cells. This value is well above the minimum temporal and spatial resolution of the imaging system.

Received: May 13, 2008

Revised: August 21, 2008

Published online: October 15, 2008

- [1] S. Even-Ram, K. M. Yamada, *Curr. Opin. Cell Biol.* **2005**, *17*, 524.
- [2] R. B. Dickinson, R. T. Tranquillo, *AiChE J.* **1993**, *39*, 1995.
- [3] B. D. Harms, G. M. Bassi, A. R. Horwitz, D. A. Lauffenburger, *Biophys. J.* **2005**, *88*, 1479.
- [4] E. Cukierman, R. Pankov, D. R. Stevens, K. M. Yamada, *Science* **2001**, *294*, 1708.
- [5] K. Wolf, I. Mazo, H. Leung, K. Engelke, U. H. von Andrian, E. I. Deryugina, A. Y. Strongin, E. B. Brocker, P. Friedl, *J. Cell Biol.* **2003**, *160*, 267.
- [6] P. Friedl, K. Wolf, *Nat. Rev. Cancer* **2003**, *3*, 362.
- [7] F. Grinnell, L. B. Rocha, C. Iucu, S. Rhee, H. M. Jiang, *Exp. Cell Res.* **2006**, *312*, 86.
- [8] M. H. Zaman, L. M. Trapani, A. Siemeski, D. MacKellar, H. Y. Gong, R. D. Kamm, A. Wells, D. A. Lauffenburger, P. Matsudaira, *Proc. Natl. Acad. Sci. USA* **2006**, *103*, 10889.
- [9] C. Melani, M. Campana, B. Lombardot, B. Rizzi, F. Veronesi, C. Zanella, P. Bourguine, K. Mikula, N. Peyri  ras, A. Sarti, *Conf. Proc. IEEE Eng. Med. Biol. Soc.* **2007**, 2007, 1631.
- [10] S. N. Bhatia, U. J. Balis, M. L. Yarmush, M. Toner, *Biotechnol. Prog.* **1998**, *14*, 378.
- [11] C. S. Chen, M. Mrksich, S. Huang, G. M. Whitesides, D. E. Ingber, *Science* **1997**, *276*, 1425.
- [12] C. K. Chua, K. F. Leong, C. M. Cheah, S. W. Chua, *Int. J. Adv. Manuf. Technol.* **2003**, *21*, 291.
- [13] D. W. Huttmacher, *Biomaterials* **2000**, *21*, 2529.
- [14] E. Sachlos, J. T. Czernuszka, *Eur. Cell. Mater.* **2003**, *5*, 29.
- [15] P. Sarazin, X. Roy, B. D. Favis, *Biomaterials* **2004**, *25*, 5965.
- [16] T. Weigel, G. Schinkel, A. Lendlein, *Expert Rev. Med. Devices* **2006**, *3*, 835.
- [17] D. W. Huttmacher, *J. Biomater. Sci. Polym. Ed.* **2001**, *12*, 107.
- [18] M. H. Too, K. F. Leong, C. K. Chua, Z. H. Du, S. F. Yang, C. M. Cheah, S. L. Ho, *Int. J. Adv. Manuf. Technol.* **2002**, *19*, 217.
- [19] A. Ovsianikov, B. Chichkov, O. Adunka, H. Pillsbury, A. Doraiswamy, R. J. Narayan, *Appl. Surf. Sci.* **2007**, *253*, 6603.
- [20] M. P. Lutolf, J. A. Hubbell, *Nat. Biotechnol.* **2005**, *23*, 47.
- [21] W. Denk, J. H. Strickler, W. W. Webb, *Science* **1990**, *248*, 73.
- [22] B. H. Cumpston, S. P. Ananthavel, S. Barlow, D. L. Dyer, J. E. Ehrlich, L. L. Erskine, A. A. Heikal, S. M. Kuebler, I. Y. S. Lee, D. McCord-Maughon, J. Q. Qin, H. Rockel, M. Rumi, X. L. Wu, S. R. Marder, J. W. Perry, *Nature* **1999**, *398*, 51.
- [23] S. Maruo, O. Nakamura, S. Kawata, *Opt. Lett.* **1997**, *22*, 132.
- [24] T. Baldacchini, C. N. LaFratta, R. A. Farrer, M. C. Teich, B. E. A. Saleh, M. J. Naughton, J. T. Fourkas, *J. Appl. Phys.* **2004**, *95*, 6072.
- [25] Z. Bayindir, Y. Sun, M. J. Naughton, C. N. LaFratta, T. Baldacchini, J. T. Fourkas, J. Stewart, B. E. A. Saleh, M. C. Teich, *Appl. Phys. Lett.* **2005**, *86*.
- [26] S. Hazgui, N. Bonnet, J. Cutrona, B. Nawrocki-Raby, M. Polette, L. Chouchane, P. Birembaut, J. M. Zahm, *Am. J. Physiol. Cell Physiol.* **2005**, *289*, C1547.
- [27] S. Sun, J. Wise, M. Cho, *Tissue Eng.* **2004**, *10*, 1548.
- [28] M. H. Zaman, P. Matsudaira, D. A. Lauffenburger, *Ann. Biomed. Eng.* **2007**, *35*, 91.

Femtosecond laser waveguide micromachining of PMMA films with azoaromatic chromophores

C. R. Mendonca^{1,2}, L. R. Cerami¹, T. Shih¹, R. W. Tilghman¹, T. Baldacchini¹, and E. Mazur^{1*}

¹Department of Physics and Harvard School of Engineering and Applied Sciences,
Harvard University, 9 Oxford Street, Cambridge, Massachusetts 02138

²Instituto de Física de São Carlos, Universidade de São Paulo, Caixa Postal 369, 13560-970 São Carlos, SP, Brazil

*Corresponding Author: mazur@physics.harvard.edu

Abstract: We report on the femtosecond-laser micromachining of poly(methyl methacrylate) (PMMA) films doped with nonlinear azoaromatic chromophores: Disperse Red 1, Disperse Red 13 and Disperse Orange 3. We study the conditions for controlling chromophore degradation during the micromachining of PMMA doped with each chromophore. Furthermore, we successfully used fs-micromachining to fabricate optical waveguides within a bulk sample of PMMA doped with these azochromophores.

©2008 Optical Society of America

OCIS codes: (350.3390) Laser processing of materials; (320.7090) Ultrafast lasers; (160.4890) Organic materials; (130.5460) Polymer waveguides.

References and links

1. K. M. Davis, K. Miura, N. Sugimoto, and K. Hirao, "Writing waveguides in glass with a femtosecond laser," *Opt. Lett.* **21**, 1729-1731 (1996).
2. R. R. Gattass, L. R. Cerami, and E. Mazur, "Micromachining of bulk glass with bursts of femtosecond laser pulses at variable repetition rates," *Opt. Express* **14**, 5279-5284 (2006).
3. K. Kamada, K. Ohta, I. Yoichiro, and K. Kondo, "Two-photon absorption properties of symmetric substituted diacetylene: drastic enhancement of the cross section near the one-photon absorption peak," *Chem. Phys. Lett.* **372**, 386-393 (2003).
4. K. Minoshima, A. M. Kowalevich, I. Hartl, E. P. Ippen, and J. G. Fujimoto, "Photonic device fabrication in glass by use of nonlinear materials processing with a femtosecond laser oscillator," *Opt. Lett.* **26**, 1516-1518 (2001).
5. C. B. Schaffer, A. Brodeur, J. F. Garcia, and E. Mazur, "Micromachining bulk glass by use of femtosecond laser pulses with nanojoule energy," *Opt. Lett.* **26**, 93-95 (2001).
6. Y. Sikorski, A. A. Said, P. Bado, R. Maynard, C. Florea, and K. A. Winick, "Optical waveguide amplifier in Nd-doped glass written with near-IR femtosecond laser pulses," *Electron. Lett.* **36**, 226-227 (2000).
7. L. Sudrie, M. Franco, B. Prade, and A. Mysyrewicz, "Writing of permanent birefringent microlayers in bulk fused silica with femtosecond laser pulses," *Opt. Commun.* **171**, 279-284 (1999).
8. A. M. Kowalevich, T. R. Schibli, F. X. Kartner, and J. G. Fujimoto, "Ultralow-threshold Kerr-lens mode-locked Ti: Al₂O₃ laser," *Opt. Lett.* **27**, 2037-2039 (2002).
9. A. M. Kowalevich, V. Sharma, E. P. Ippen, J. G. Fujimoto, and K. Minoshima, "Three-dimensional photonic devices fabricated in glass by use of a femtosecond laser oscillator," *Opt. Lett.* **30**, 1060-1062 (2005).
10. K. Miura, J. R. Qiu, H. Inouye, T. Mitsuyu, and K. Hirao, "Photowritten optical waveguides in various glasses with ultrashort pulse laser," *Appl. Phys. Lett.* **71**, 3329-3331 (1997).
11. Y. Nasu, M. Kohtoku, and Y. Hibino, "Low-loss waveguides written with a femtosecond laser for flexible interconnection in a planar light-wave circuit," *Opt. Lett.* **30**, 723-725 (2005).
12. S. Nolte, M. Will, J. Burghoff, and A. Tuennermann, "Femtosecond waveguide writing: a new avenue to three-dimensional integrated optics," *Appl. Phys. A-Mater. Sci. Process.* **77**, 109-111 (2003).
13. R. Osellame, S. Taccheo, M. Marangoni, R. Ramponi, P. Laporta, D. Polli, S. De Silvestri, and G. Cerullo, "Femtosecond writing of active optical waveguides with astigmatically shaped beams," *J. Opt. Soc. Am. B.* **20**, 1559-1567 (2003).
14. T. Shih, R. R. Gattass, C. R. Mendonca, and E. Mazur, "Faraday rotation in femtosecond laser micromachined waveguides," *Opt. Express* **15**, 5809-5814 (2007).
15. A. M. Streltsov, and N. F. Borrelli, "Fabrication and analysis of a directional coupler written in glass by nanojoule femtosecond laser pulses," *Opt. Lett.* **26**, 42-43 (2001).
16. G. J. Wang, Y. N. He, X. G. Wang, and L. Jiang, "Self-assembly and optical properties of poly(acrylic acid)-based azo polyelectrolyte," *Thin Solid Films* **458**, 143-148 (2004).

17. W. Watanabe, T. Asano, K. Yamada, K. Itoh, and J. Nishii, "Wavelength division with three-dimensional couplers fabricated by filamentation of femtosecond laser pulses," *Opt. Lett.* **28**, 2491-2493 (2003).
18. M. Will, S. Nolte, B. N. Chichkov, and A. Tunnermann, "Optical properties of waveguides fabricated in fused silica by femtosecond laser pulses," *Appl. Opt.* **41**, 4360-4364 (2002).
19. K. Yamada, W. Watanabe, T. Toma, K. Itoh, and J. Nishii, "In situ observation of photoinduced refractive-index changes in filaments formed in glasses by femtosecond laser pulses," *Opt. Lett.* **26**, 19-21 (2001).
20. Y. Li, K. Yamada, T. Ishizuka, W. Watanabe, K. Itoh, and Z. X. Zhou, "Single femtosecond pulse holography using polymethyl methacrylate," *Opt. Express* **10**, 1173-1178 (2002).
21. P. J. Scully, D. Jones, and D. A. Jaroszynski, "Femtosecond laser irradiation of polymethylmethacrylate for refractive index gratings," *J. Opt. A Pure Appl. Opt.* **5**, S92-S96 (2003).
22. S. Sowa, W. Watanabe, J. Nishii, and K. Itoh, "Filamentary cavity formation in poly(methyl methacrylate) by single femtosecond pulse," *Appl. Phys. A: Mater. Sci. Process.* **81**, 1587-1590 (2005).
23. S. Sowa, W. Watanabe, T. Tamaki, J. Nishii, and K. Itoh, "Symmetric waveguides in poly(methyl methacrylate) fabricated by femtosecond laser pulses," *Opt. Express* **14**, 291-297 (2006).
24. D. B. Wolfe, J. B. Ashcom, J. C. Hwang, C. B. Schaffer, E. Mazur, and G. M. Whitesides, "Customization of poly(dimethylsiloxane) stamps by micromachining using a femtosecond-pulsed laser," *Adv. Mater.* **15**, 62-65 (2003).
25. K. Yamasaki, S. Juodkazis, M. Watanabe, H. B. Sun, S. Matsuo, and H. Misawa, "Recording by microexplosion and two-photon reading of three-dimensional optical memory in polymethylmethacrylate films," *Appl. Phys. Lett.* **76**, 1000-1002 (2000).
26. A. Zoubir, C. Lopez, M. Richardson, and K. Richardson, "Femtosecond laser fabrication of tubular waveguides in poly(methyl methacrylate)," *Opt. Lett.* **29**, 1840-1842 (2004).
27. L. Eldada, and L. W. Shacklette, "Advances in polymer integrated optics," *IEEE J. Sel. Top. Quantum Electron.* **6**, 54-68 (2000).
28. S. Katayama, M. Horiike, K. Hirao, and N. Tsutsumi, "Structure induced by irradiation of femtosecond laser pulse in dyed polymeric materials," *J. Polym. Sci. Pt. B-Polym. Phys.* **40**, 2800-2806 (2002).
29. J. H. Si, J. R. Qiu, and K. Hirao, "Photofabrication of periodic microstructures in azodye-doped polymers by interference of laser beams," *Appl. Phys. B: Lasers Opt.* **75**, 847-851 (2002).
30. J. H. Si, J. R. Qiu, J. F. Zhai, Y. Q. Shen, and K. Hirao, "Photoinduced permanent gratings inside bulk azodye-doped polymers by the coherent field of a femtosecond laser," *Appl. Phys. Lett.* **80**, 359-361 (2002).
31. J. F. Zhai, Z. Q. Shen, J. H. Si, J. R. Qiu, and K. Hirao, "The fabrication of permanent holographic gratings in bulk polymer medium by a femtosecond laser," *J. Phys. D-Appl. Phys.* **34**, 3466-3469 (2001).
32. Y. Q. Shi, C. Zhang, H. Zhang, J. H. Bechtel, L. R. Dalton, B. H. Robinson, and W. H. Steier, "Low (sub-1-volt) halfwave voltage polymeric electro-optic modulators achieved by controlling chromophore shape," *Science* **288**, 119-122 (2000).
33. M. Jager, G. I. Stegeman, S. Yilmaz, W. Wirges, W. Brinker, S. Bauer-Gogonea, S. Bauer, M. Ahlheim, M. Stahelin, B. Zysset, F. Lehr, M. Diemeer, and M. C. Flipse, "Poling and characterization of polymer waveguides for modal dispersion phase-matched second-harmonic generation," *J. Opt. Soc. Am. B.* **15**, 781-788 (1998).
34. A. Natansohn, S. Xie, and P. Rochon, "Azo Polymers for Reversible Optical Storage.2. Poly 4'-2-(Acryloyloxy)Ethyl Ethylamino -2-Chloro-4-Nitroazobenzene," *Macromolecules* **25**, 5531-5532 (1992).
35. P. Rochon, J. Gosselin, A. Natansohn, and S. Xie, "Optically Induced and Erased Birefringence and Dichroism in Azoaromatic Polymers," *Appl. Phys. Lett.* **60**, 4-5 (1992).
36. L. Antonov, K. Kamada, K. Ohta, and F. S. Kamounah, "A systematic femtosecond study on the two-photon absorbing D-pi-A molecules-pi-bridge nitrogen insertion and strength of the donor and acceptor groups," *Phys. Chem. Chem. Phys.* **5**, 1193-1197 (2003).
37. L. De Boni, L. Misoguti, S. C. Zilio, and C. R. Mendonca, "Degenerate Two-Photon Absorption Spectra in Azoaromatic Compounds," *Chem. Phys. Chem.* **6**, 1121-1125 (2005).
38. L. De Boni, J. J. Rodrigues, D. S. dos Santos, C. Silva, D. T. Balogh, O. N. Oliveira, S. C. Zilio, L. Misoguti, and C. R. Mendonca, "Two-photon absorption in azoaromatic compounds (vol 361, pg 209, 2002)," *Chem. Phys. Lett.* **374**, 684-684 (2003).
39. D. W. Fradin, and M. Bass, "Comparison of Laser-Induced Surface and Bulk Damage," *Appl. Phys. Lett.* **22**, 157-159 (1973).
40. A. Galvan-Gonzalez, M. Canva, G. I. Stegeman, L. Sukhomlinova, R. J. Twieg, K. P. Chan, T. C. Kowalczyk, and H. S. Lackritz, "Photodegradation of azobenzene nonlinear optical chromophores: the influence of structure and environment," *J. Opt. Soc. Am. B.* **17**, 1992-2000 (2000).
41. A. Galvan-Gonzalez, M. Canva, G. I. Stegeman, R. Twieg, K. P. Chan, T. C. Kowalczyk, X. Q. Zhang, H. S. Lackritz, S. Marder, and S. Thayumanavan, "Systematic behavior of electro-optic chromophore photostability," *Opt. Lett.* **25**, 332-334 (2000).
42. A. Galvan-Gonzalez, M. Canva, G. I. Stegeman, R. Twieg, T. C. Kowalczyk, and H. S. Lackritz, "Effect of temperature and atmospheric environment on the photodegradation of some Disperse Red 1-type polymers," *Opt. Lett.* **24**, 1741-1743 (1999).

1. Introduction

Femtosecond micromachining of transparent materials allow the fabrication of waveguides within a material volume without damaging its surface [1-7]. Femtosecond laser micromachining has been used in a wide variety of glasses to fabricate waveguide-based photonic devices, including interferometers, amplifiers, resonators, waveguide couplers, and switches [1, 3-19]. In the last five years, this technique has been used to fabricate devices in polymers [20-26]. Polymers are of interest for photonic components because they are cheaper and easier to manufacture than glass, and the optical properties of polymers can be tailored by chemical synthesis or by doping, allowing easy customization for specific applications.

Because of its high transmission in the visible and near-infrared [27], poly(methyl methacrylate) (PMMA) is one of the most widely used polymers for optical components. Previous work has shown fabrication of waveguides in pure PMMA via femtosecond micromachining [20-23, 25, 26] and structural modifications in azo-doped polymers by amplified femtosecond laser pulses [28-31]. However, there is no work on oscillator-only micromachining of waveguides in PMMA doped with optically active organic molecules. In this paper, we investigate femtosecond laser micromachining in PMMA doped with chromophores Disperse Red 1 (DR1), Disperse Red 13 (DR13) and Disperse Orange 3 (DO3). Because of the molecular structures of these chromophores (Fig. 1), these molecules are often referred to as azoaromatic chromophores, or azochromophores. These azochromophores possess interesting linear and nonlinear optical properties, which can be exploited for electro-optic modulators [32], second-harmonic generation [33], and birefringent devices [34, 35]. We determine the threshold energy for polymer modification, and demonstrated that the micromachining results from two-photon absorption. We also quantify the azochromophore photobleaching during microfabrication by measuring the sample absorption spectrum before and after laser irradiation. Finally, we present the first demonstration of waveguide fabrication within the bulk of PMMA doped with azochromophores.

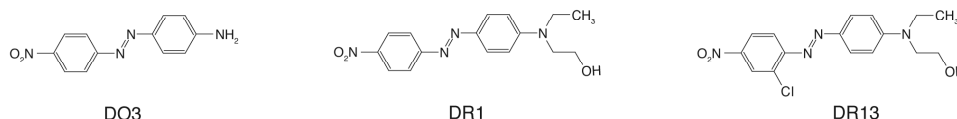


Fig. 1. Molecular structure of (a) DO3, (b) DR1, and (c) DR13.

2. Experimental

The DR1 (4-nitro-4'-[N-ethyl-N-(2-hydroxyethyl)-amino]azobenzene), DR13 (4-nitro-1'-chloro-4'-[N-ethyl-N-(2-hydroxyethyl)-amino]azobenzene) and DO3 (4-(4-nitrophenylazo)aniline) were purchased from Aldrich and used as received. PMMA with a molecular weight of 350,000 g/mol was used for sample preparation without further purification.

We spin-coated films of 5% (by weight) PMMA chloroform solution containing the dissolved azochromophores onto glass slides. The concentration of the azochromophores in the polymer films ranged from 1% to 20%. The resulting film thicknesses were measured with a profilometer and ranged between 3 to 5 mm. For the waveguide fabrication, we prepared thicker samples (2 mm) by casting multiple layers of chloroform solution containing both the polymer and the azochromophores. To determine the optical properties of the doped films, we measured their absorbance from 350 nm to 800 nm with a spectrophotometer.

The PMMA-doped sample was micromachined using 130-fs, 800-nm laser pulses with pulse energies ranging from 0.01 nJ to 0.2 nJ from a Kerr-lens mode-locked oscillator operating at a 76-MHz repetition rate. The pulses were focused through a 0.65-NA microscope objective into the doped films, which were translated at speeds ranging from 5 $\mu\text{m/s}$ to 75 $\mu\text{m/s}$ with respect to the laser beam. Waveguides were written along the entire 5-mm length of the sample, and spaced by 200 μm to prevent crosstalk between them. After micromachining, the ends of the sample were polished to allow coupling of light into the

waveguides. HeNe laser light at 632.8 nm was coupled into and out of the waveguide using two 10× microscope objectives and an iris blocked any scattered light at the exit of the second objective lens. The resulting structures were imaged by transmission optical microscopy to determine their size and shape.

3. Results

The solid lines in Fig. 2 show the absorption spectra of 3-μm thick PMMA films containing 3.5% of DO3, DR1, and DR13. The spectra exhibit absorption bands centered between 440 nm and 515 nm, which correspond to the $\pi \rightarrow \pi^*$ electronic transition of the azochromophores. The samples are completely transparent in the near infrared region, where the micromachining is carried out.

For each sample, we determined the threshold energy at which a change occurs in the PMMA films containing various % of DO3, DR1, and DR13 as a result of the focusing of the Ti:sapphire laser beam into the sample. We used a CCD camera to monitor the sample transmission in real time as we micromachined the material. Figure 3 shows the threshold energy as we vary the concentration of each azochromophore in the sample. For all samples, we see that the threshold energy decreases as the azochromophore concentration increases. We also observe that the threshold energy is highest for DO3, followed by DR1, and DR13 respectively. For instance, with an azochromophore concentration of 1.0%, the sample doped with DO3 has the highest modification energy at 0.17 nJ, DR1 has the next highest energy at 0.11 nJ, and DR13 requires the least energy at 0.05 nJ. This trend is most pronounced for azochromophore concentrations up to 4%. At higher concentrations, the threshold energy is so small that it is hard to distinguish the value from experimental noise. The threshold energy for each sample of a fixed concentration scales very well with the two-photon photon absorption cross-section of the azochromophores; DO3, DR1 and DR13 present two-photon absorption cross-section of 35, 75 and 130 GM, respectively, at 800 nm [36-38]. This result indicates that micromachining in the doped polymers is a two-photon induced process. We also determined the threshold for pure PMMA to be 0.54 nJ. Above this threshold, micromachining of the doped samples results in carbonization of the sample.

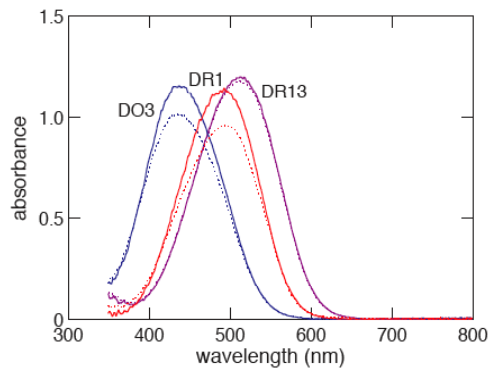


Fig. 2. Absorbance spectrum of PMMA films containing 3.5% by weight of (a) DO3, (b) DR1, and (c) DR13. The dashed lines show the absorbance after micromachining the films.

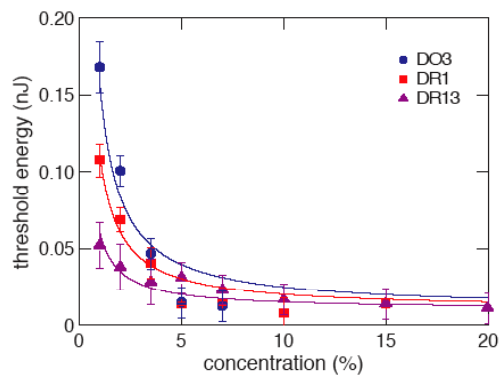


Fig. 3. Threshold energy of PMMA films doped with DO3, DR1 and DR13 as a function of the azochromophore concentration. The solid lines are drawn to guide the eye.

To fabricate waveguides and to study the optical properties of the samples after micromachining, we chose to work exclusively with samples containing 3.5% of azochromophores. Samples with 3.5% doping contain sufficient azochromophores to be useful for applications. We chose not to use samples with higher azochromophore

concentrations because the azochromophores in the highly doped samples tend to aggregate, inhibiting switching of the material, making those samples ineffective for device applications.

To evaluate the optical properties of the micromachined samples, we measured the absorbance of $2\text{ mm} \times 2\text{ mm}$ micromachined areas of each sample. The areas were micromachined at a speed of $20\text{ }\mu\text{m/s}$ with laser pulse energies at the threshold energy of each sample. The dashed lines in Fig. 2 show the absorption spectrum of the microfabricated areas for each sample, while the solid lines show the absorption spectrum of samples that have not been irradiated. The $\pi \rightarrow \pi^*$ electronic transition of the azochromophores decreases after irradiation, indicating photobleaching of the chromophores during the micromachining. The decrease in absorbance is highest for DR1, followed by DO3 and DR13, which has the smallest decrease in the absorption.

Figure 4 shows the decrease in absorbance for each sample at the peak of its absorbance band as function of the writing speed. For this experiment we used energies of 0.29, 0.14 and 0.08 nJ for DO3, DR1 and DR13, respectively, such that the product of the pulse energies and the two photon absorption cross-section is constant. Figure 4, shows that the order of greatest to least drop in absorption is from DR1 to DO3 to DR13, in agreement with the result shown in Fig. 2. The drop in absorption decreases with increasing translation speed, showing that less azochromophore photobleaching occurs at higher micromachining speeds, as expected.

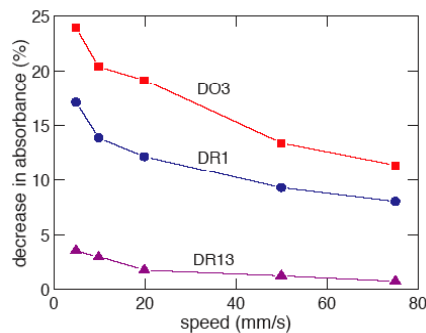


Fig. 4. Decrease in absorbance of PMMA films doped with DO3, DR1 and DR13 as a function of the writing speed of the waveguides.

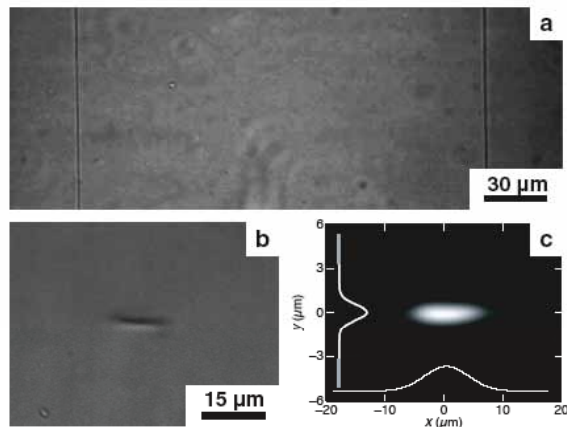


Fig. 5. (a). Optical microscope image of the waveguides micromachined in PMMA doped with DR1 written at a speed of $20\text{ }\mu\text{m/s}$, spaced by $200\text{ }\mu\text{m}$ to prevent crosstalk. (b) Cross-sectional view of the waveguides. (c) Output image of the single-mode profile of 632.8-nm light coupled through the waveguide, along with a graphical representation of the spatial intensity distribution of the profile along the two major axes.

Figure 5(a) shows a transmission optical microscopy image of the femtosecond laser micromachined waveguides in DR1-doped PMMA. These waveguides are visible only in transmission and not in reflection, indicating that the waveguides are inside the bulk. The threshold energies determined for waveguide fabrication inside the bulk are approximately 15% higher than the threshold energies for surface micromachining (Fig. 3) [39]. Figure 5(b) shows a transverse image of a waveguide. As can be seen, the waveguide profile is oblong because the voxel in which modification occurs has elliptical symmetry, due to the two-photon-absorption nature of micromachining in azo-doped PMMA. This is in contrast to the more spherical voxels produced by multi-photon absorption in undoped materials [23]. We

also looked at the output of the waveguide (Fig. 5(c)), confirming that the guided mode is single mode at 632.8 nm. By measuring the numerical aperture (NA) of the waveguide output [23], we estimate the magnitude of the refractive index change to be about 1×10^{-4} .

4. Discussion

In contrast to fs-laser micromachining in undoped transparent materials, where the optical breakdown is a multi-photon process, the results in Fig. 3 show that micromachining in doped polymers is driven by two-photon absorption of the azochromophores. The doping yields a threshold energy that is an order of magnitude smaller than pure PMMA and of glasses [5].

The absorption spectra of the samples (Fig. 2) show that a decrease in absorbance of the PMMA samples doped with the azochromophores occurs after fs-laser micromachining. A similar decrease in the absorption has been reported in the literature when samples containing azochromophores are exposed to light whose wavelengths are within the azochromophores absorption band [40-42]. The observed decrease in absorbance has been attributed to photo-oxidation induced by one-photon absorption (photobleaching) [40-42]. The azochromophore-containing samples we studied, however, are completely transparent and exhibit a large two-photon absorption cross-section at our excitation wavelength of 800 nm, as shown in Fig. 2. This leads us to attribute the photobleaching after fs-laser micromachining to two-photon induced photo-oxidation of the azochromophores. The smaller photobleaching observed for DR13 in Figs. 2 and 4 can be explained by the smaller photo-oxidation potential of DR13 compared to the other two azochromophores. This interpretation is in agreement with photodegradation studies reported for azocompounds under one-photon excitation [40-42].

Photodegradation of azochromophores is a complex subject, and depends on the host polymer, irradiation wavelength, temperature, atmospheric environment and azochromophore structure [40-42]. Systematic studies have demonstrated that photo-induced oxidation is the dominant mechanism for photodegradation of azobenzenes [40-42]. There is a strong correlation between the oxidation potential and the azodye degradation; molecules that have largest oxidation potentials are the most stable, meaning that they photobleach the least [40]. This correlation may explain the observed photobleaching for different azochromophores as observed in Fig. 2. Because DR13 possesses a higher oxidation potential than DO3 and DR1 [40], the observed photobleaching in DR13 is negligible for the range of irradiances we used.

The pulse energy for fs-laser micromachining of doped polymers should be minimized to avoid carbonization and photobleaching. Although the samples show some photobleaching (Fig. 2), the results in Fig. 4 show that significant amounts of unbleached azochromophores remain in the sample. In a previous study, the one-photon-induced photo-oxidation of azochromophores was reduced when the sample was irradiated in an inert atmosphere [40-42]. Similarly, we could micromachine azo-doped PMMA samples in an inert atmosphere to minimize the observed two-photon induced photobleaching, preserving a higher azochromophore concentration after micromachining, and enabling device fabrication.

In Fig. 5, we use a high-repetition laser to micromachine waveguides in the DR1-doped PMMA. Because the interval between successive pulses is shorter than the thermal diffusion time (approximately 1 μ s) in the polymer, the volume around the focal point is heated above the glass transition temperature. After the exposed area is translated out of the focus, the polymer resolidifies producing an index change. The resulting difference in index of refraction yields a waveguide inside the azochromophore-doped PMMA that guides light at 632.8 nm in single mode (Fig. 5(c)). This demonstration opens the doors for new applications of fs-laser micromachined polymeric waveguides containing nonlinear chromophores.

5. Conclusion

In summary, we show that fs-laser waveguide micromachining is possible in azochromophore doped PMMA. The micromachining results from two-photon absorption by the azochromophores at 800 nm. We determined the laser and sample parameters for micromachining PMMA samples doped with the azochromophores DO3, DR1 and DR13. Although we observe photobleaching of the azochromophores during micromachining, our

results show that a significant amount of azochromophores remains unbleached. Finally, we fabricated optical waveguides in bulk PMMA doped with DR1, demonstrating single-mode wave guiding in doped polymers.

Acknowledgments

This work was carried out with the financial support of the National Science Foundation under contract DMI-0334984 and the Army Research Office under contract W911NF-05-1-0471. T. Shih would like to acknowledge support from NSF Graduate Research Fellowship, and C. R. Mendonca acknowledges support from the FAPESP and CAPES (Brazil).

Femtosecond laser-induced formation of nanometer-width grooves on synthetic single-crystal diamond surfaces

Masataka Shinoda,^{a)} Rafael R. Gattass, and Eric Mazur^{b)}*School of Engineering and Applied Sciences, Harvard University, 9 Oxford Street, Cambridge, Massachusetts 02138, USA*

(Received 17 April 2008; accepted 7 January 2009; published online 3 March 2009)

We form periodic linear grooves in synthetic single-crystal diamond with femtosecond pulses at 800 nm. The grooves are 40 nm wide, 500 nm deep, up to 0.3 mm long, and have an average spacing of 146 ± 7 nm. The grooves are perpendicular to the direction of the laser polarization and are formed below the threshold for ablation throughout the focal volume. The submicrometer periodicity is caused by interference between a laser-induced plasma and the incident laser beam, which locally enhances the field at the surface so the ablation threshold is exceeded. Using Raman spectroscopy we find that the structures retain the original diamond composition. © 2009 American Institute of Physics.

[DOI: [10.1063/1.3079512](https://doi.org/10.1063/1.3079512)]

I. INTRODUCTION

Because diamond is an ultrahard material, methods for forming submicrometer structures in diamond are limited.^{1–5} Synthetic single-crystal diamond recently received much attention because of its outstanding optical, electrical, and mechanical properties.^{6–8} The material has found a broad range of applications in deep ultraviolet lasers and photodetectors, field emission displays, high-power semiconductor devices, and surface acoustic wave devices.^{2,4,9–11}

Surface processing of diamond has been demonstrated with ultraviolet and near-infrared femtosecond lasers.^{1,3,5,12–14} The intensity threshold required to ablate diamond with 800-nm pulses is on the order of 2×10^{16} W/m².^{13,14} Within the ablated spot, periodic structuring has been observed with a periodicity below the laser wavelength.³ However, the induced periodic structures are shallow, rough, and confined to the edges of ablation craters or clusters.^{1,3} We report on the generation of nanometer-width periodic grooves in synthetic single-crystal diamond using femtosecond laser pulses. In contrast to previously reported structures, the grooves are formed with laser pulses below the ablation threshold, have a large depth-to-width aspect ratio, and can be extended to millimeter length by translating the laser beam over the sample.

II. EXPERIMENT

The experiments described in this paper were carried out on undoped synthetic single-crystal diamond fabricated by chemical vapor deposition (CVD).⁸ The diamond samples were 1.2 mm thick oriented along the (100) direction. The real and imaginary parts of the refractive index of diamond at 800 nm are 2.397 and 0, respectively. The optical absorption edge is 235 nm.¹¹ The diamond surface was polished to op-

tical grade displaying a final mean surface roughness of 0.7 nm, as measured by atomic force microscopy.

To process the diamond we used a 250-kHz, 120-fs, 800-nm amplified femtosecond Ti:sapphire laser. Using neutral density filters, we adjusted the laser pulse energy to be in the range from 50–250 nJ. The laser was incident normal to the diamond surface and focused by a microscope objective with a numerical aperture of 0.45. The laser spot size on the sample was approximately 2 μ m. The diamond sample was placed on a scanning stage and translated under computer control during irradiation at a scanning speed of 500 μ m/s. The scanning direction was normal to the laser polarization direction. All experiments were carried out in ambient air at atmospheric pressure and room temperature. After irradiation, the diamond sample was rinsed for 30 min with ethanol in an ultrasonic cleaner in order to remove any debris from the ablation process. After cleaning we analyzed the ablated diamond surfaces using a scanning electronic microscope (SEM). No conductive coating was used to avoid blocking the submicrometer structures.

III. RESULTS AND DISCUSSION

Figure 1 shows SEM images of the diamond surfaces after irradiation by femtosecond laser pulses with pulse energies ranging from 72 to 240 nJ; below the energy threshold of 72 nJ we do not observe any surface structures. The dashed arrow in Fig. 1(a) indicates the direction of the laser polarization; the solid arrow shows the direction of sample translation. The grooves always form perpendicularly to the polarization direction. If the laser polarization direction is rotated 90° by inserting a half-wave plate in the optical path, the direction of the grooves also rotates by 90°. Increasing the pulse energy by 10% to 80 nJ leads to ablation throughout the focal volume [Fig. 1(b)]. This observation is consistent with previous reports of the ablation threshold for diamond.¹³ As the pulse energy is increased further, more material is removed, but we continue to observe grooves that are perpendicular to the ablated surface [Figs. 1(c) and 1(d)].

^{a)}Present address: Materials Laboratories, Sony Corporation, 6-7-35 Kitashinagawa, Shinagawa-ku, Tokyo 141-0001, Japan.

^{b)}Electronic mail: mazur@seas.harvard.edu.

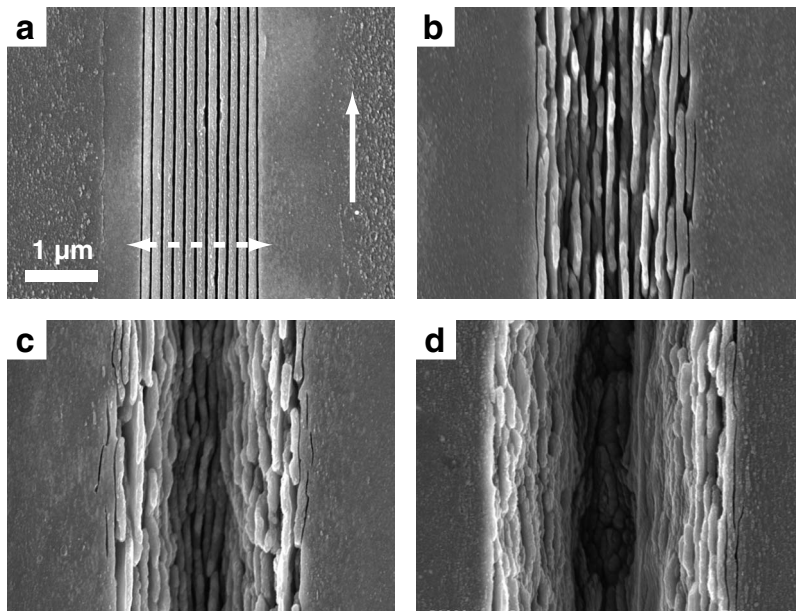


FIG. 1. SEM images of the diamond surface after irradiation with a 1000 pulse train of 120-fs laser pulses at a rate of 250 kHz with a pulse energy of (a) 72, (b) 80, (c) 120, and (d) 240 nJ. The polarization and the scanning directions are indicated by the dotted and solid arrows, respectively.

Figure 2(a) shows an enlarged SEM image of grooves in Fig. 1(a). The average period of the grooves is 146 ± 7 nm, which is about 5.5 times smaller than the free-space wavelength of the laser (2.28 times smaller than the wavelength in diamond). As the laser beam is translated, the periodic grooves continue uninterrupted for hundreds of micrometers [Fig. 2(b)]. The maximum length of the grooves we observed was limited to approximately 300 μm by the translation stage used.

The formation of the grooves is similar to the generation of nanostructures in bulk glass and can be attributed to an interaction between the laser pulse and a laser-induced plasma.^{3,15–17} Because the band gap of the diamond (5.47 eV) is much larger than the photon energy (1.55 eV), the incident laser creates a dense electron plasma through multiphoton excitation at the surface of the diamond.¹⁸ The plasma generated by absorption of the front end of the pulse enhances the electric field of the remainder of the pulse and breaks up into a series of planes perpendicular to the electric field with a periodicity close to $\lambda/2n$, where λ is the free-space wavelength of the incident radiation and n the index of refraction.^{17,19} As the sample is translated the previously formed periodicity favors nonlinear absorption at an identical spatial distribution, causing the periodicity to be maintained as observed in Fig. 2(b).

The results in Fig. 1 show that the “cleanest” and most uniform grooves occur in a narrow energy range just at the measured ablation threshold. Interestingly, the laser-induced

pattern does not reflect the spatial profile of the laser beam, in contrast to the results obtained significantly above threshold. Near the threshold, periodic plasma enhancement of the electric field causes the ablation threshold to be exceeded only at a specific periodicity. Because ablation depends nonlinearly on intensity the resulting grooves are sharp. The periodic grooves are a fingerprint of the plasmonic field enhancement at the surface of diamond and are consistent with previously observed and modeled plasma-induced periodic structures inside the bulk of transparent materials.^{16,17}

Figure 3 shows the cross section of the periodic grooves and a close up of the center pillar after removal of the adjacent pillars using focused ion beam etching. Although debris generated by gallium ions from the focused ion beam partially block the grooves, Figs. 3(a) and 3(b) indicate that the shape and period of the grooves are uniform at the nanometer scale. The 40-nm wide grooves have a depth of about 500 nm, giving them an aspect ratio larger than twelve, significantly larger than previously reported period structures on diamond.^{1,3} The groove depth can be controlled by varying the repetition rate and scanning speed of the femtosecond laser.

To determine the composition of the irradiated material between the grooves, we performed micro-Raman spectroscopy using a 100 \times objective lens and a laser wavelength of 532 nm. Figure 4 shows the Raman spectra obtained from irradiated and unirradiated areas on the diamond surface. Both spectra show a unique peak at 1331 cm^{-1} , correspond-

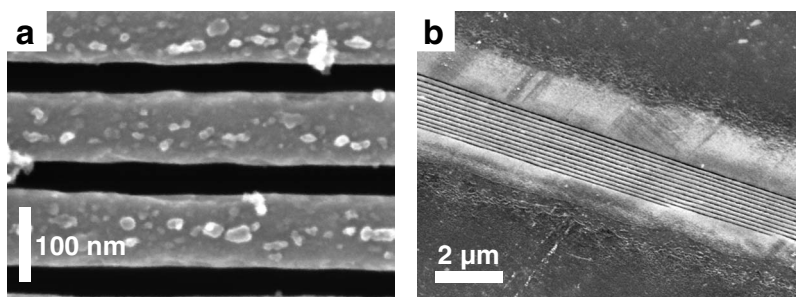


FIG. 2. (a) Enlarged SEM image of the grooves obtained at a pulse energy of 72 nJ. (b) SEM image of grooves of several hundred micrometers length.

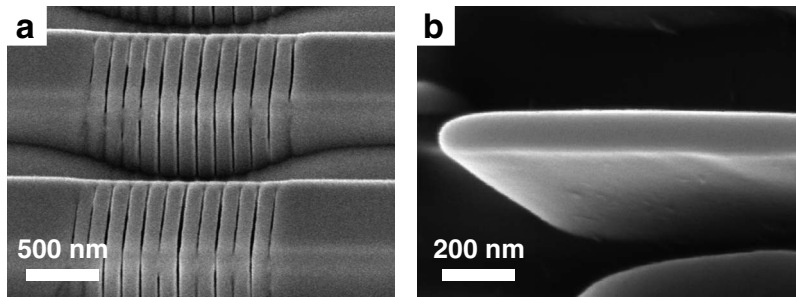


FIG. 3. (a) SEM image of the cross section the periodic surface structure after etching by focused ion beam. (b) SEM image of the center part of a pillar after focused ion beam etching. The SEM images were obtained at an angle of 45° and 30° from the diamond surface, respectively.

ing to the first-order Raman line of a diamond crystal.²⁰ The reduction in Raman intensity on the irradiated area is due to scattering by the grooves. The micro-Raman spectra indicate that the material between the grooves maintains the original diamond composition after irradiation by the femtosecond laser.

Figure 5 shows how even finer features can be obtained by sequential processing. We irradiated the diamond surface sequentially in two different scanning directions to form parallelepiped-shaped pillar structures with submicrometer dimensions. Although the pulse energy is the same as the one used in Fig. 1(a), the resulting structures are not uniform.

Although all the results presented are for single-crystal CVD-grown diamond, we believe that the same effect would be observed on a natural diamond of sufficient purity. Previous studies with natural diamond (type Ia and IIa) show a significant variation in bulk damage threshold from sample to sample.²¹ Defect sites in the form of impurities or point defects are likely to lower the surface ablation threshold, broadening the narrow energy window for periodic structure formation in natural diamond.

IV. CONCLUSION

In summary, we demonstrated the fabrication of long nanometer-width grooves on synthetic single-crystal CVD diamond surfaces by femtosecond laser irradiation. The grooves are formed perpendicular to the laser polarization direction. Their aspect ratio is larger than twelve and their shape is quite uniform at the nanometer scale. We used this technique to fabricate grooves of approximately $300\text{-}\mu\text{m}$ long and parallelepiped-shaped pillar structures with submi-

cometer dimensions. Raman spectroscopy confirms that the structures maintain the original diamond composition. The average groove spacing of 146 nm corresponds to $1/5.5$ of the laser wavelength and can be explained by a plasma enhancement of incident laser electric field at the surface. This process provides a high-speed and low-cost method for fabricating submicrometer devices such as optical gratings or nanoimprint molds in diamond.

ACKNOWLEDGMENTS

Several people contributed to the work described in this paper. M. Shinoda conceived and performed the experiment; R. R. Gattass built and assisted with the experimental setup and analysis; E. Mazur supervised the research and contributed to the development of the manuscript. M. Shinoda wrote the first draft and all authors subsequently took part in the revision process. The authors greatly are grateful to C. R. Mendonca of Universidade de São Paulo for assistance with the femtosecond laser setup and E. Lee of HORIBA Jobin Yvon Inc. for providing the micro-Raman spectroscopy setup. This work was performed in part at the Center for Nanoscale Systems (CNS), a member of the National Nanotechnology Infrastructure Network (NNIN), which is supported by the National Science Foundation under NSF Award no. ECS-0335765. CNS is part of the Faculty of Arts and Sciences at Harvard University. Part of the research

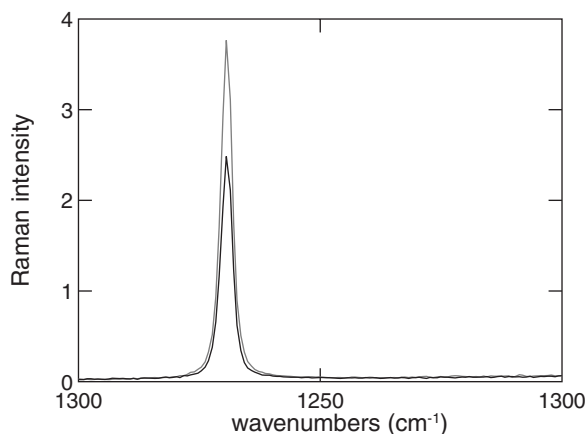


FIG. 4. Micro-Raman spectra of the irradiated (black) and unirradiated (gray) areas a laser-processed diamond sample.

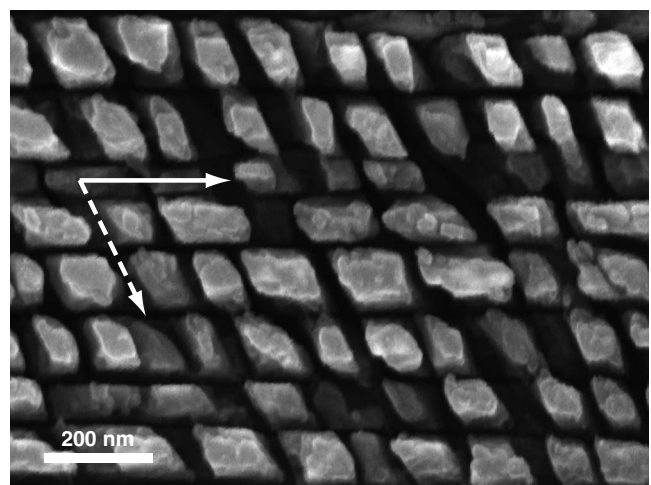


FIG. 5. SEM image of the diamond surface processed sequentially using two scanning directions at 0° (bold arrow) and 300° (dotted arrow).

presented here has been supported by the Army Research Office under Contract No. W911NF-05-1-0471.

- ¹A. M. Ozkan, A. P. Malshe, T. A. Railkar, W. D. Brown, M. D. Shirk, and P. A. Molian, *Appl. Phys. Lett.* **75**, 3716 (1999).
- ²C. Beuret, T. Akiyama, U. Staufer, N. F. de Rooij, P. Niedermann, and W. Hanni, *Appl. Phys. Lett.* **76**, 1621 (2000).
- ³Q. H. Wu, Y. R. Ma, R. C. Fang, Y. Liao, Q. X. Yu, X. L. Chen, and K. Wang, *Appl. Phys. Lett.* **82**, 1703 (2003).
- ⁴Y. Ando, Y. Nishibayashi, and A. Sawabe, *Diamond Relat. Mater.* **13**, 633 (2004).
- ⁵M. Takesada, E. Vanagas, D. Tuzhilin, I. Kudryashov, S. Suruga, H. Murakami, N. Sarukura, K. Matsuda, S. Mononobe, T. Saiki, M. Yoshimoto, and S. Y. Koshihara, *Jpn. J. Appl. Phys., Part 1* **42**, 4613 (2003).
- ⁶R. J. Trew, J. B. Yan, and P. M. Mock, *Proc. IEEE* **79**, 598 (1991).
- ⁷S. Koizumi, K. Watanabe, F. Hasegawa, and H. Kanda, *Science* **292**, 1899 (2001).
- ⁸J. Isberg, J. Hammersberg, E. Johansson, T. Wikstrom, D. J. Twitchen, A. J. Whitehead, S. E. Coe, and G. A. Scarsbrook, *Science* **297**, 1670 (2002).
- ⁹J. Taniguchi, Y. Tokano, I. Miyamoto, M. Komuro, and H. Hiroshima, *Nanotechnology* **13**, 592 (2002).
- ¹⁰M. Pagels, C. E. Hall, N. S. Lawrence, A. Meredith, T. G. J. Jones, H. P. Godfried, C. S. J. Pickles, J. Wilman, C. E. Banks, R. G. Compton, and L. Jiang, *Anal. Chem.* **77**, 3705 (2005).
- ¹¹M. Shinoda, K. Saito, T. Kondo, A. Nakaoki, M. Furuki, M. Takeda, M. Yamamoto, T. J. Schaich, B. M. Van Oerle, H. P. Godfried, P. A. C. Kriele, E. P. Houwman, W. H. M. Nelissen, G. J. Pels, and P. G. M. Spaaij, *Jpn. J. Appl. Phys., Part 1* **45**, 1311 (2006).
- ¹²M. D. Shirk, P. A. Molian, and A. P. Malshe, *J. Laser Appl.* **10**, 64 (1998).
- ¹³G. Dumitru, V. Romano, H. P. Weber, M. Sentis, and W. Marine, *Appl. Phys. A: Mater. Sci. Process.* **74**, 729 (2002).
- ¹⁴D. Ramanathan and P. A. Molian, *ASME J. Manuf. Sci. Eng.* **124**, 389 (2002).
- ¹⁵J. E. Sipe, J. F. Young, J. S. Preston, and H. M. Vandriel, *Phys. Rev. B* **27**, 1141 (1983).
- ¹⁶Y. Shimotsuma, P. G. Kazansky, J. R. Qiu, and K. Hirao, *Phys. Rev. Lett.* **91**, 247405 (2003).
- ¹⁷V. R. Bhardwaj, E. Simova, P. P. Rajeev, C. Hnatovsky, R. S. Taylor, D. M. Rayner, and P. B. Corkum, *Phys. Rev. Lett.* **96**, 253001 (2006).
- ¹⁸B. C. Stuart, M. D. Feit, A. M. Rubenchik, B. W. Shore, and M. D. Perry, *Phys. Rev. Lett.* **74**, 2248 (1995).
- ¹⁹P. P. Rajeev, M. Gertsyov, C. Hnatovsky, E. Simova, R. S. Taylor, P. B. Corkum, D. M. Rayner, and V. R. Bhardwaj, *J. Phys. B* **40**, S273 (2007).
- ²⁰S. A. Solin and A. K. Ramdas, *Phys. Rev. B* **1**, 1687 (1970).
- ²¹J. Hwang, J. B. Ashcom, and E. Mazur, *J. Opt. Soc. Am. B* (submitted).